Advanced Characterization of Shape Memory Polymers and Electrospun Conducting Polymers for Engineering Applications

by

Midhan Siwakoti

A dissertation submitted to the Graduate Faculty of
Auburn University
in partial fulfillment of the
requirements for the Degree of
Doctor of Philosophy

Auburn, Alabama
December 9, 2023

Keywords: shape memory polymers, viscoelasticity, finite element method, recovered enthalpy, structure-property relationship, electrospinning

Approved by

Russell W. Mailen, Chair, Assistant Professor, Aerospace Engineering
Vinamra Agrawal, Assistant Professor, Aerospace Engineering
Asha-Dee Celestine, Visiting Assistant Professor, Aerospace Engineering
Suhasini Gururaja, Associate Professor, Aerospace Engineering
Davide Guzzetti, Assistant Professor, Aerospace Engineering
Chad G. Rose, Assistant Professor, Mechanical Engineering

Abstract

Smart materials are an attractive solution to low cost, low weight and high performance applications. They have multifunctional properties that can be controlled by external stimuli such as light, heat and electricity. Their properties can be tailored for specific purposes, their fabrication process is cost effective, and their applications do not require an additional electronic control system. Smart materials can be broadly classified into their two major abilities, actuation and sensing. They can be programmed to respond to external stimulus (actuation) or sense the changes in their environment (sensing). Throughout this dissertation, the programming/fabrication of such smart materials and their analytical characterization techniques for both actuation and sensing, are discussed.

In chapter 3, the programming process of a polymer for smart actuation application was evaluated using a coupled thermomechanical finite element framework. The polymer was programmed to store applied strain through a pre-straining process which was later recovered by shape recovery through uniform shrinking of the polymer. The strain was applied in two orthogonal directions by passing the polymer through a set of rollers and its shape recovery was investigated by uniformly heating the polymer. The process parameters were parametrically varied to obtain an optimized shape recovery performance. It was found that process parameters such as feed rate and rate of uniform heating changes the shape recovery performance.

In chapter 4, pre-strained polymer was evaluated for its localized shrinking and shape recovery with an application of an applied electric field. The electric field increases the temperature through resistive Joule heating and generates a temperature gradient through the thickness of the polymer. This temperature gradient creates strain gradient through its thickness

resulting in an uneven shrinking of the polymer along its thickness. This results in out-of-plane self-folding of polymers and this is studied for various processing parameters, such as electrical conductivity of the localized region (hinge), width of the hinge and applied voltage. It was found that folding occurs only when the polymer reaches glass transition temperature (T_g) and the speed at which it folds depend on the applied voltage, the width and conductivity of the hinge.

In chapter 5, the structural relaxation of polymers undergoing physical aging is studied for their shape recovery applications. Polymers were aged for several days where they go through structural relaxation by changing their polymer chain conformation. The structural relaxation process was further analyzed by inducing conformational changes to the polymer chains through thermomechanical pre-straining process. The enthalpy lost during the structural relaxation process was quantified for various aging time, pre-straining parameters and their effects on shape recovery performance of the polymer was analyzed.

In chapter 6, polymers under the exposure of space environments, such as UV-C and atomic oxygen were evaluated for their shape recovery performance. The prolonged exposure to these environments causes chain scission in polymer chain backbone, breaks down the polymer chains and introduces foreign functional group to the backbone which degrades the polymer. Polymers were exposed to the UV-C radiation and atomic oxygen for several hours, and the resultant degradation of polymers were analyzed through infrared spectroscopy. The degradation of polymer chains resulted in diminished shape recovery performance in polymers. This chapter lays the experimental foundation for the samples sent to the international space station (ISS) for a 6-months long experiment where they were exposed to space environments of UV-C and atomic oxygen.

In chapter 7, conducting polymer fibers were fabricated through electrospinning process, and characterized for electrical signal sensing applications. Electrospun fiber mat has tremendous

potential to be used as an intelligent interface between a human and a prosthetic limb to enable wider range of mobility in patients with spinal cord injuries (SCI). The non-woven electrospun fibers were analyzed for their morphology and their thermal, mechanical and electrical performance were characterized accordingly. Multiple conducting polymers were evaluated for the electrospinning process and the fiber mat's conductivity was seen to be increasing with increased concentration of conducting polymer solvent.

Keywords: smart materials, shape memory polymers, pre-straining, viscoelasticity, finite element method, recovered enthalpy, structure-property relationship, electrospinning.

Acknowledgment

I would like to dedicate this work to my grandmother Rewati Mainali, who was and still is the beaming source of inspiration to me. I am sure she is smiling her biggest smile up there, showing off all her wrinkles! She was a constant source of love and warmth in my life, always looking out for me and wishing nothing but the best.

I would like to express my deepest gratitude to my advisor Dr. Russell Mailen for his intellectual contribution, unwavering support, and continuous guidance throughout my Ph.D. You helped me find a way along this perilous path, and I wish every student had a mentor like you who makes sure you keep learning and pushing the boundaries. Thank you for your patience and support throughout my time at Auburn.

This work could not have been completed without the support of my advisory committee, Dr. Vinamra Agrawal, Dr. Suhasini Gururaja, Dr. Asha-Dee Celestine, Dr. Davide Guzzetti, and Dr. Chad Rose, who provided their time and resources in making sure my work is up to the accepted standards. Your comments and concerns were always appreciated, and that improved the quality of my work.

A very special thanks goes to my parents, Meena and Dhanya Prasad, who kept on believing and facilitating me in every endeavor. Thank you for listening to me explain my work every once in a while, even though you did not understand anything about it. Even from half a world away, your constant support and motivation helped me complete this work. And now I finally have an answer to your only question, the one where you kept on asking when I will graduate. Well, here it is!

I am thankful to my sister and brother-in-law, Shikha and Sagar, who were there for me in the brightest and the darkest hour of my life. You both always had the best intentions in your heart for me. I am eternally grateful to have a sister like you. And I got both a friend and a brother, who I always wished I had in my life. You guys are the epitome of kind souls. Thank you for motivating me by incessantly asking when I will graduate. Well, here it is!

I would also like to remember the contribution of Mr. Narayan Budathoki, who believed in me when I and everybody else doubted me. You inspired me to keep seeking knowledge and laid the foundation for my intellectual growth. I would not have reached this milestone without your guidance. Thank you for your mentorship at the time when I needed the most.

And finally, my thanks go to all of my friends with whom I had a wonderful opportunity to work with at Auburn, Dr. Alexander Davis, Dr. Gaurav Sharma, Dr. Leily Majidi, Dr. Shankar Kharel, Priscella Goodson, Tarka Giri, Anjan Bhatta, Ishwor Poudel, Prateek Shrestha, Ashutosh Aman Mishra, Ryan, Karan, Joe, Maggie, Robin, Daniel, Marrissa, Greg, Armin, Antara, Ajay, Arun, Harrish, and many more who were not only great to talk to but also actively helped me in various parts of my PhD journey. I would like to stay in touch with you, and if you ever choose to read this part of my dissertation, please reach out to me and let me know what's going on in your life!

In the words of Sir Isaac Newton, "If I have seen further, it is by standing on the shoulders of giants". These are the shoulders of giants that I got the privilege to stand upon and got the opportunity to see further into the distance. I am forever indebted to you and deeply appreciate all of your collective efforts.

Table of Contents

List of figures

List of Abbreviations

ABS	Acrylonitrile butadiene styrene
ASTM	American society for testing and materials
ATR	Attenuated total reflection
CAD	Computer aided design
CSA	Camphorsulfonic acid
DI	Deionized water
DMA	Dynamic mechanical analysis
DMF	Dimethylformamide
DSC	Differential scanning calorimetry
EAP	Electroactive polymer
EDA	Electrodermal activity
ETC	Environment test chamber
FEA	Finite element analysis
FEM	Finite element method
FTIR	Fourier transform infrared spectroscopy
GPC	Gel permeation chromatography
kV	Kilovolts
LEO	Low earth orbit
MDSC	Modulated differential scanning calorimetry
MISSE	Materials International Space Station Experiment
NGDE	Neopentyl glycol diglycidyl ether
OWSME	One way shape memory effect
PANI	Polyaniline
PEDOT	Poly (3,4-ethylenedioxythiophene)
PETG	Polyethylene glycol
PLLA	Polylactic acid
PPy	Polypyrrole

PS	Polystyrene
PSS	Polystyrene sulfonate
PTSA	P-toluene sulfonic acid
PVA	Polyvinyl alcohol
PVDF	Poly(vinylidene fluoride)
PZT	Lead zirconate
RH	Relative humidity
SCI	Spinal cord injuries
SEM	Scanning electron microscope
sEMG	surface electromyography
SMA	Shape memory alloy
SME	Shape memory effect
SMP	Shape memory polymer
SRM	Stimuli responsive material
SRP	Stimuli responsive polymer
TPU	Thermoplastic polyurethane
TTSP	Time temperature superposition principle
TWSME	Two way shape memory effect
UV	Ultraviolet
WLF	Williams Landel Ferry

Chapter 1

Introduction

1.1. Background

Smart materials are a class of multifunctional materials, that can be used as an actuator by modifying their shape[1] or fundamental properties, such as mechanical[2], electrical[3] or optical properties[4], in response to environmental cues such as heat[5], electromagnetic waves[6,7], electric fields[8], or moisture[9], or used as a sensor by converting mechanical response to electrical signal[10]. Smart materials are abundant in nature, such as a chameleon changing its color to blend in with its surroundings, the leaves of *mimosa pudica* collapsing when touched, and leaflets of *codariocalyx motorius* rotating towards sunlight are some of the examples of smart materials found in nature[11]. Throughout several decades, researchers have worked in developing polymers to behave as a stimuli-responsive polymers (SRPs) that are currently being used in variety of industries such as, automotive[12], aerospace[13], biomedical[14], food packaging[15], textiles[16], and acoustics[17]. Due to an increase in demand for high performance, ease of manufacturability and compact size, SRPs are used as a sensor or an actuator without the need for an additional electronic control system[18,19]. SRPs are an attractive alternative to ceramics and metallic materials due to their low cost, faster response time, high strain output, lightweight and biocompatibility properties[20–22]. Some of the commonly used SRPs are thermoplastic polymers such as polystyrene (PS), thermoplastic polyurethane (TPU), and polyethylene terephthalate glycol (PETG) and thermoset polymers such as epoxy resin, thermoset polyurethane and polyimide[23].

SRPs can be tailored to specific functions by programming their response behavior (e.g., mechanical deformation) in response to a stimulus (e.g., thermal exposure). One such application

is the shape memory effect (SME), where the SRPs "memorize" their original shape and can revert back to it in response to the applied stimulus[24]. The programming is conducted on a molecular level of a polymer, by taking the polymer chains through a number of thermomechanical processing steps[25]. This step is called pre-straining, and it imparts a temporary shape to the polymer and conditions the polymer for SME. Polymers can be pre-strained through processes such as hot drawing[26], compression molding[27,28], and rolling[29]. The temporary shape can be reverted to the original shape through a recovery process involving the external stimulus. The shape recovery process of these shape memory polymers (SMPs) has been utilized in various forms, such as Miura-ori folding[30,31] and self-folding origami[25,32,33], to achieve complex 3D structures from a 2D sheets.

SMPs utilize the structure of their polymer chains to exhibit shape memory abilities and is important to understand the effects of pre-straining steps in their recovery behavior. The study of structure-process-property relationship of polymers undergoing pre-straining and eventually the recovery process is therefore essential in understanding the shape memory behavior of SMPs. Furthermore, the underlying process of shape recovery is affected by their prolonged storage condition (physical aging) which needs to be addressed for practical usage of these SMPs.

Furthermore, smart materials has been used in space applications, such as low earth orbits (LEOs), where they are exposed to harsher environmental conditions, such as UV radiation, atomic oxygen, and colder temperatures that change the properties of the material rapidly. Polymers are sensitive to these environments and are known to degrade under prolonged exposure to UV radiation and atomic oxygen. Any polymers used for shape memory applications for future space explorations will get exposed to these conditions, gets degraded rapidly, decreases its performance over time and needs to be studied further.

In addition to smart materials being used as actuators, they have been used as sensors in applications involving detection of toxic gases[34], sensing the presence of organic contaminants in the environment[35] and detecting electrical signals from muscle actuations[36]. Polymers with their inherent properties to sense such changes can be fabricated through numerous processes, such as polymerization[37], additive manufacturing[38], and electrospinning[39]. Electrospinning is a fiber manufacturing process that stretches the polymer solution into nanofibers by applying electrical field and deposits them as a fiber mat[40,41]. For applications involving sensing of electrical signals produced from muscle actuations, electrospun polymer fibers have been widely used in the past years[41,42].

1.2. Research objectives

The current research focuses on studying the structure-process-property relationship of polymers undergoing thermomechanical load and analyze the shape recovery response under various external stimuli. Multiple analytical tools and characterization techniques have been used to quantify the changes in the structure of the polymer. In addition, computational modeling and experimental verification has been conducted to examine the validity of the shape recovery response. This research will provide a better understanding of rolling process applied to SMPs, advance the knowledge of shape recovery performance in SMPs, study the effects of physical aging and UV aging on shape recovery response of SMPs and fabricate an electrically conducting smart fiber mats for sensing application, followed by its characterization.

1.2.1. Computational modeling of hot rolling process for biaxial pre-straining of shape memory polymer sheets

In chapter 3, biaxial pre-straining of a polymer, undergoing rolling, was computationally evaluated for shape memory applications. The goal of the work done in this chapter is to

computationally model a biaxially pre-strained polymer and maximize its shape recovery performance by varying multiple processing parameters. A previously developed finite element framework was used to study the thermomechanical load applied to the polymer through rolling. The amount of strain generated by the roller, in two orthogonal directions, were evaluated. In addition, the role of friction between the roller and workpiece on the amount of stress applied on the workpiece surface is analyzed. Finally, the effects of processing parameters were evaluated to maximize the shape fixity and shape recovery of the pre-strained polymer.

1.2.2. Coupled electro-thermo-mechanical modeling of shape memory polymers

In chapter 4, a previously developed computational framework is modified to include electrical properties of the polymer and thermomechanical load is applied to pre-strain the polymer. The goal of this chapter is to develop a finite element framework that evaluates coupled electro-thermo-mechanical response of a thermomechanically pre-strained polymer actuated by application of electric field. The strain recovery of the pre-strained polymer is triggered by applying localized electrical current to the polymer, and the performance of shape recovery is evaluated through self-folding of the polymer.

1.2.3. Relationship between recovered enthalpy and the shape-memory effect in shape memory polymers

In chapter 5, the structural relaxation of polymers undergoing physical aging is studied for their shape recovery applications. Polymers were physically aged for several days where they go through structural relaxation by changing their polymer chain conformation. The structural relaxation process was further analyzed by inducing conformational changes to the polymer chains through thermomechanical pre-straining process. The enthalpy lost during the structural relaxation

process was quantified for various aging time, pre-straining parameters and their effects on shape recovery performance of the polymer was analyzed.

1.2.4. Effects of UV-aging on shape recovery performance of shape memory polymers

In chapter 6, polymers were studied for their shape recovery performance when exposed to UV-C radiation and atomic oxygen. The prolonged exposure to these environments introduces foreign functional groups to the polymer chain backbone, causes polymer chain scission, and breaks down the polymer chains. Polymers were exposed to the UV-C radiation and atomic oxygen for several hours, and the resultant degradation of polymers were analyzed through infrared spectroscopy. The thermal, mechanical and viscoelastic characterization were performed, and the change in shape recovery performance of UV-aged polymers were analyzed.

1.2.5. Characterization of electrospun, conducting polymer electrodes enabling mobility for all

Finally, in chapter 7, the sensing application of smart materials is studied. In this chapter, conducting polymer fibers were fabricated through electrospinning process, and characterized for electrical signal sensing applications. The non-woven electrospun fibers were analyzed for their morphology and their thermal, mechanical and electrical performance were characterized accordingly. Electrospun fiber mat has tremendous potential to be used as an intelligent interface between a human and a prosthetic limb to enable wider range of mobility in patients with spinal cord injuries (SCI). Multiple conducting polymers were evaluated for the electrospinning process and the fiber mat's conductivity was analyzed for several concentrations of conducting polymer solvent.

1.3. References

(1) Xu, W.; Kwok, K. S.; Gracias, D. H. Ultrathin Shape Change Smart Materials. *Acc. Chem. Res.* **2018**, *51* (2), 436–444. https://doi.org/10.1021/acs.accounts.7b00468.

(2) Tan, L.; Davis, A. C.; Cappelleri, D. J. Smart Polymers for Microscale Machines. *Advanced Functional Materials* **2021**, *31* (9), 2007125. https://doi.org/10.1002/adfm.202007125.

(3) Abbas, M. Smart Materials for Changing the Electrical Properties of Nanostructures. *Composites and Advanced Materials* **2021**, *30*, 26349833211016479. https://doi.org/10.1177/26349833211016479.

(4) Choi, S. H.; Duzik, A. J.; Kim, H.-J.; Park, Y.; Kim, J.; Ko, H.-U.; Kim, H.-C.; Yun, S.; Kyung, K.-U. Perspective and Potential of Smart Optical Materials. *Smart Mater Struct* **2017**, *26* (9), 093001. https://doi.org/10.1088/1361-665X/aa7c32.

(5) Sun, L.; Huang, W. M.; Ding, Z.; Zhao, Y.; Wang, C. C.; Purnawali, H.; Tang, C. Stimulus-Responsive Shape Memory Materials: A Review. *Materials & Design* **2012**, *33* (1), 577–640. https://doi.org/10.1016/J.MATDES.2011.04.065.

(6) Liu, Y.; Boyles, J. K.; Genzer, J.; Dickey, M. D. Self-Folding of Polymer Sheets Using Local Light Absorption. *Soft Matter* **2012**, *8* (6), 1764–1769. https://doi.org/10.1039/C1SM06564E.

(7) Liu, Y.; Miskiewicz, M.; Escuti, M. J.; Genzer, J.; Dickey, M. D. Three-Dimensional Folding of Pre-Strained Polymer Sheets via Absorption of Laser Light. *Journal of Applied Physics* **2014**, *115* (20). https://doi.org/10.1063/1.4880160.

(8) Yang, P.; Ghosh, S.; Xia, T.; Wang, J.; Bissett, M. A.; Kinloch, I. A.; Barg, S. Joule Heating and Mechanical Properties of Epoxy/Graphene Based Aerogel Composite. *Composites Science and Technology* **2022**, *218*, 109199. https://doi.org/10.1016/J.COMPSCITECH.2021.109199.

(9) Yang, M.; Wang, S.-Q.; Liu, Z.; Chen, Y.; Zaworotko, M. J.; Cheng, P.; Ma, J.-G.; Zhang, Z. Fabrication of Moisture-Responsive Crystalline Smart Materials for Water Harvesting and Electricity Transduction. *J. Am. Chem. Soc.* **2021**, *143* (20), 7732–7739. https://doi.org/10.1021/jacs.1c01831.

(10) Das, R.; Zeng, W.; Asci, C.; Del-Rio-Ruiz, R.; Sonkusale, S. Recent Progress in Electrospun Nanomaterials for Wearables. *APL Bioengineering* **2022**, *6* (2), 21505. https://doi.org/10.1063/5.0088136.

(11) Hu, J.; Meng, H.; Li, G.; Ibekwe, S. I. A Review of Stimuli-Responsive Polymers for Smart Textile Applications. *Smart Materials and Structures* **2012**, *21* (5). https://doi.org/10.1088/0964-1726/21/5/053001.

(12) Bahl, S.; Nagar, H.; Singh, I.; Sehgal, S. Smart Materials Types, Properties and Applications: A Review. *Materials Today: Proceedings* **2020**, *28*, 1302–1306. https://doi.org/10.1016/j.matpr.2020.04.505.

(13) Sharma, K.; Srinivas, G. Flying Smart: Smart Materials Used in Aviation Industry. *Materials Today: Proceedings* **2020**, *27*, 244–250. https://doi.org/10.1016/j.matpr.2019.10.115.

(14) Fang, F.; Meng, F.; Luo, L. Recent Advances on Polydiacetylene-Based Smart Materials for Biomedical Applications. *Mater. Chem. Front.* **2020**, *4* (4), 1089–1104. https://doi.org/10.1039/C9QM00788A.

(15) Halonen, N.; Pálvölgyi, P. S.; Bassani, A.; Fiorentini, C.; Nair, R.; Spigno, G.; Kordas, K. Bio-Based Smart Materials for Food Packaging and Sensors – A Review. *Frontiers in Materials* **2020**, *7*.

(16) Chen, G.; Li, Y.; Bick, M.; Chen, J. Smart Textiles for Electricity Generation. *Chem. Rev.* **2020**, *120* (8), 3668–3720. https://doi.org/10.1021/acs.chemrev.9b00821.

(17) Athanassiadis, A. G.; Ma, Z.; Moreno-Gomez, N.; Melde, K.; Choi, E.; Goyal, R.; Fischer, P. Ultrasound-Responsive Systems as Components for Smart Materials. *Chem. Rev.* **2022**, *122* (5), 5165–5208. https://doi.org/10.1021/acs.chemrev.1c00622.

(18) Hu, L.; Shu, T.; Wan, Y.; Fang, C.; Gao, F.; Serpe, M. J. Recent Advances in Stimuli-Responsive Polymers for Sensing and Actuation. *Mol. Syst. Des. Eng.* **2021**, *6* (2), 108–121. https://doi.org/10.1039/D0ME00133C.

(19) Hu, L.; Zhang, Q.; Li, X.; Serpe, M. J. Stimuli-Responsive Polymers for Sensing and Actuation. *Mater. Horiz.* **2019**, *6* (9), 1774–1793. https://doi.org/10.1039/C9MH00490D.

(20) Mitchell, A.; Lafont, U.; Hołyńska, M.; Semprimoschnig, C. Additive Manufacturing — A Review of 4D Printing and Future Applications. *Additive Manufacturing* **2018**, *24*, 606–626. https://doi.org/10.1016/j.addma.2018.10.038.

(21) Huang, W. M.; Yang, B.; Zhao, Y.; Ding, Z. Thermo-Moisture Responsive Polyurethane Shape-Memory Polymer and Composites: A Review. *J. Mater. Chem.* **2010**, *20* (17), 3367–3381. https://doi.org/10.1039/B922943D.

(22) Yang, B.; Huang, W. M.; Li, C.; Li, L. Effects of Moisture on the Thermomechanical Properties of a Polyurethane Shape Memory Polymer. *Polymer* **2006**, *47* (4), 1348–1356. https://doi.org/10.1016/j.polymer.2005.12.051.

(23) Nithin, K. S.; Sachhidananda, S.; Shilpa, K. N.; Sandeep, S.; Karthik, C. S.; Jagajeevan Raj, B. M.; Siddaramaiah, H. 1 - Polymer-Based Smart Composites and/or Nanocomposites for Optical, Optoelectronic, and Energy Applications: A Brief introduction†Deceased. In *Polymer-Based Advanced Functional Composites for Optoelectronic and Energy Applications*; Subramani, N. K., Siddaramaiah, H., Lee, J. H., Eds.; Elsevier, 2021; pp 1–29. https://doi.org/10.1016/B978-0-12-818484-4.00011-2.

(24) Dayyoub, T.; Maksimkin, A. V.; Filippova, O. V.; Tcherdyntsev, V. V.; Telyshev, D. V. Shape Memory Polymers as Smart Materials: A Review. *Polymers (Basel)* **2022**, *14* (17), 3511. https://doi.org/10.3390/polym14173511.

(25) Mailen, R. W.; Liu, Y.; Dickey, M. D.; Zikry, M.; Genzer, J. Modelling of Shape Memory Polymer Sheets That Self-Fold in Response to Localized Heating. *Soft Matter* **2015**, *11* (39), 7827–7834. https://doi.org/10.1039/C5SM01681A.

(26) Kim, J. W.; Lee, J. S. Effect of Heat Drawing Process on Mechanical Properties of Dry-Jet Wet Spun Fiber of Linear Low Density Polyethylene/Carbon Nanotube Composites. *International Journal of Polymer Science* **2017**, *2017*, e6197348. https://doi.org/10.1155/2017/6197348.

(27) Xie, J.; Wang, S.; Cui, Z.; Wu, J. Process Optimization for Compression Molding of Carbon Fiber–Reinforced Thermosetting Polymer. *Materials (Basel)* **2019**, *12* (15), 2430. https://doi.org/10.3390/ma12152430.

(28) Rangaswamy, H.; M, H. H.; Gowdru Chandrashekarappa, M. P.; Pimenov, D. Y.; Giasin, K.; Wojciechowski, S. Experimental Investigation and Optimization of Compression Moulding Parameters for MWCNT/Glass/Kevlar/Epoxy Composites on Mechanical and Tribological Properties. *Journal of Materials Research and Technology* **2021**, *15*, 327–341. https://doi.org/10.1016/j.jmrt.2021.08.037.

(29) Mitsoulis, E. 11 - Calendering of Polymers. In *Advances in Polymer Processing*; Thomas, S., Weimin, Y., Eds.; Woodhead Publishing, 2009; pp 312–351. https://doi.org/10.1533/9781845696429.3.312.

(30) Lv, C.; Krishnaraju, D.; Konjevod, G.; Yu, H.; Jiang, H. Origami Based Mechanical Metamaterials. *Scientific Reports* **2014**, *4* (1), 1–6. https://doi.org/10.1038/srep05979.

(31) Pinson, M. B.; Stern, M.; Carruthers Ferrero, A.; Witten, T. A.; Chen, E.; Murugan, A. Self-Folding Origami at Any Energy Scale. *Nature Communications 2017 8:1* **2017**, *8* (1), 1–8. https://doi.org/10.1038/ncomms15477.

(32) Lee, Y.; Cho, M. Self-Folding Structure Using Light-Absorption of Polystyrene Sheet. **2017**, *10165*, 128–133. https://doi.org/10.1117/12.2259911.

(33) Hayes, G. J.; Liu, Y.; Genzer, J.; Lazzi, G.; Dickey, M. D. Self-Folding Origami Microstrip Antennas. *IEEE Transactions on Antennas and Propagation* **2014**, *62* (10), 5416–5419. https://doi.org/10.1109/TAP.2014.2346188.

(34) Adhikari, B.; Majumdar, S. Polymers in Sensor Applications. *Progress in Polymer Science* **2004**, *29* (7), 699–766. https://doi.org/10.1016/j.progpolymsci.2004.03.002.

(35) Pavlyukovich, N. G.; Murashov, D. A.; Dorozhkina, G. N.; Rozanov, I. A. Physicochemical Characteristics of the Reaction of Vapors of Organic Liquids with Divinyl-Styrene and Isoprene Polymer Films of Piezoelectric Chemical Sorption Sensors. *J Anal Chem* **2000**, *55* (5), 469–473. https://doi.org/10.1007/BF02757487.

(36) Kang, K.; Rhee, K.; Shin, H.-C. Event Detection of Muscle Activation Using an Electromyogram. *Applied Sciences* **2020**, *10* (16), 5593. https://doi.org/10.3390/app10165593.

(37) da Costa, T. H.; Choi, J.-W. Fabrication and Patterning Methods of Flexible Sensors Using Carbon Nanomaterials on Polymers. *Advanced Intelligent Systems* **2020**, *2* (5), 1900179. https://doi.org/10.1002/aisy.201900179.

(38) Criado-Gonzalez, M.; Dominguez-Alfaro, A.; Lopez-Larrea, N.; Alegret, N.; Mecerreyes, D. Additive Manufacturing of Conducting Polymers: Recent Advances, Challenges, and Opportunities. *ACS Appl. Polym. Mater.* **2021**, *3* (6), 2865–2883. https://doi.org/10.1021/acsapm.1c00252.

(39) Laudenslager, M. J.; Sigmund, W. M. Electrospinning. *Encyclopedia of Nanotechnology; Bhushan, B., Ed.; Springer: Dordrecht, The Netherlands* **2012**, 769–775.

(40) Wang, L.; Ryan, A. J. Introduction to Electrospinning. In *Electrospinning for Tissue Regeneration*; Bosworth, L. A., Downes, S., Eds.; Woodhead Publishing Series in Biomaterials; Woodhead Publishing, 2011; pp 3–33. https://doi.org/10.1533/9780857092915.1.3.

(41) Wu, S.; Dong, T.; Li, Y.; Sun, M.; Qi, Y.; Liu, J.; Kuss, M. A.; Chen, S.; Duan, B. State-of-the-Art Review of Advanced Electrospun Nanofiber Yarn-Based Textiles for Biomedical Applications. *Appl Mater Today* **2022**, *27*, 101473. https://doi.org/10.1016/j.apmt.2022.101473.

(42) Bednarczyk, K.; Matysiak, W.; Tański, T.; Janeczek, H.; Schab-Balcerzak, E.; Libera, M. Effect of Polyaniline Content and Protonating Dopants on Electroconductive Composites. *Scientific Reports 2021 11:1* **2021**, *11* (1), 1–11. https://doi.org/10.1038/s41598-021-86950-4.

Chapter 2

Literature Review

The dissertation focuses on shape memory polymers (SMPs), smart materials and shape recovery process of the polymers. The understanding of polymers, their structural arrangement and their characterization techniques is provided in this chapter.

2.1. Polymers

Polymers are a class of materials that consists of a collection of repeating molecular units (monomer) linked together by primary covalent bonds[1]. Polymers are distinct from other materials such as metals as their properties, such as mechanical, optical or electrical conductivity vary with time, temperature, and other environmental factors due to their molecular structure[2]. Polymers can naturally occur such as silk, cellulose, and starch or can be synthetically prepared such as polystyrene, Teflon™, and nylon[3]. Polymers are generally superior to other materials like metals in terms of their low cost, light weight, corrosion resistance and easy processability, while they lag behind metals in terms of strength, electrical conductivity and recyclability[1]. Polymers, through means of additives, can be tailored to enhance certain properties such as colors, conductivity, and strength[4]. This has led to polymers being an integral part of day-to-day life and they find usage in applications such as food packaging, fibers and textiles, manufacturing, electronics, transportation and biomedical devices[5].

2.1.1. Monomer unit

The individual monomer unit consists of carbon backbone with other elements such as hydrogen, oxygen, and nitrogen, linked with each other to form a polymer chain. Each polymer chain can have different lengths depending on the number of linked monomer units and is

considered to be a single molecule, hence the name macromolecule (macro = large), as shown in Figure 2.1a. These polymer chains can have different regions, such as crystalline region, where the chains are folded in an orderly way or amorphous region, where the chains are oriented randomly, as shown in Figure 2.1b. The polymer chains are entangled with each other and can occur either through secondary van der Waals bond or primary covalent bond[1]. These bonds are a function of temperature. which affects both the molecular and bulk properties of polymers[6]. Polymers are categorized into two types, thermoplastic and thermoset polymer.

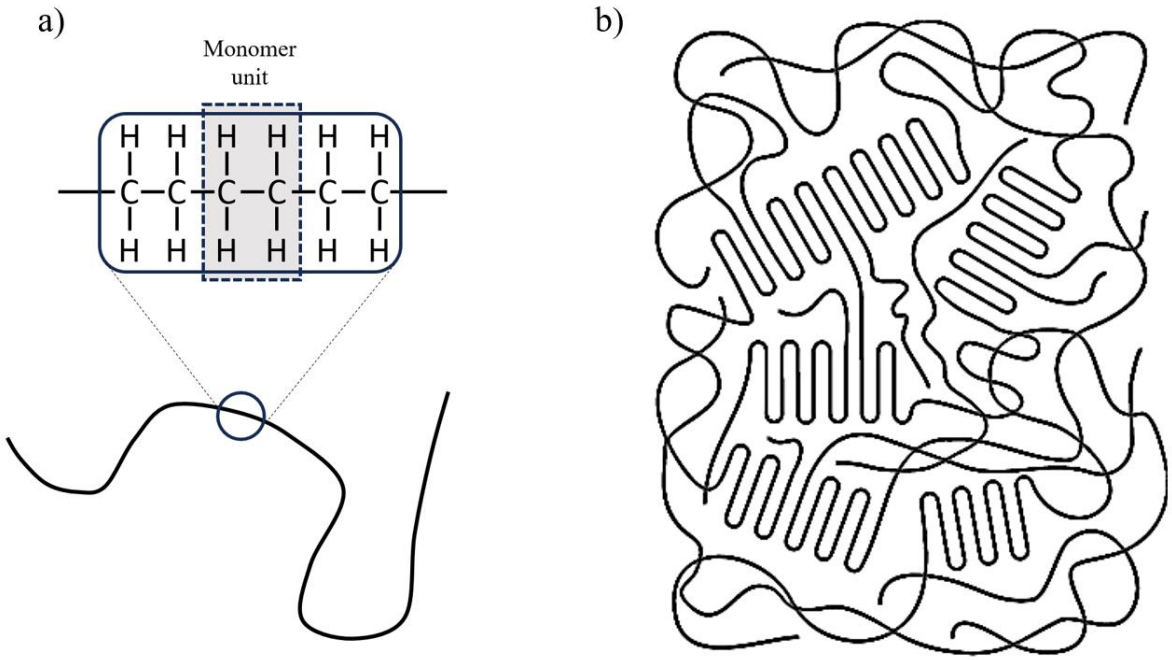

Figure 2.1: Schematic representation of macromolecular structure of polyethylene. a) Representative polymer chain containing multiple monomer units. b) Collection of polymer chains in crystalline (folded up portion of a polymer chain) or amorphous (random portion of a polymer chain)[1].

2.1.1.1. Thermoplastic polymers

The polymers where intermolecular entanglement of polymer chains occur through weak van der Waals bond is thermoplastic polymers as shown in Figure 2.2a. Thermoplastics have lower strength compared to thermoset polymers but are relatively easy to process due to the weak entanglements. They are recyclable and can be easily molded by heating and deforming repeatedly. reversibly[7]. Thermoplastic polymers are usually manufactured through extrusion, injection molding, or compression molding[8]. Some examples of commodity thermoplastic polymers are polyethylene, polypropylene, and polystyrene.

2.1.1.2. Thermoset polymers

The polymers where intermolecular crosslink occurs through primary covalent bond is thermoset polymers, as shown in Figure 2.2b. The crosslink networks are usually stronger than the entanglements found in thermoplastic polymer. Unlike thermoplastic polymers, thermosets degrade when heated and cannot be molded reversibly[1]. Thermoset polymers are used as a high performance composites in automotive and aerospace industries[7]. They are manufactured through reaction injection molding, casting, or transfer molding[8]. Some examples of thermoset polymers are epoxy resins, Bakelite™, and thermosetting polyurethane.

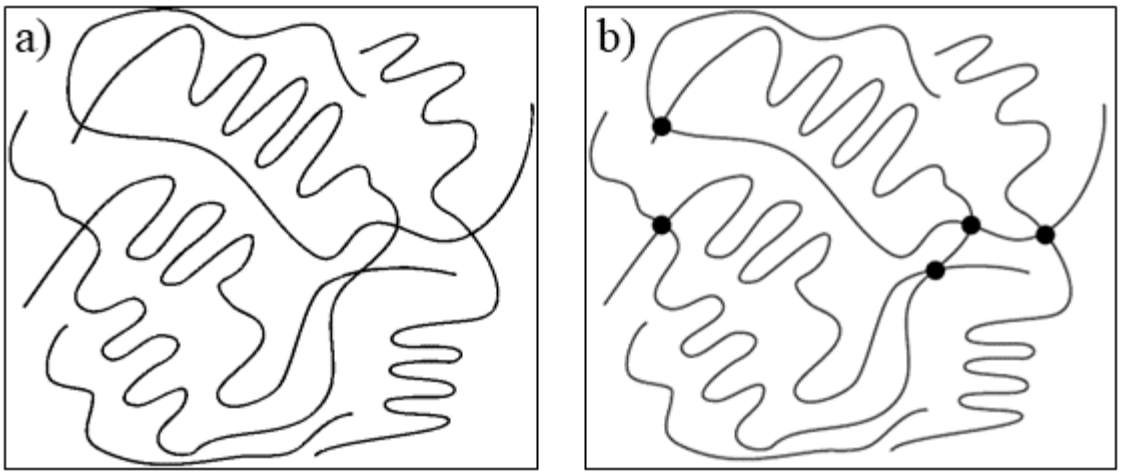

Figure 2.2: Representative polymer chains containing entanglements in a) thermoplastic polymer and b) thermoset polymer. The dots represents presence of crosslink between polymer chains in thermoset polymer[1].

2.1.2. Polymer chain motion

The polymer chain network in both thermoplastic and thermoset polymers have free volumes between them providing enough space for chains to undergo random motion at various temperatures[9]. This motion of polymer chains is best described in terms of reptation (derived from the word *reptile*) or worm-like creeping motion of one polymer chain through a matrix of neighboring chains[10], as shown in Figure 2.3.

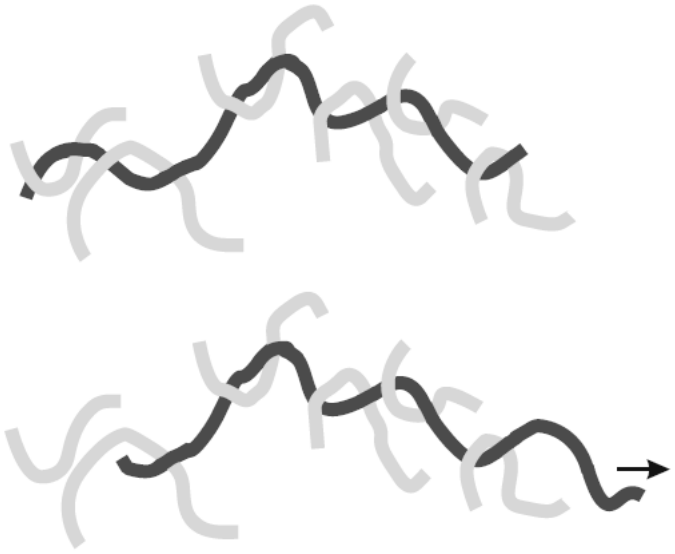

Figure 2.3: Polymer chain motion depicted through reptation, where one polymer chain slide through its neighboring chains.[11]

For thermoplastic polymers, the free volume between the polymer chain decreases at lower temperatures. At this temperature, the polymer behaves as a solid elastic material. In contrast, at higher temperatures, the polymer chains are free to move around and behaves as a viscous liquid (thermoplastics) or elastomer (thermosets).

Similarly, at low temperatures, despite having low free volume, individual polymer chains can creep through the neighboring chains extremely slowly. The time scale of such creeping motion is long enough to be undetected at normal time. With enough time, polymer eventually behaves as a flowing viscous liquid at sufficiently lower temperatures[1].

For thermoset polymers, the behavior is similar to that of thermoplastic polymers at lower temperatures, however, due to the presence of stronger crosslink between the polymer chains, they cannot freely move around and do not behave as a viscous liquid at both higher temperatures and longer time[1].

The dual nature, elastic and viscous, residing in the same material, make polymers unique and interesting. The elastic and viscous properties, both are reversible in polymers and are time and temperature dependent[1]. This present a challenge in understanding the mechanical behavior of a polymer and therefore is explored through a time temperature dependent model called viscoelasticity.

2.1.3. Viscoelasticity

Polymers, due to the motion of polymer chains, have a range of elasticity values depending on temperature and time. This range of elasticity is a measure of free volume between the polymer chains and their movement at a given temperature[12]. It ranges from glassy elastic modulus where the chain movement is minimal and restricted, to rubbery viscous modulus where the chains can slide past each other freely (for thermoplastic polymers). The modulus can be reversibly changed at the glass transition temperature (T_g), as shown in Figure 2.4[13]. At lower temperatures ($T < T_g$), polymer mobility is low, chain movement is frozen and both polymers behave as an elastic material. At higher temperatures ($T > T_g$), polymer chains can move around freely for thermoplastic polymers, and they behave as viscous material. Thermoset polymers exhibit loss in its modulus but they do not flow due to the presence of stronger crosslinks preventing its chain motions[1].

During the glass transition, the amorphous portion of polymer chains have an increased mobility and the van der Waals force decreases. This softens the material and manifests in the significant drop of its modulus within a smaller temperature range. Apart from modulus drop, multiple transitions occur at T_g, such as thermal expansion coefficient, specific volume and specific heat capacity undergoes a discontinuity[1]. These transitions occur at T_g due to an onset of large chain motion with a dramatic increase in free volume.

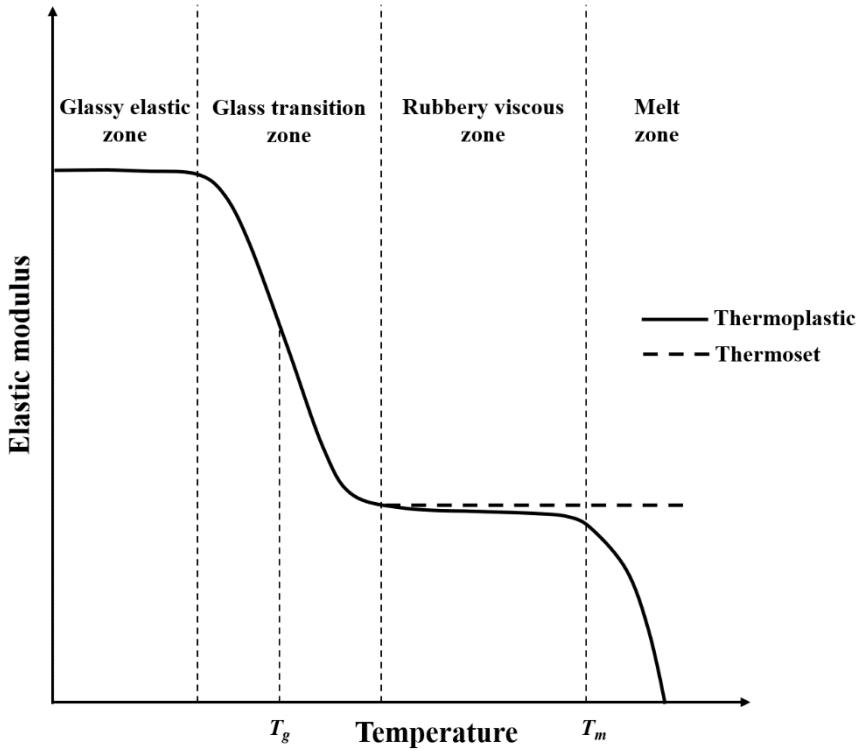

Figure 2.4: Temperature dependence of elastic modulus of thermoplastic polymer (solid line) and thermoset polymer (dashed line). At lower temperatures ($T < T_g$), polymers behave as an elastic material, at higher temperatures ($T_g < T < T_m$), thermoplastic polymers behave as viscous material and thermosets show no change in its modulus due to crosslinks among the polymer chains. The transition between elastic and viscous regime occurs at T_g and at temperature above the melting temperature T_m, the polymer completely melts.

The transition of mechanical properties at T_g is reversible and can be utilized to program a polymer for a specific purpose. The viscoelastic property of a polymer is an exciting concept in the realm of materials that can adapt their properties in response to external stimuli. By employing viscoelastic transition of polymers, researchers can create novel systems that not only respond to stimuli but also exhibit controlled and specific time-dependent responses.

2.2. Smart materials

Smart materials are a class of active materials that can adapt their properties, such as shape[14] and physical properties[15] in response to the controlled application of external stimuli, such as heat[16,17], electromagnetic waves[18,19], electric fields[20,21] and magnetic fields[22]. These stimuli-responsive materials (SRMs) are tailored to transduce external stimuli into physical changes, such as thermochromic (color change in response to the applied heat)[23] piezoelectric (generating electrical charge in response to the applied mechanical load)[24,25], and shape memory (transitioning between temporary and permanent state in response to the applied thermal load)[15,26]. SRMs that can reversibly change their shape are programmed to include SME and can be triggered in smart materials such as SMPs through viscoelastic transition[27], and in SMAs through crystalline transitions[28,29]. Due to their low cost, high strain output, lightweight and biocompatibility properties, SRMs are advantageous over materials like metals, ceramics and glass[30–32]. Shape memory effect of SRMs has been utilized over the past decades to create sensors and actuators without the need of additional electronic control system[33,34]. Some industrial applications include biomedical devices[35,36], artificial muscles[37], self-healing applications[38,39], self-deployable space structures[40], auxetic structures[41,42], structural health monitoring[43,44], smart packaging[45], smart textiles[46], and vibration dampening applications[47,48].

2.2.1. Types of smart materials

A number of SRMs initiate shape change through the application of external stimuli. Various SRMs and their shape change response mechanism are briefly described here.

2.2.1.1. Piezoelectric materials

Piezoelectric materials can generate electrical charge in response to the applied mechanical load (direct piezoelectric effect) and conversely, convert electrical input to mechanical deformation

(inverse piezoelectric effect)[24,25], as shown in Figure 2.5. Piezoelectric materials can be naturally occurring, such as tourmaline and quartz[49], or artificially synthesized, such as PZT[50] and potassium-sodium niobate[51]. The mechanism of piezoelectricity in a crystal lattice is described by the movement of ions in the crystal developing electrical charge when an external mechanical load is applied[52]. Piezoelectric materials have been extensively used in applications such as biosensors[53], healthcare monitoring[54] and energy harvesting[55].

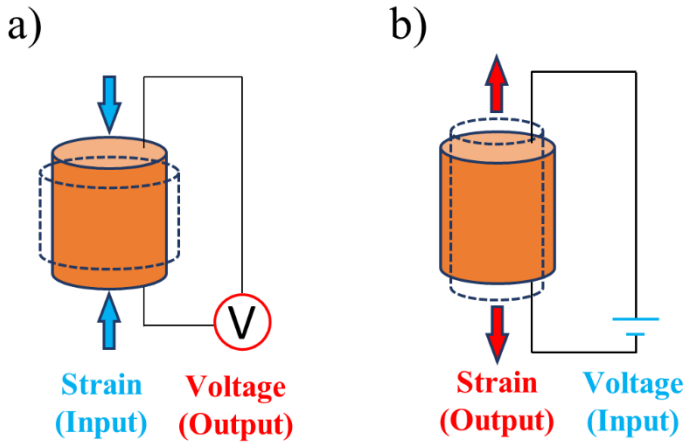

Figure 2.5: Schematics of a) direct piezoelectric effect and b) inverse piezoelectric effect. Blue and red represents input and output respectively for each effect.

2.2.1.2. Electroactive polymers (EAPs)

Polymers exhibiting shape change in response to an applied electrical field is grouped as EAPs[56]. Unlike piezoelectric materials, EAPs under the application of electric field exhibit shape change by the accumulation of opposing electric charges on the surfaces of the polymer[57]. EAPs can undergo larger mechanical deformation compared to a piezoelectric material and can sustain the load longer[56]. Due to the larger mechanical deformation and excellent biocompatibility

properties, EAPs has been used in applications such as artificial muscles[58], tissue engineering[59] and soft robotics[60].

2.2.1.3. Shape memory alloys (SMAs)

SMAs are metallic alloys that have shape memory properties and can return to their original shape in the presence of external heat. They are one of the widely used smart materials in applications ranging from automotive[61] to biomedical devices[62]. SMAs exhibit shape memory effect through a reversible solid-solid phase transformation between two distinct crystal structures, martensite and austenite[63]. The martensite is a lower energy crystal phase which is stable at lower temperatures, while austenite is stable at higher temperatures[64].

The shape memory sequence for SMAs is shown in Figure 2.6. The twinned martensite crystal phase of SMAs can be plastically deformed at lower temperature with an application of a mechanical load to de-twinned martensite phase. The unloading at this temperature recovers some strain elastically and it retains the temporary shape. When the unloaded detwinned martensite is heated above the austenite start temperature (A_s), the transformation to austenite phase begins and the material begins contracting and start to recover its original shape. The transformation ends at the austenite finish temperature (A_f) after which the material is cooled to the original temperature. During the cooling process, the austenite phase reverts to the twinned martensite phase at the martensite start temperature (M_s) and it ends at martensite finish temperature (M_f). The transformation back to the martensite phase during cooling recovers the original twinned crystal phase, thus imparting SME on the SMA.

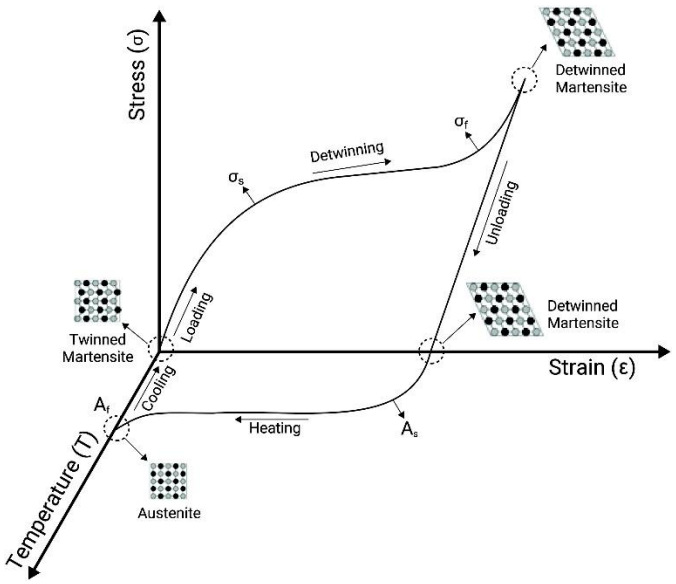

Figure 2.6: Reversible solid-solid phase transformation between martensite and austenite phase inducing shape memory effect to the shape memory alloys[65].

This feature of SMA is called one way shape memory effect (OWSME), where the SMA maintains the temporary shape and can revert to its original shape by reheating. Another feature of SMA is called two-way shape memory effect (TWSME), where the SMA can "remember" two shapes, one at lower temperature and the other at higher temperature and can show the shape memory effect during both heating and cooling. TWSME usually recovers half of the strain compared to OWSME and is therefore preferred less than compared to OWSME. The third feature of SMA is called superelasticity, where the SMA appear extremely elastic. This occurs at temperatures just above A_f, where the applied load transforms the austenite phase to the martensite phase resulting in relatively high deformation (extremely elastic). When unloaded at this temperature, the deformed shape reverts to the austenite phase and the SMA recovers its original shape[63].

SMA such as Nickel-Titanium (NiTinol) is used in medical applications such as vascular surgery[66], orthodontic wires[67] and catheter tips[68] due to its excellent shape memory and biocompatibility properties.

2.2.1.4. Shape memory polymers (SMPs)

SMPs are polymers that has been programmed to "memorize" its original shape and can change its shape between its original and the temporary shape. The shape memory effect in SMPs originates from changes to the conformation of individual polymer chains. The entangled polymer chains consist of netpoints between the polymer chains[27] as shown in Figure 2.7. The netpoints can be physical entanglement between the chains, crystalline phase, block copolymers or chemical crosslinks[27]. The netpoints acts as an anchor point to "memorize" the original undeformed shape, while the polymer chains can slide past each other to deform and retain a temporary shape. In semi-crystalline polymers, as shown in Figure 2.7, the shape change of SMPs is based on the entanglement of alternating segments of crystalline phase netpoints and random polymer chains, while in an amorphous polymer, the net points are the physical entanglement between random polymer chains.

The polymer chains, when deformed at higher temperatures slide past each other and retain the deformed shape when cooled down. They can return back to their original configuration after reheating, through recovery of the initial strain. SMPs can undergo shape change in response to the thermal energy in the form of heat[16], light[69] or electricity[20]. SMPs, unlike SMAs, can sustain larger mechanical deformation (up to two orders of magnitude more), provide higher recoverable strain (up to two orders of magnitudes more), and require lower actuation energy (up to two orders of magnitude less)[32,70]. Thus, SMPs are preferred over SMAs in applications such as heat shrinking tubes[71], adaptive sensors[72], self-deploying structures[73,74] and origami structures[75,76].

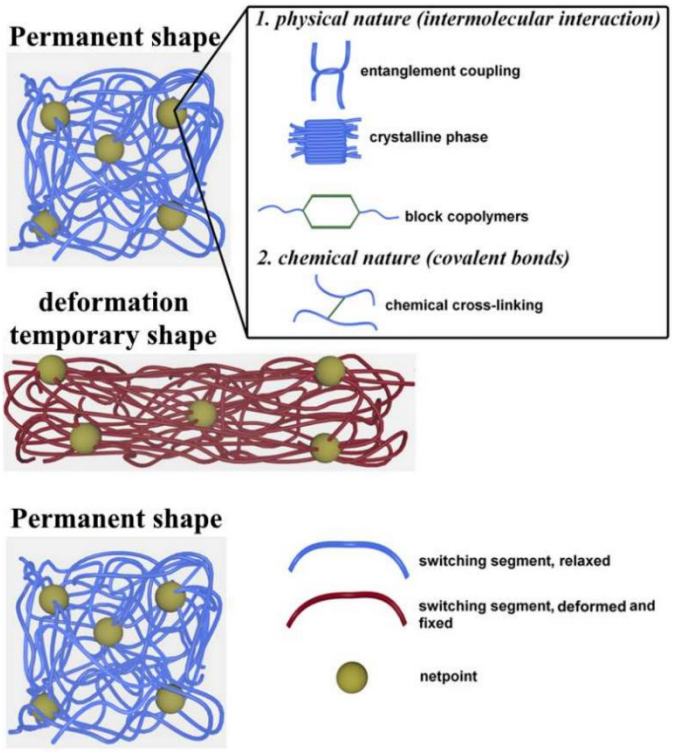

Figure 2.7: Schematic of entangled polymer chains with the netpoints. The netpoints act as an anchor to retain the original shape and the polymer chains can slide past each other to deform and retain the temporary shape[27].

2.2.2. Pre-straining sequence

Pre-straining is a set of thermomechanical processing steps that impart shape memory properties to the polymer. It consists of a series of thermomechanical loading and unloading steps[77,78] shown in Figure 2.8. In a prestraining process, a polymer undergoes mechanical deformation (ε_m) at a temperature above its T_g, followed by subsequent fixation of that deformation while unloading and decreasing the temperature[79,80]. Deformation at elevated temperature provides polymer chains with additional energy allowing them to move around the domain in an attempt to reduce the conformational energy. This movement is stopped when the

polymer is cooled below T_g while holding this new deformation. Once cooled, the chains stay at this higher energy chain conformation even after the removal of the applied deformation. Finally, the unloading process recovers some deformation due to the elasticity of the material and to some extent due to the thermal contraction at $T < T_g$. This process locks the polymer chains into a new configuration, thus providing a temporary shape (ε_u) to the polymer. The ability of a polymer to fix the mechanical deformation (ε_m) applied during the pre-straining process is calculated using shape fixity, (R_f) as[81]:

$$R_f = \frac{\varepsilon_u}{\varepsilon_m} \cdot 100\% \quad (1)$$

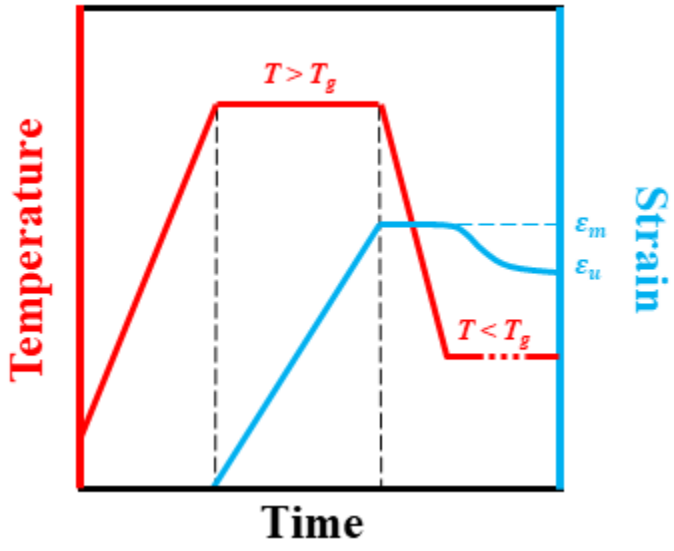

Figure 2.8: Schematic of thermomechanical load applied during pre-straining sequence. Red and blue represents temperature and strain respectively.

2.2.3. Shape recovery process

The end of the prestraining process is followed by recovery of the residual strain of polymer chains as shown in Figure 2.9. The residual energy of polymer chains due to the applied strain can

be recovered by raising the temperature of the polymer to a temperature above its T_g. At this temperature, the polymer chains have increased mobility, resulting in chain relaxation where they can move around until they find a lower energy conformation. The chain relaxation occurs at temperatures above T_g where the end-to-end length of the chain decreases in order to return back to a thermodynamically favored lower energy conformation. The net effect of this relates to the bulk material returning to its original shape ($\varepsilon_r \sim 0$). The polymer chains move towards a lower energy state achieved before prestraining and in the process recovers the residual strain. The efficiency of the recovery process is calculated through shape recovery (R_r) according to the relation[81]:

$$R_r = \frac{\varepsilon_m - \varepsilon_r}{\varepsilon_m} \cdot 100\% \tag{2}$$

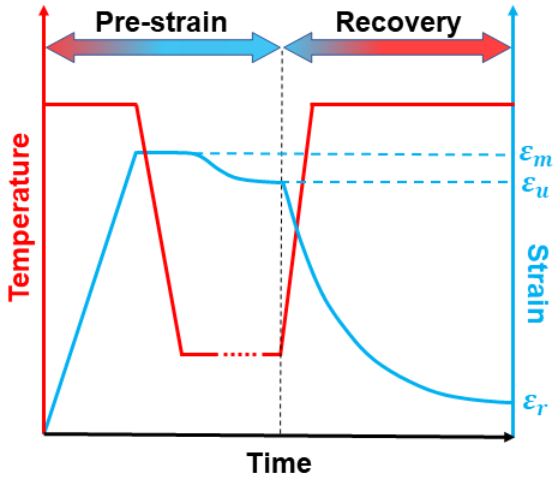

Figure 2.9: Thermomechanical loading depicting pre-straining and recovery sequences. Red and blue represents temperature and strain respectively during each procedure.

2.3. References

(1) Brinson, H. F.; Brinson, L. C. *Polymer Engineering Science and Viscoelasticity: An Introduction, Second Edition*; Springer US, 2015. https://doi.org/10.1007/978-1-4899-7485-3.

(2) Hutchinson, J. M. Physical Aging of Polymers. *Progress in Polymer Science* **1995**, *20* (4), 703–760. https://doi.org/10.1016/0079-6700(94)00001-I.

(3) Bhatia, S. Natural Polymers vs Synthetic Polymer. In *Natural Polymer Drug Delivery Systems: Nanoparticles, Plants, and Algae*; Bhatia, S., Ed.; Springer International Publishing: Cham, 2016; pp 95–118. https://doi.org/10.1007/978-3-319-41129-3_3.

(4) Baskaran, K.; Ali, M.; Gingrich, K.; Porter, D. L.; Chong, S.; Riley, B. J.; Peak, C. W.; Naleway, S. E.; Zharov, I.; Carlson, K. Sol-Gel Derived Silica: A Review of Polymer-Tailored Properties for Energy and Environmental Applications. *Microporous and Mesoporous Materials* **2022**, *336*, 111874. https://doi.org/10.1016/j.micromeso.2022.111874.

(5) Geyer, R.; Jambeck, J. R.; Law, K. L. Production, Use, and Fate of All Plastics Ever Made. *Science Advances* **2017**, *3* (7), e1700782. https://doi.org/10.1126/sciadv.1700782.

(6) Physical, Thermal, and Mechanical Properties of Polymers. In *Biosurfaces*; John Wiley & Sons, Ltd, 2014; pp 329–344. https://doi.org/10.1002/9781118950623.app1.

(7) Rennie, A. R. Thermoplastics and Thermosets. In *Mechanical Properties and Testing of Polymers: An A–Z Reference*; Swallowe, G. M., Ed.; Polymer Science and Technology Series; Springer Netherlands: Dordrecht, 1999; pp 248–248. https://doi.org/10.1007/978-94-015-9231-4_53.

(8) Tadmor, Z.; Gogos, C. G. *Principles of Polymer Processing*, 2nd ed., Rev. ed.; Wiley-Interscience: Hoboken, N.J, 2006.

(9) Gennes, P. G. de. *Scaling Concepts in Polymer Physics*; Cornell University Press: Ithaca, N.Y, 1979.

(10) de Gennes, P. Entangled Polymers. *Physics Today* **1983**, *36* (6), 33–39. https://doi.org/10.1063/1.2915700.

(11) Strobl, G. R. *The Physics of Polymers: Concepts for Understanding Their Structures and Behavior*, 3rd rev. and Expanded ed.; Chemistry and Materials Science (Springer-11644; ZDB-2-CMS); Springer-Verlag Berlin Heidelberg Springer e-books: Berlin, Heidelberg, 2007.

(12) Rubinstein, M.; Colby, R. H. *Polymer Physics*; Oxford University Press: Oxford ; New York, 2003.

(13) Austen Angell, C.; Sivarajan, S. Glass Transition☆. In *Reference Module in Materials Science and Materials Engineering*; Elsevier, 2017. https://doi.org/10.1016/B978-0-12-803581-8.03155-6.

(14) Liu, Y.; Miskiewicz, M.; Escuti, M. J.; Genzer, J.; Dickey, M. D. Three-Dimensional Folding of Pre-Strained Polymer Sheets via Absorption of Laser Light. *Journal of Applied Physics* **2014**, *115* (20). https://doi.org/10.1063/1.4880160.

(15) Chaudhari, R.; Vora, J. J.; Parikh, D. M. A Review on Applications of Nitinol Shape Memory Alloy. **2021**, 123–132. https://doi.org/10.1007/978-981-33-4176-0_10.

(16) Srivastava, V.; Chester, S. A.; Anand, L. Thermally Actuated Shape-Memory Polymers: Experiments, Theory, and Numerical Simulations. *Journal of the Mechanics and Physics of Solids* **2010**, *58* (8), 1100–1124. https://doi.org/10.1016/J.JMPS.2010.04.004.

(17) Voit, W.; Ware, T.; Dasari, R. R.; Smith, P.; Danz, L.; Simon, D.; Barlow, S.; Marder, S. R.; Gall, K. High-Strain Shape-Memory Polymers. *Advanced Functional Materials* **2010**, *20* (1), 162–171. https://doi.org/10.1002/adfm.200901409.

(18) Hubbard, A. M.; Mailen, R. W.; Zikry, M. A.; Dickey, M. D.; Genzer, J. Controllable Curvature from Planar Polymer Sheets in Response to Light. *Soft Matter* **2017**, *13* (12), 2299–2308. https://doi.org/10.1039/C7SM00088J.

(19) Lee, Y.; Lee, H.; Hwang, T.; Lee, J.-G.; Cho, M. Sequential Folding Using Light-Activated Polystyrene Sheet. *Scientific Reports* **2015**, *5* (1), 16544. https://doi.org/10.1038/srep16544.

(20) Murugan, M. S.; Rao, S.; Chiranjeevi, M. C.; Revathi, A.; Rao, K. V.; Srihari, S.; Dayananda, G. N. Actuation of Shape Memory Polymer Composites Triggered by Electrical Resistive Heating. *Original Article Journal of Intelligent Material Systems and Structures* **2017**, *28* (17), 2363–2371. https://doi.org/10.1177/1045389X17689944.

(21) Luo, X.; Mather, P. T. Conductive Shape Memory Nanocomposites for High Speed Electrical Actuation. *Soft Matter* **2010**, *6* (10), 2146. https://doi.org/10.1039/c001295e.

(22) Fornell, J. Magnetic Shape Memory Composites. In *Encyclopedia of Materials: Composites*; Brabazon, D., Ed.; Elsevier: Oxford, 2021; pp 487–495. https://doi.org/10.1016/B978-0-12-803581-8.11867-3.

(23) Fu, F.; Hu, L. 15 - Temperature Sensitive Colour-Changed Composites. In *Advanced High Strength Natural Fibre Composites in Construction*; Fan, M., Fu, F., Eds.; Woodhead Publishing, 2017; pp 405–423. https://doi.org/10.1016/B978-0-08-100411-1.00015-7.

(24) Abrahams, S. C.; Nassau, K. Piezoelectric Materials. In *Concise Encyclopedia of Advanced Ceramic Materials*; Brook, R., Ed.; Pergamon: Oxford, 1991; pp 351–354. https://doi.org/10.1016/B978-0-08-034720-2.50097-6.

(25) Behera, A. Piezoelectric Materials. In *Advanced Materials: An Introduction to Modern Materials Science*; Behera, A., Ed.; Springer International Publishing: Cham, 2022; pp 43–76. https://doi.org/10.1007/978-3-030-80359-9_2.

(26) Zende, R.; Ghase, V.; Jamdar, V. A Review on Shape Memory Polymers. *Polymer-Plastics Technology and Materials* **2022**. https://doi.org/10.1080/25740881.2022.2121216.

(27) Dayyoub, T.; Maksimkin, A. V.; Filippova, O. V.; Tcherdyntsev, V. V.; Telyshev, D. V. Shape Memory Polymers as Smart Materials: A Review. *Polymers (Basel)* **2022**, *14* (17), 3511. https://doi.org/10.3390/polym14173511.

(28) Hodgson, D. E. Shape Memory Alloys; 1990.

(29) Bahl, S.; Nagar, H.; Singh, I.; Sehgal, S. Smart Materials Types, Properties and Applications: A Review. *Materials Today: Proceedings* **2020**, *28*, 1302–1306. https://doi.org/10.1016/j.matpr.2020.04.505.

(30) Mitchell, A.; Lafont, U.; Hołyńska, M.; Semprimoschnig, C. Additive Manufacturing — A Review of 4D Printing and Future Applications. *Additive Manufacturing* **2018**, *24*, 606–626. https://doi.org/10.1016/j.addma.2018.10.038.

(31) Huang, W. M.; Yang, B.; Zhao, Y.; Ding, Z. Thermo-Moisture Responsive Polyurethane Shape-Memory Polymer and Composites: A Review. *J. Mater. Chem.* **2010**, *20* (17), 3367–3381. https://doi.org/10.1039/B922943D.

(32) Liu, C.; Qin, H.; Mather, P. T. Review of Progress in Shape-Memory Polymers. *Journal of Materials Chemistry* **2007**, *17* (16), 1543–1558. https://doi.org/10.1039/b615954k.

(33) Hu, L.; Shu, T.; Wan, Y.; Fang, C.; Gao, F.; Serpe, M. J. Recent Advances in Stimuli-Responsive Polymers for Sensing and Actuation. *Mol. Syst. Des. Eng.* **2021**, *6* (2), 108–121. https://doi.org/10.1039/D0ME00133C.

(34) Hu, L.; Zhang, Q.; Li, X.; Serpe, M. J. Stimuli-Responsive Polymers for Sensing and Actuation. *Mater. Horiz.* **2019**, *6* (9), 1774–1793. https://doi.org/10.1039/C9MH00490D.

(35) Feninat, F. E.; Laroche, G.; Fiset, M.; Mantovani, D. Shape Memory Materials for Biomedical Applications. **2002**. https://doi.org/10.1002/1527-2648.

(36) Sokolowski, W.; Hayashi, S.; Metcalfe, A.; Raymond, J. Medical Applications of Shape Memory Polymers. https://doi.org/10.1088/1748-6041/2/1/S04.

(37) Phan, P. T.; Thai, M. T.; Hoang, T. T.; Davies, J.; Nguyen, C. C.; Phan, H.-P.; Lovell, N. H.; Do, T. N. Smart Textiles Using Fluid-Driven Artificial Muscle Fibers. *Sci Rep* **2022**, *12* (1), 11067. https://doi.org/10.1038/s41598-022-15369-2.

(38) Tan, Y. J.; Wu, J.; Li, H.; Tee, B. C. K. Self-Healing Electronic Materials for a Smart and Sustainable Future. *ACS Appl. Mater. Interfaces* **2018**, *10* (18), 15331–15345. https://doi.org/10.1021/acsami.7b19511.

(39) Bekas, D. G.; Tsirka, K.; Baltzis, D.; Paipetis, A. S. Self-Healing Materials: A Review of Advances in Materials, Evaluation, Characterization and Monitoring Techniques. *Composites Part B: Engineering* **2016**, *87*, 92–119. https://doi.org/10.1016/j.compositesb.2015.09.057.

(40) Zhang, D.; Liu, L.; Xu, P.; Zhao, Y.; Li, Q.; Lan, X.; Zou, X.; Li, Y.; He, Y.; Liu, Y.; Leng, J. Ancient Papyrus Scroll-Inspired Self-Deployable Mechanism Based on Shape Memory Polymer Composites for Mars Explorations. *Composite Structures* **2023**, *304*, 116391. https://doi.org/10.1016/j.compstruct.2022.116391.

(41) Scarpa, F.; Alderson, A.; Ruzzene, M.; Wojciechowski, K. Auxetics in Smart Systems and Structures 2015. *Smart Mater. Struct.* **2016**, *25* (5), 050301. https://doi.org/10.1088/0964-1726/25/5/050301.

(42) Acuna, D.; Gutiérrez, F.; Silva, R.; Palza, H.; Nunez, A. S.; Düring, G. A Three Step Recipe for Designing Auxetic Materials on Demand. *Commun Phys* **2022**, *5* (1), 1–9. https://doi.org/10.1038/s42005-022-00876-5.

(43) Yang, Y. W.; Ju, C. K.; Soh, C. K. Smart Beams: A Semi-Analytical Method. In *Smart Materials in Structural Health Monitoring, Control and Biomechanics*; Soh, C.-K., Yang, Y., Bhalla, S., Eds.; Advanced Topics in Science and Technology in China; Springer: Berlin, Heidelberg, 2012; pp 299–332. https://doi.org/10.1007/978-3-642-24463-6_8.

(44) Altabey, W. A.; Noori, M. A Dynamic Analysis of Smart and Nanomaterials for New Approaches to Structural Control and Health Monitoring. *Materials (Basel)* **2023**, *16* (9), 3567. https://doi.org/10.3390/ma16093567.

(45) Halonen, N.; Pálvölgyi, P. S.; Bassani, A.; Fiorentini, C.; Nair, R.; Spigno, G.; Kordas, K. Bio-Based Smart Materials for Food Packaging and Sensors – A Review. *Front. Mater.* **2020**, *7*, 521914. https://doi.org/10.3389/fmats.2020.00082.

(46) Kuzubaşoğlu, B. A.; Tekçin, M.; Bahadır, S. K. Electronic Textiles (E-Textiles): Fabric Sensors and Material-Integrated Wearable Intelligent Systems. In *Encyclopedia of Sensors and*

Biosensors (First Edition); Narayan, R., Ed.; Elsevier: Oxford, 2023; pp 80–100. https://doi.org/10.1016/B978-0-12-822548-6.00085-6.

(47) More, G. R.; Ohatkar, S. N. Effective Vibration Damping Using Self-Tuning Smart Material. In *Micro-Electronics and Telecommunication Engineering*; Sharma, D. K., Balas, V. E., Son, L. H., Sharma, R., Cengiz, K., Eds.; Lecture Notes in Networks and Systems; Springer: Singapore, 2020; pp 65–74. https://doi.org/10.1007/978-981-15-2329-8_7.

(48) Xu, Z.-D.; Chen, Z.-H.; Huang, X.-H.; Zhou, C.-Y.; Hu, Z.-W.; Yang, Q.-H.; Gai, P.-P. Recent Advances in Multi-Dimensional Vibration Mitigation Materials and Devices. *Frontiers in Materials* **2019**, *6*.

(49) Fox, G. W.; Fink, G. A. The Piezoelectric Properties of Quartz and Tourmaline. *Physics* **2004**, *5* (10), 302–306. https://doi.org/10.1063/1.1745214.

(50) Uchino, K. Piezoelectric Actuators. In *Encyclopedia of Materials: Electronics*; Haseeb, A. S. M. A., Ed.; Academic Press: Oxford, 2023; pp 151–179. https://doi.org/10.1016/B978-0-12-819728-8.00128-5.

(51) Rubio-Marcos, F.; Fernandez, J. F.; Ochoa, D. A.; García, J. E.; Rojas-Hernandez, R. E.; Castro, M.; Ramajo, L. Understanding the Piezoelectric Properties in Potassium-Sodium Niobate-Based Lead-Free Piezoceramics: Interrelationship between Intrinsic and Extrinsic Factors. *Journal of the European Ceramic Society* **2017**, *37* (11), 3501–3509. https://doi.org/10.1016/j.jeurceramsoc.2017.04.045.

(52) Lang, S. B.; Tofail, S. a. M.; Kholkin, A. L.; Wojtaś, M.; Gregor, M.; Gandhi, A. A.; Wang, Y.; Bauer, S.; Krause, M.; Plecenik, A. Ferroelectric Polarization in Nanocrystalline

Hydroxyapatite Thin Films on Silicon. *Sci Rep* **2013**, *3* (1), 2215. https://doi.org/10.1038/srep02215.

(53) Markus, D. T.; Hayes, M. C. Piezoelectric Sensor for Vision Correction. US20160030160A1, February 4, 2016. https://patents.google.com/patent/US20160030160/en (accessed 2023-08-11).

(54) Wang, Y.; Yu, Y.; Wei, X.; Narita, F. Self-Powered Wearable Piezoelectric Monitoring of Human Motion and Physiological Signals for the Postpandemic Era: A Review. *Advanced Materials Technologies* **2022**, *7* (12), 2200318. https://doi.org/10.1002/admt.202200318.

(55) Sezer, N.; Koç, M. A Comprehensive Review on the State-of-the-Art of Piezoelectric Energy Harvesting. *Nano Energy* **2021**, *80*, 105567. https://doi.org/10.1016/j.nanoen.2020.105567.

(56) Bar-Cohen, Y. EAP History, Current Status, and Infrastructure. *Electroactive polymer (EAP) actuators as artificial muscles* **2001**, 3–44.

(57) Maksimkin, A. V.; Dayyoub, T.; Telyshev, D. V.; Gerasimenko, A. Yu. Electroactive Polymer-Based Composites for Artificial Muscle-like Actuators: A Review. *Nanomaterials (Basel)* **2022**, *12* (13), 2272. https://doi.org/10.3390/nano12132272.

(58) Mirfakhrai, T.; Madden, J. D. W.; Baughman, R. H. Polymer Artificial Muscles. *Materials Today* **2007**, *10* (4), 30–38. https://doi.org/10.1016/S1369-7021(07)70048-2.

(59) Ning, C.; Zhou, Z.; Tan, G.; Zhu, Y.; Mao, C. Electroactive Polymers for Tissue Regeneration: Developments and Perspectives. *Prog Polym Sci* **2018**, *81*, 144–162. https://doi.org/10.1016/j.progpolymsci.2018.01.001.

(60) Wang, R.; Zhang, C.; Tan, W.; Yang, J.; Lin, D.; Liu, L. Electroactive Polymer-Based Soft Actuator with Integrated Functions of Multi-Degree-of-Freedom Motion and Perception. *Soft Robotics* **2023**, *10* (1), 119–128. https://doi.org/10.1089/soro.2021.0104.

(61) Riccio, A.; Sellitto, A.; Ameduri, S.; Concilio, A.; Arena, M. Chapter 24 - Shape Memory Alloys (SMA) for Automotive Applications and Challenges. In *Shape Memory Alloy Engineering (Second Edition)*; Concilio, A., Antonucci, V., Auricchio, F., Lecce, L., Sacco, E., Eds.; Butterworth-Heinemann: Boston, 2021; pp 785–808. https://doi.org/10.1016/B978-0-12-819264-1.00024-8.

(62) Velvaluri, P.; Soor, A.; Plucinsky, P.; de Miranda, R. L.; James, R. D.; Quandt, E. Origami-Inspired Thin-Film Shape Memory Alloy Devices. *Sci Rep* **2021**, *11* (1), 10988. https://doi.org/10.1038/s41598-021-90217-3.

(63) Mohd Jani, J.; Leary, M.; Subic, A.; Gibson, M. A. A Review of Shape Memory Alloy Research, Applications and Opportunities. *Materials & Design (1980-2015)* **2014**, *56*, 1078–1113. https://doi.org/10.1016/j.matdes.2013.11.084.

(64) Dolce, M.; Cardone, D. Mechanical Behaviour of Shape Memory Alloys for Seismic Applications 2. Austenite NiTi Wires Subjected to Tension. *International Journal of Mechanical Sciences* **2001**, *43* (11), 2657–2677. https://doi.org/10.1016/S0020-7403(01)00050-9.

(65) Abdelrahman, K.; El-Hacha, R. Experimental Investigation of RC Columns Confined with Ni–Ti Shape Memory Alloy Wires versus CFRP Sheets. *Can. J. Civ. Eng.* **2021**, *48* (8), 925–940. https://doi.org/10.1139/cjce-2019-0511.

(66) Barras, C. D. J.; Myers, K. A. Nitinol – Its Use in Vascular Surgery and Other Applications. *European Journal of Vascular and Endovascular Surgery* **2000**, *19* (6), 564–569. https://doi.org/10.1053/ejvs.2000.1111.

(67) Siegner, D.; Ibe, D. Clinical Application of Shape-Memory Alloys in Orthodontics. In *Shape Memory Implants*; Yahia, L., Ed.; Springer: Berlin, Heidelberg, 2000; pp 210–228. https://doi.org/10.1007/978-3-642-59768-8_15.

(68) Giba, J. J.; Walcott, G. P.; Ideker, R. E.; Richardson, D. A. Shape Memory Catheter. US5997526A, December 7, 1999. https://patents.google.com/patent/US5997526A/en (accessed 2023-08-11).

(69) Mailen, R. W.; Dickey, M. D.; Genzer, J.; Zikry, M. Effects of Thermo-Mechanical Behavior and Hinge Geometry on Folding Response of Shape Memory Polymer Sheets. *Journal of Applied Physics* **2017**, *122* (19), 195103. https://doi.org/10.1063/1.5000040.

(70) Tobushi, H.; Hayashi, S.; Sugimoto, Y.; Date, K. Two-Way Bending Properties of Shape Memory Composite with SMA and SMP. *Materials* **2009**, *2* (3), 1180. https://doi.org/10.3390/ma2031180.

(71) Tolley, M. T.; Felton, S. M.; Miyashita, S.; Aukes, D.; Rus, D.; Wood, R. J. Self-Folding Origami: Shape Memory Composites Activated by Uniform Heating. *Smart Materials and Structures* **2014**, *23* (9), 094006. https://doi.org/10.1088/0964-1726/23/9/094006.

(72) Zhao, W.; Liu, L.; Lan, X.; Su, B.; Leng, J.; Liu, Y. Adaptive Repair Device Concept with Shape Memory Polymer. *Smart Materials and Structures* **2017**, *26* (2), 025027. https://doi.org/10.1088/1361-665X/aa5595.

(73) Lan, X.; Liu, Y.; Lv, H.; Wang, X.; Leng, J.; Du, S. Fiber Reinforced Shape-Memory Polymer Composite and Its Application in a Deployable Hinge. *Smart Mater. Struct.* **2009**, *18* (2), 024002. https://doi.org/10.1088/0964-1726/18/2/024002.

(74) Hu, J.; Chen, S. A Review of Actively Moving Polymers in Textile Applications. *Journal of Materials Chemistry* **2010**, *20* (17), 3346–3355. https://doi.org/10.1039/b922872a.

(75) Danielson, C.; Mehrnezhad, A.; Yekrangsafakar, A.; Park, K. Fabrication and Characterization of Self-Folding Thermoplastic Sheets Using Unbalanced Thermal Shrinkage. *Soft Matter* **2017**, *13* (23), 4224–4230. https://doi.org/10.1039/C6SM02637K.

(76) Na, J. H.; Evans, A. A.; Bae, J.; Chiappelli, M. C.; Santangelo, C. D.; Lang, R. J.; Hull, T. C.; Hayward, R. C. Programming Reversibly Self-Folding Origami with Micropatterned Photo-Crosslinkable Polymer Trilayers. *Advanced Materials* **2015**, *27* (1), 79–85. https://doi.org/10.1002/adma.201403510.

(77) Atli, B.; Gandhi, F.; Karst, G. Thermomechanical Characterization of Shape Memory Polymers. *Journal of Intelligent Material Systems and Structures* **2009**, *20* (1), 87–95. https://doi.org/10.1177/1045389X07086689.

(78) Shojaei, A.; Xu, W.; Yan, C.; Yang, Q.; Li, G. Insight in Thermomechanical Constitutive Modeling of Shape Memory Polymers. *Frontiers in Mechanical Engineering* **2022**, *8*, 83. https://doi.org/10.3389/FMECH.2022.956129/BIBTEX.

(79) Mailen, R. W.; Liu, Y.; Dickey, M. D.; Zikry, M.; Genzer, J. Modelling of Shape Memory Polymer Sheets That Self-Fold in Response to Localized Heating. *Soft Matter* **2015**, *11* (39), 7827–7834. https://doi.org/10.1039/C5SM01681A.

(80) Wang, Z.; Liu, J.; Guo, J.; Sun, X.; Xu, L. The Study of Thermal, Mechanical and Shape Memory Properties of Chopped Carbon Fiber-Reinforced TPI Shape Memory Polymer Composites. *Polymers* **2017**, *9* (11), 594. https://doi.org/10.3390/POLYM9110594.

(81) Tobushi, H.; Hayashi, S.; Ikai, A.; Hara, H.; Co, R. Thermomechanical Properties of Shape Memory Polymers of Polyurethane Series and Their Applications. *Journal de Physique IV Colloque* **1996**, *111* (C1), 6. https://doi.org/10.1051/jp4:1996136.

Chapter 3

Computational modeling of hot rolling process for biaxial pre-straining of shape memory polymer sheets

Abstract

Shape recovery of SMPs enable planar sheets to be converted to 3D structures in response to external stimuli such as heat. This shape change results from viscoelastic recovery of stored strain at higher temperature, that was imparted to the material via a pre-straining sequence. The pre-straining sequence consists of deforming the polymer at an elevated temperature and cooling it to lock in a temporary, deformed shape. The imparted strain can be recovered by reheating the polymer above its glass transition temperature (T_g) uniformly to shrink. Biaxially pre-straining the polymer sheets has been developed at an industrial scale for few types of materials and provide limited opportunities to scale down to a laboratory setup for specific applications such as temperature and strain controlled shape recovery applications. In addition, previous research efforts have focused primarily on uniaxial pre-straining by stretching the material, which limits the possibilities for transforming the material to 3D structures through origami principles. However, limited research has been conducted towards lab-scale, biaxial pre-straining of polymer sheets, which can provide increased shape recovery efficiency and pre-strain a wider variety of polymers that can be selected based on their applications. In this chapter, we build a computational model of a lab-scale shape-memory polymer pre-straining process, wherein a heated polystyrene is pre-strained by passing it through two rollers, thereby pre-straining in two directions, followed by quenching. We conduct a parametric pre-straining analysis by varying the process parameters such as roller gap, roller speed, feed rate and working temperature and quantify the effects of process parameters on the amount of pre-strain imparted to the polymer. Further, we evaluate the

shape memory performance of the SMP as a result of varying process parameters. The results obtained through this study is useful in studying various processing parameters in biaxial pre-straining process by pre-straining a variety of application specific polymers and will be used to verify the experimental analysis.

3.1. Introduction

Pre-straining is a series of thermomechanical processing steps, intended to modify a polymer's structural configuration that leads to tailorable material properties, such as stiffness, toughness[1,2]. Pre-straining involves subjecting the polymer chains to controlled mechanical deformation at an elevated temperature, which aligns them in a desired orientation[3]. Polymer chains can be aligned through stretching[4], compressing[5], blow molding[6] and rolling[7], before they take their final shape. The alignment of polymer chains improves mechanical properties such as strength and toughness[8], enhances barrier properties of polymer films[9,10] and improves dimensional stability[11,12]. Pre-strained polymers have been used in various applications such as blow molded PET bottles, flexible electronics[13] and fabric-reinforced composites[14] and have meet the performance requirements in industries such as automotive[15] and aerospace[16].

During the pre-straining process, the polymer is heated to an elevated temperature, usually above its glass transition temperature $(T > T_g)$, which increases the mobility of its molecular chains[17]. The increased mobility allows the polymer chains to align more easily when subjected to a controlled mechanical deformation, such as stretching, compressing or twisting[18,19]. Mechanical deformation can be applied uniaxially in a longitudinal direction, or biaxially in both longitudinal and transverse direction[20]. Tensile mechanical deformation at elevated temperature aligns the polymer chains along the direction of the applied force[18]. Following the deformation, the polymer is immediately cooled below its glass transition temperature $(T < T_g)$, where the chain mobility

is reduced, and the alignment of the polymer chains can be preserved in the temporarily deformed shape[21,22]. In polymers, biaxial pre-straining can enhance mechanical properties more effectively compared to uniaxial pre-straining as it involves subjecting the polymer chains to align along both longitudinal and transverse axes[23,24]. As a result, the material gains improved mechanical performance in both directions[20]. The alignment of polymer chains after the pre-straining process can also be used for temperature responsive shape recovery or actuator purposes through the application of external stimuli[21]. The application of external stimuli increases the temperature of the polymer, thus increasing the mobility of the polymer chains. This gain in chain mobility gradually releases the stored pre-strain, thereby recovering the polymer to the undeformed shape. It is to be noted that only the elastic portion of the applied pre-strain is recovered at temperatures above T_g, as any plastic deformation will permanently align the polymer chains beyond elastic recovery. The pre-straining process is a precursor to the SME of a polymer and it has been used in various applications such as self-folding origami[25,26], soft robotics[27,28] and deployable structures[29,30].

In recent years, numerous groups have worked on biaxially pre-straining of polymer sheets and studied the effects of biaxial stretching on the performance of a polymer. Notable works include the development of a stretching module that can be adapted to any uniaxial tensile testing machine[31]; plastic deformation of biaxially pre-strained polymers studied through the rolling process[32]; and step-wise rolling with multiple passing of polymers in different orientation.[20]. Previous studies have primarily focused on plastic deformation during the rolling process and observed the mechanical performance of the pre-strained polymers. However, limited study has been performed on evaluating the performance of polystyrene undergoing biaxial pre-straining process. With the correct understanding of biaxial pre-straining of a variety of polymers, we could

select the right polymer for a specific application, such as thermomechanical shape memory applications. The shape memory cycle is sensitive to processing parameters during pre-straining process, such as processing temperature, strain rate and amount of deformation[3]. Plastic deformation of a polymer is disadvantageous to its mechanical strength and is particularly detrimental for applications including SME of a polymer, as it cannot recover the plastic deformation applied during the pre-straining process. Furthermore, polymer rolling is advantageous to hot pressing, as rolling provides uniformity in the production of sheet and films and is a continuous process that is suitable for continuous production line while hot pressing requires some downtime between each compression and introduces shear bands on the surface of the polymers[33,34]. Therefore, study of polymers undergoing elastic deformation during biaxial pre-straining is necessary in order to improve the shape recovery performance and generate the most optimized temporary shape to a polymer that can be recovered for shape memory applications.

In this chapter, a computational biaxial rolling model was developed, and the pre-straining process was investigated towards the goal of optimizing the shape recovery performance for SMPs. A previously developed 3D, nonlinear finite element framework was used to model the rolling process[21]. The material properties of polystyrene were used as an input for the pre-straining process, and the roller was modeled to be analytically rigid aluminum. Material properties such as mechanical properties, viscoelastic properties, and thermal properties of polystyrene were input along with the boundary conditions associated with the rolling process. The computational approach involves passing the polymer workpiece between two rollers at a specific feed rate at a temperature above its glass transition temperature ($T > T_g$), and immediately cooling to below its T_g ($T < T_g$) after exiting the roller. The pre-strained workpiece is further investigated for the effects

of process variables such as roller gap, roller speed, feed rate and temperature on shape recovery performance of SMP.

3.2. Computational approach

A general rolling schematic is shown in Figure 3.1a. Consider a pair of rollers of radius R rotating at an angular velocity of ω_r. A workpiece with an initial height h_i, width w_i *(into the page)*, and length L_i , as shown in Figure 3.1b, is moving towards the roller at a speed v_i. The coefficient of friction between the roller and the workpiece is μ and the projected length of the arc of contact between the roller and the workpiece is L_p. The workpiece is compressed to a final height h_f(which may be different than the gap between the rollers), width w_f, and length L_f after exiting the roller. The change in height of the workpiece $(\Delta h = h_i - h_f)$ is used to compute the pre-strain in y-axis and the change in width of the workpiece $(\Delta w = w_i - w_f)$ is used to compute the pre-strain in z-axis. The change in the workpiece's length, along x-axis, is negligible (<1%) due to the absence of applied force in a longitudinal direction. The gap between the rollers, roller gap (g_r), is varied to apply varying amount of pre-strain to the workpiece during the rolling process.

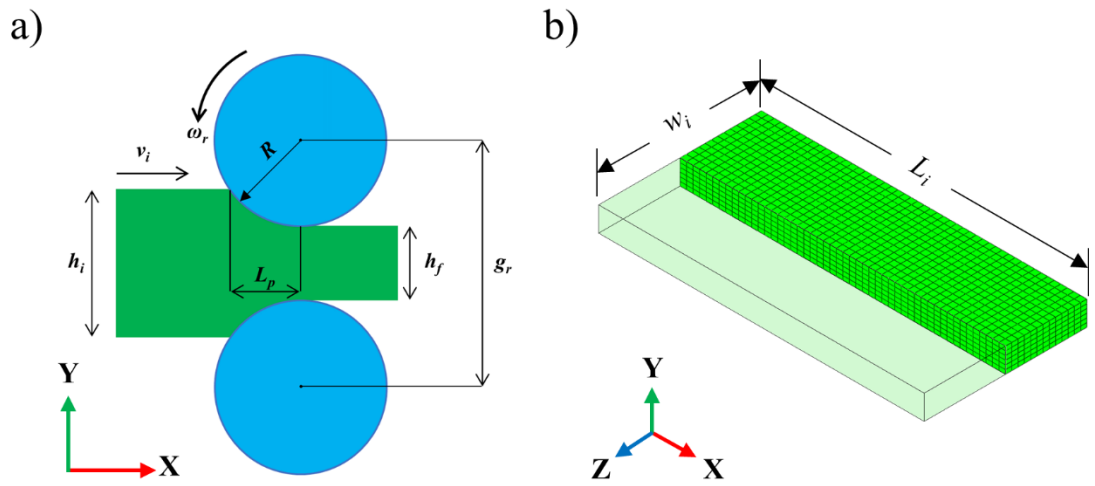

Figure 3.1: a) Schematic of rolling process. The workpiece is biaxially compressed at $T > T_g$ during the rolling process and is cooled to $T < T_g$ after the compression to store the applied pre-strain. b) The workpiece used in computational analysis. The workpiece has midplane symmetry about the xy-plane.

Throughout the rolling process, the workpiece undergoes viscoelastic deformation at $T > T_g$, the viscoelastic deformation is caused due to deviatoric strain, therefore, the entire process is a constant volume process and follows volume conservation law[35] according to the relation:

$$h_i w_i L_i = h_f w_f L_f \tag{1}$$

The prevalent theory on rolling assumes the width to be sufficiently large compared to the projected length of arc of contact between the roller and the workpiece $(w > L_p)$, that the width is considered constant throughout the rolling process[36]. The decrease in final height of the workpiece therefore increases the final length according to Equation 1. Furthermore, it is also assumed that the workpiece undergoes plastic deformation during the rolling process[6]. However, both of these assumptions need to be updated for this work as our model consists of a workpiece

that has a comparable width to the projected length of arc of contact between the roller and the workpiece, thereby assuming the width to vary during the rolling process. In addition, we are only applying elastic and viscoelastic deformation, instead of plastic deformation to the workpiece for shape recovery applications.

The assumptions and boundary conditions for this model are:

a) The roller is an analytical rigid element,

b) The roller has an angular velocity ω_r,

c) The workpiece has a translational velocity of v_i towards the positive x-axis.

The physical and mechanical material properties used are density *(ρ)*, specific heat capacity *(C_p)*, thermal conductivity *(k)*, Young's modulus *(E)*, Poisson's ratio *(v)*, viscoelastic component represented by dimensionless relaxation moduli (g_i), and relaxation times (τ_i).

The underlying viscoelastic response is evaluated through a previously developed[37] 3D, nonlinear finite element framework. A viscoelastic material model was utilized to account for the time dependent mechanical behavior of the SMP. An experimentally obtained viscoelastic master curve is modeled by a Prony series[21], which requires dimensionless relaxation moduli, g_i, and relaxation times, τ_i, to calculate the storage modulus, *G'*, and loss modulus, *G''*, according to[38]:

$$G'(\omega) = G_0(1 - \sum_{i=1}^{n} g_i) + G_0 \sum_{i=1}^{n} \frac{g_i (2\pi\omega\tau_i)^2}{1+ (2\pi\omega\tau_i)^2} \quad (2)$$

$$G''(\omega) = G_0 \sum_{i=1}^{n} \frac{g_i (2\pi\omega\tau_i)}{1+ (2\pi\omega\tau_i)^2} \quad (3)$$

$$tan\,\delta = \frac{G''(\omega)}{G'(\omega)} \quad (4)$$

where G_0 is the instantaneous shear modulus, ω is the frequency in Hz and $tan\delta$ indicates the amount of energy dissipated.

The relaxation times are temperature dependent and is updated for the viscoelastic material model as the temperature changes using the WLF equation[39]:

$$log(a_T) = -\frac{C_1 (T - T_g)}{C_2 + (T - T_g)} \quad (5)$$

where, a_T is the shift factor for the time and temperature dependent properties, C_1 and C_2 are constants, T is the temperature and T_g is the glass transition temperature. For polystyrene, the values of C_1 = 17.44; C_2 = 51.6 and T_g = 103°C was used[17].

The viscoelastic material properties vary with thermal changes, which needs to be accounted for in the model. Therefore, in addition to the mechanical response, the thermal change is calculated according to:

$$\rho C_p \frac{\partial T}{\partial t} - \nabla \cdot (k \nabla T) = \dot{q}_t \quad (6)$$

where, $\dot{q}_t$ represent the total heat flux. The variables ρ, C_p and k are the density, specific heat capacity and thermal conductivity of the material, respectively.

The roller applies maximum strain (ε_m^x, and ε_m^y) to the workpiece at $T = T_g + 10°C$ during the rolling process, as shown in Figure 3.2a-b. The workpiece is cooled to $T = T_g - 10°C$ by applying temperature boundary condition after exiting the rollers. During this step, the workpiece shrinks a small amount on both directions due to the removal of the mechanical load, to a new temporary strain (ε_u^x, and ε_u^y), as shown in Figure 3.2c. The efficiency of the pre-straining sequence in each direction is evaluated through the shape fixity ratio (R_f) as[40]:

$$R_f = \frac{\varepsilon_u}{\varepsilon_m} \cdot 100\% \quad (7)$$

After the pre-straining step, the workpiece undergoes shape recovery step where it is uniformly heated to $T = Tg + 10°C$ to recover the applied pre-strain during the pre-straining process, as shown in Figure 3.2e-f and is evaluated as the recovery ratio[40]:

$$R_r = \frac{\varepsilon_m - \varepsilon_r}{\varepsilon_m} \cdot 100\% \tag{8}$$

where, ε_r is the recovered strain at the end of shape recovery process.

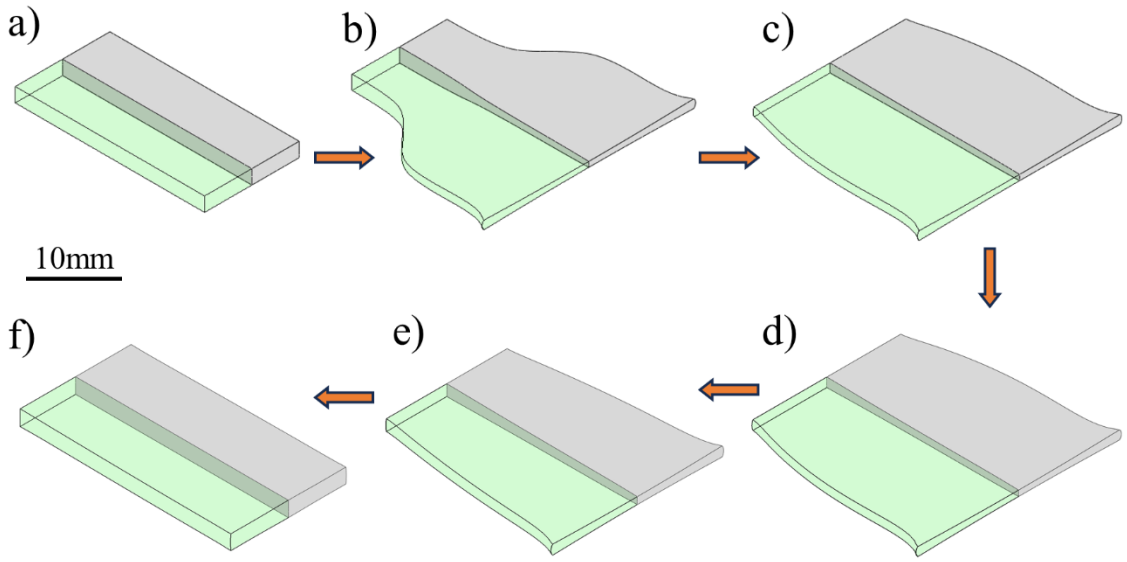

Figure 3.2: Polymer workpiece undergoing biaxially pre-straining process through a set of rollers (not shown). a) initial geometry of the workpiece at $T > T_g$, b) intermediate step during rolling, c) end of rolling and cooled to $T < T_g$, d) initial recovery process of the workpiece at $T > T_g$, e) intermediate shape recovery, f) complete shape recovery.

3.3. Results and discussion

We report the effects of processing parameters on the shape memory performance of the polymer undergoing pre-straining via biaxial rolling. All of the analyses are performed considering half width of the workpiece and is considered symmetric along the z-axis, as shown in Figure 3.1b. In section 3.3.1, we report the applied strain along the biaxial direction during rolling, followed by contact stress for a general case of rolling with frictional force in section 3.3.2. In section 3.3.3,

we report the effects of processing parameters on shape fixity ratio in biaxial direction and finally, in Section 3.3.4, we report the effects of heating rate on the shape recovery ratio of the pre-strained material.

3.3.1. Biaxial strain

In this section, we report the changes in biaxial strain applied during the rolling process analyzed according to section 3.2. For this analysis, a general rolling case with $\omega_r = 20$ rpm, change in height of workpiece, $\Delta h = 0.55 h_i$ is considered, the temperature of the workpiece is 105°C ($T > T_g$) and the polymer feed rate is 50mm/sec. The feed rate and the roller speed are selected as reported in literature[6,41]. During the rolling process, the workpiece is compressed (in y-axis), and following Equation 1, its width increases (in z-axis). The length of the workpiece alters as well; however, it is small (<1%) compared to changes in other axes. This is because the model is not applying any force to pull on the polymer, along its longitudinal axis, during rolling. The average strain experienced by the workpiece along the two axes during the rolling is shown in Figure 3.3. The rolling process is normalized with the total rolling time and changes in strain in y-axis (height of the workpiece) and z-axis (width of the workpiece) are shown in red and blue respectively. The strain applied in y-axis shows an initial increase in compressive strain until it reaches the maximum value of 55%, after which the workpiece exits the roller. After exiting the roller, the polymer recovers some of the strain due to the removal of the applied load from the roller and stays in this strain state. Similarly, the strain applied in z-axis shows an initial increase in tensile strain until it reaches the maximum value of 108%, after which the polymer begins to shrink in z-axis similar to that in y-axis. This is due to the fact that at temperatures slightly above T_g, the polymer starts to behave as a rubbery material[17] and undergoes a combination of viscoelastic and elastic recovery. The computational model specifies the Poisson's ratio to be close

to 0.5 at this temperature, therefore any changes in strain in one direction results in almost twice the change in another orthogonal direction.

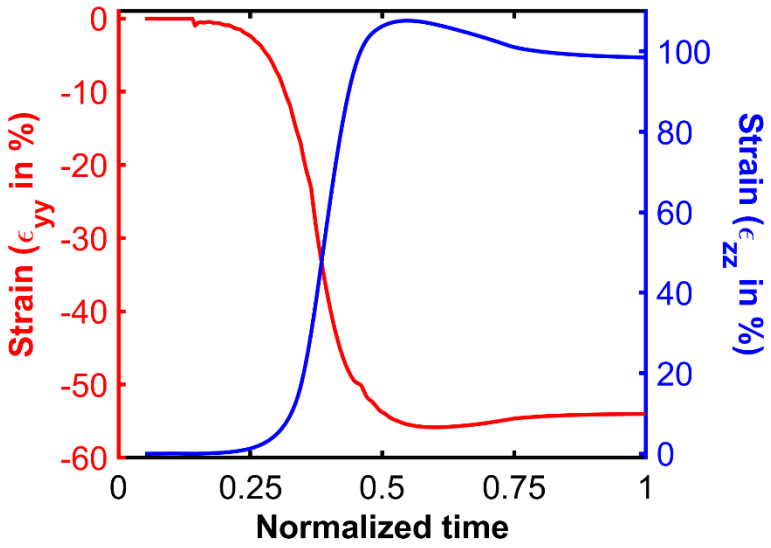

Figure 3.3: Biaxial strain during the rolling process along the y-axis (in red) and z-axis (in blue). The workpiece at temperature $T > T_g$, undergoing 55% shrinkage during the rolling process subsequently elongates its width to almost twice its original width. The polymer behaves as rubbery material at $T > T_g$, and the computational framework reproduce this behavior by setting the Poisson's ratio to be close to 0.5[17].

3.3.2. Frictional folding along the free edge

In this section, we analyze the effect of frictional force on the free edge of the workpiece undergoing rolling process. Unlike uniform compression, rolling consists of both compressive and shear force (produced due to friction between the roller and the workpiece) that further change the state of the polymer during the rolling process. To study this, we run similar analysis as mentioned in section 3.3.1 and evaluate the change in contact stress along z-axis. The contact stress on the surface of the polymer during the rolling process is defined as the contact normal force per unit area[38]. The contact stress applied on the upper surface of the workpiece, at normalized time … is

shown in Figure 3.4a. It shows that the stress being applied is highest at the center of the workpiece surface and gradually decreases with increasing width. The gradual decrease in the contact stress is explained by the combination of thickness compression and width elongation of the workpiece. As the workpiece undergoes rolling, the material along the free edge folds in on the upper and lower surfaces due to the frictional force applied between the roller and the polymer, as shown in inset of Figure 3.4a.

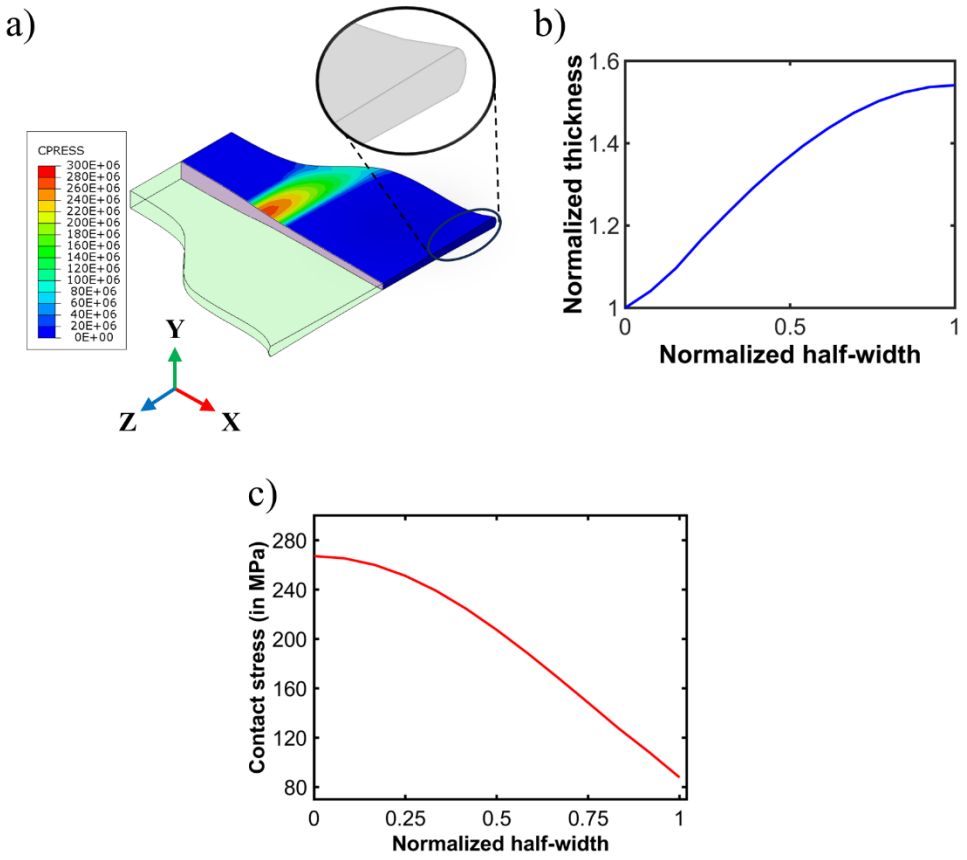

Figure 3.4 a) Contact stress variation along the width. The variation is caused by folding of materials on the edge due to friction between the roller and workpiece, b) this creates an increase in thickness along the half width. The increase in thickness and elongation of the width increases

the effective surface area and the pressure exerted from the roller is distributed over larger area thereby c) decreasing the contact stress.

This creates an uneven thickness distribution along the half-width of the workpiece. Figure 3.4b shows the thickness of the workpiece normalized to the minimum thickness along the half width of the workpiece. We see about 55% increase in the thickness of the workpiece along the z-axis due to the frictional force applied between the roller and the workpiece. The pressure exerted by the rolls is distributed across the width of the material and with the increase in its width, the same total force is spread over a larger area, leading to a lower pressure. The application of non-uniform pressure with a combination of increased thickness along the width and elongation of width itself results in a non-uniform pre-strain imparted to the material. This is therefore important to address this issue for the uniformity of pre-straining and recovery of the SMP.

3.3.3. Effects of processing parameters on shape fixity

In this section, we analyze the effect of processing parameters such as roller speed, amount of applied strain and polymer feed rate on the shape fixity of the pre-strained polymer. After removing the mechanical deformation applied to the polymer during a pre-straining process, the polymer recovers some of the applied strain. The amount of strain recovered is a measure of the efficiency of the pre-straining process and is evaluated by shape fixity ratio (R_f) according to Equation 7. To analyze the changes in shape fixity ratio, we conducted a parametric test by changing rolling parameters such as roller speed and polymer feed rate one at a time while keeping the other parameters unchanged. These parameters were selected as they either change the speed at which the polymer deforms or speed at which the polymer recovers after exiting the roller. These parameters change the polymer chain orientation and thereby change the efficiency of the pre-straining process.

We start first by analyzing the effects of roller speed on shape fixity ratio. For this analysis, we set the amount of applied strain to 55%, polymer feed rate at 5mm/sec and temperature at 105°C, similar to section 3.3.1. We evaluate the shape fixity in both orthogonal direction at the end of the rolling step for roller speed of 1, 5, 10, 20, 40 and 60 rpm. The shape fixity for all of these cases were between 90 and 95% in both directions. The reason for such small variations was that even with an increase in roller speed, the amount of pre-strain applied was essentially the same and the initial recovery after exiting the roller were similar in all conditions.

Next, we study the effects of material feed rate on shape fixity ratio. This analysis evaluates the speed at which the material is pushed through the roller and its subsequent recovery after exiting the roller. For this analysis, we set the amount of applied strain to 55%, roller speed at 20rpm and temperature at 105°C, similar to section 3.3.1. We evaluate the shape fixity in both orthogonal directions at the end of the rolling step for material speed of 1, 2, 5, 10, 25, 50, and 100 mm/sec and report the average shape fixity ratio. The change in shape fixity ratio with normalized rolling time is shown in Figure 3.5.

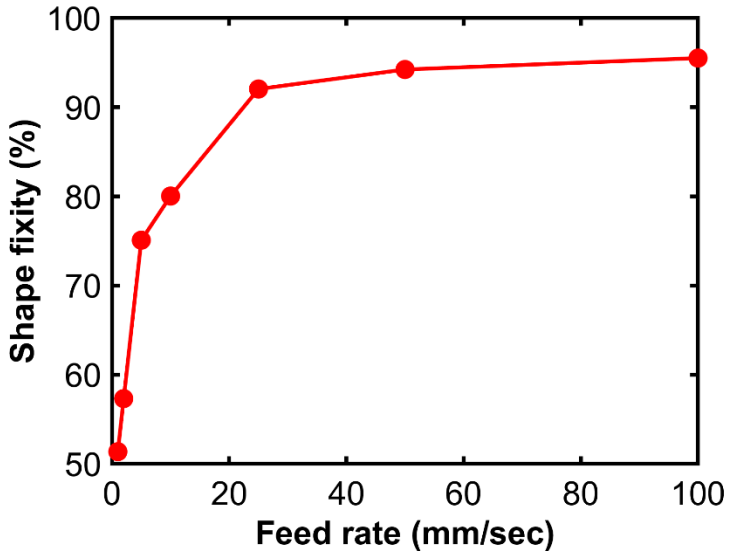

Figure 3.5: Shape fixity ratio of pre-strained polymer at different feed rates. The pre-strained polymer with higher shape fixity value, can better retain their applied strain and are efficient during shape recovery process.

The shape fixity ratio is smaller for lower feed rate and increases with increasing feed rate until 25 mm/sec after which the shape fixity ratio stays above fairly constant above 90%. A decrease in material feed rate increases the amount of time the polymer stays in contact with the roller and as a result, it gets enough time to relax and recover its applied strain after exiting the roller, whereas the converse is true for materials fed at a higher rate. However, feed rate above 50 mm/sec does not sufficiently increase shape fixity.

3.3.4. Effects of heating rate on shape recovery

In this section, we analyze the effect of heating rate on the shape recovery ratio of the pre-strained polymer. At the end of the pre-straining step, the polymer remains at 90°C ($T < T_g$). It is then taken through a shape recovery process by increasing its temperature to 110°C ($T > T_g$). The rate at which its temperature is increased has a significant effect on how fast the polymer undergoes

shape recovery, while the amount recovered essentially remains constant[21]. For this analysis, we pre-strain the polymer similar to the conditions mentioned in section 3.3.1. The temperature of the polymer, after exiting the roller, is increased at various rates of 1, 2, 5, 10, 20, and 40°C/min to 110°C. The shape recovery along y-axis and z-axis for multiple heating rates is shown in Figure 3.6a and Figure 3.6b respectively. The amount of pre-strain recovered in y-axis and z-axis is the same strain that was present at the end of the pre-straining sequence, as shown in Figure 3.3. The slower heating rate recovers almost all of the applied pre-strain in both directions; however, it takes longer to recover the applied pre-strain. In contrast, faster heating rate increases the temperature quickly, but cannot recover all of the strain even when the temperature reaches $T > T_g$. A pre-strained polymer heated above its T_g should recover its pre-strain regardless of heating rate.

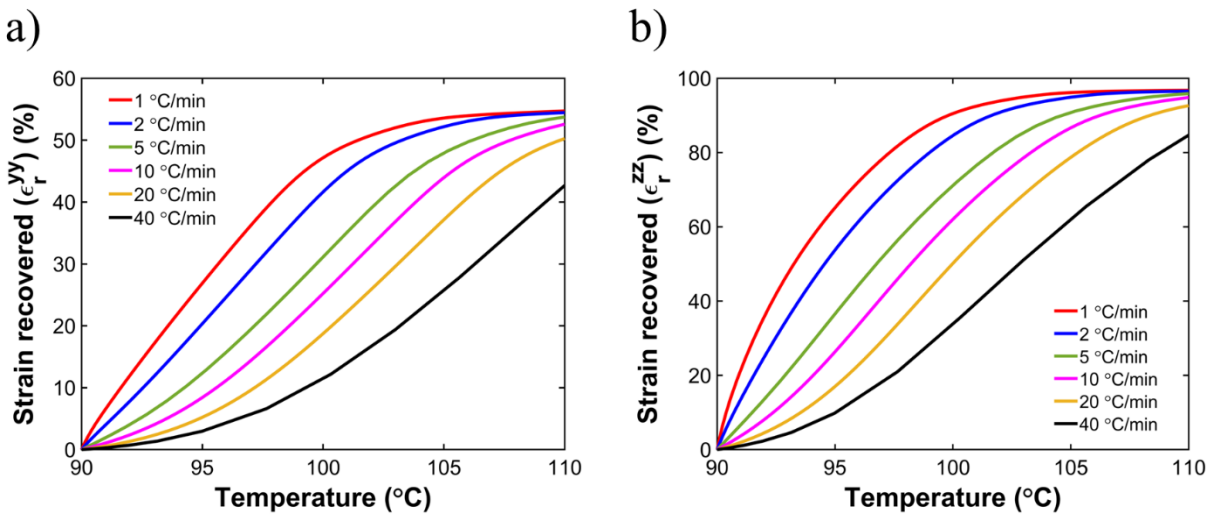

Figure 3.6: Shape recovery of applied pre-strain along a) y-axis and b) z-axis. The amount of strain recovered in each direction is the same that was present at the end of the pre-straining step.

3.4. Conclusion

In this chapter, we investigated the biaxial pre-straining through rolling process, using a previously developed coupled thermomechanical finite element framework. We applied the

framework to a commercially available polystyrene and conducted a biaxial thermomechanical rolling process to pre-strain it. This applies strain on two orthogonal directions and biaxially pre-strains the material. We observed the amount of change in strain in both directions and found out the decrease in thickness due to compressive force of the roller results in width and length elongation, the latter being insignificant compared to the former.

The combined effect of frictional force, width elongation and thickness reduction results in folding of the material on itself on the free edge and increases the effective contact surface area of the polymer. This distributes the contact force along the surface, effectively reducing the rolling stress throughout the rolling process. We observed an increase in shape fixity ratio with an increase in material feed rate, but no change was observed with roller speed. Finally, the pre-strained material is further subjected to uniform reheating to recover the applied strain in both directions and the recovery speed of the pre-strained polymer was evaluated for multiple heating rates.

This study in biaxial pre-straining process provides an insight into various processing parameters associated with the rolling process and the finite element framework makes it easier to modify these parameters and evaluate the pre-straining and recovery process for a wide variety of materials.

3.5. Future works

The future work consists of validating the model with an experimental setup. The preliminary design consists of a 24-in slip roll combined with a variable torque electric motor, purchased from Eastwood, as shown in Figure 3.7a and Figure 3.7b respectively. The manual crank of the slip roller will be replaced and will be attached with the chain sprocket system as shown in Figure 3.7c. The slip roller will have an adjustable height to vary the amount of thickness during

the rolling process. The slip roll will rest on T-slots and the motor (green solid, as shown in Figure 3.7c) is attached on a plate which is attached to the T-slots. The motor transfers its torque to the roller through a chain sprocket system which helps regulate the roller speed. The roller will be heated through a modified oven and the polymer, while exiting the roller, will be immediately cooled using a water bath. The pre-strained polymer will be reheated uniformly, and the shape recovery process will be analyzed for multiple polymers.

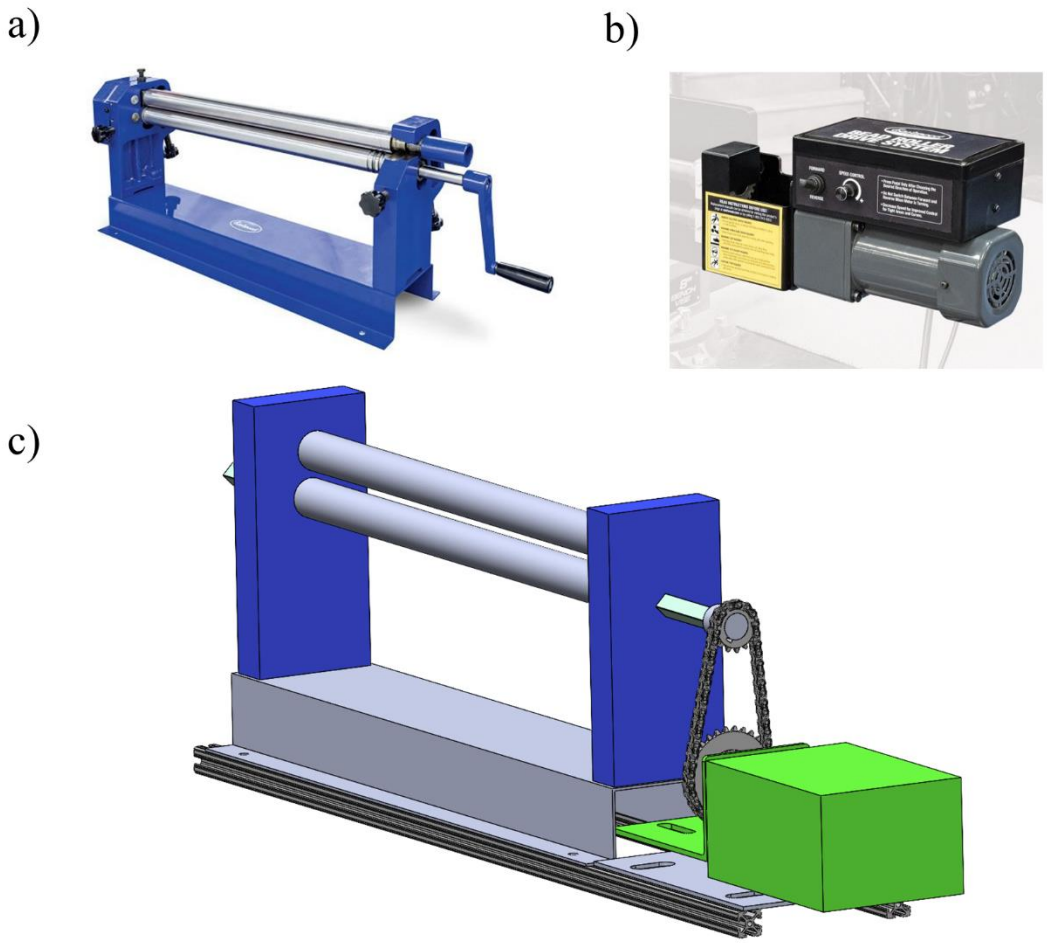

Figure 3.7: Experimental setup for biaxial pre-straining using a) slip roll[42] and b) a high torque DC motor[43] purchased from Eastwood. c) The motor and the roller shafts are connected with a chain sprocket system thus allowing the roller for variable roller speed.

3.6. References

(1) Akay, M. Influence of Total Processing History on Polypropylene Structure and Properties. *British Polymer Journal* **1989**, *21* (4), 285–293. https://doi.org/10.1002/pi.4980210402.

(2) Drobny, J. G. Processing Methods Applicable to Thermoplastic Elastomers. In *Handbook of Thermoplastic Elastomers (Second Edition)*; Drobny, J. G., Ed.; Plastics Design Library; William Andrew Publishing: Oxford, 2014; pp 33–173. https://doi.org/10.1016/B978-0-323-22136-8.00004-1.

(3) Siwakoti, M.; Mailen, R. W. Relationship between Recovered Enthalpy and the Shape-Memory Effect in Shape Memory Polymers. *Journal of Applied Polymer Science n/a* (n/a), e54727. https://doi.org/10.1002/app.54727.

(4) Papkov, D.; Delpouve, N.; Delbreilh, L.; Araujo, S.; Stockdale, T.; Mamedov, S.; Maleckis, K.; Zou, Y.; Andalib, M. N.; Dargent, E.; Dravid, V. P.; Holt, M. V.; Pellerin, C.; Dzenis, Y. A. Quantifying Polymer Chain Orientation in Strong and Tough Nanofibers with Low Crystallinity: Toward Next Generation Nanostructured Superfibers. *ACS Nano* **2019**, *13* (5), 4893–4927. https://doi.org/10.1021/acsnano.8b08725.

(5) Chen, W.; Kong, X.; Wei, Q.; Chen, H.; Liu, J.; Jiang, D. Compression and Stretching of Confined Linear and Ring Polymers by Applying Force. *Polymers (Basel)* **2021**, *13* (23), 4193. https://doi.org/10.3390/polym13234193.

(6) Tadmor, Z.; Gogos, C. G. *Principles of Polymer Processing*, 2nd ed.; Wiley-Interscience: Hoboken, N.J, 2006.

(7) Kushida, T.; Nagase, T.; Naito, H. Mobility Enhancement in Solution-Processable Organic Transistors through Polymer Chain Alignment by Roll-Transfer Printing. *Organic Electronics* **2011**, *12* (12), 2140–2143. https://doi.org/10.1016/j.orgel.2011.09.013.

(8) Kumar, M.; Sharma, A.; Hait, S.; Wießner, S.; Heinrich, G.; Arief, I.; Naskar, K.; Stöckelhuber, K. W.; Das, A. Effect of Prestrain on the Actuation Characteristics of Dielectric Elastomers. *Polymers (Basel)* **2020**, *12* (11), 2694. https://doi.org/10.3390/polym12112694.

(9) Wu, F.; Misra, M.; Mohanty, A. K. Challenges and New Opportunities on Barrier Performance of Biodegradable Polymers for Sustainable Packaging. *Progress in Polymer Science* **2021**, *117*, 101395. https://doi.org/10.1016/j.progpolymsci.2021.101395.

(10) Delorme, A. E.; Radusin, T.; Myllytie, P.; Verney, V.; Askanian, H. Enhancement of Gas Barrier Properties and Durability of Poly(Butylene Succinate-Co-Butylene Adipate)-Based Nanocomposites for Food Packaging Applications. *Nanomaterials (Basel)* **2022**, *12* (6), 978. https://doi.org/10.3390/nano12060978.

(11) Qin, R.; Peng, L.; Deng, H.; Liu, Y.; Liu, X. Enhancing Thermal Dimensional Stability of Polyimide Composite Films through In-Situ Constructing Highly Interfacial Grafting Degree to Constrain Early Chain Relaxation. *Composites Part B: Engineering* **2021**, *216*, 108829. https://doi.org/10.1016/j.compositesb.2021.108829.

(12) Zhang, W.; Zhou, J.; Cao, Z.; Wu, X.; Wang, H.; Han, S.; Zhang, Y.; Sun, F.; Zhang, T. In Situ Construction of Thermotropic Shape Memory Polymer in Wood for Enhancing Its Dimensional Stability. *Polymers (Basel)* **2022**, *14* (4), 738. https://doi.org/10.3390/polym14040738.

(13) Wang, Z.; Sun, L.; Ni, Y.; Liu, L.; Xu, W. Flexible Electronics and Healthcare Applications. *Frontiers in Nanotechnology* **2021**, *3*.

(14) Mostafa, N. H.; Ismarrubie, Z.; Sapuan, S.; Sultan, M. Effect of Equi-Biaxially Fabric Prestressing on the Tensile Performance of Woven E-Glass/Polyester Reinforced Composites. *Journal of Reinforced Plastics and Composites* **2016**, *35* (14), 1093–1103. https://doi.org/10.1177/0731684416638553.

(15) Cui, M.; Kayani, S. H.; Kim, H.-W.; Lee, J.-H. The Role of Prestraining on Mechanical Properties and Microstructure of Preaged AA 6016 Al-Mg-Si Sheets. *Journal of Alloys and Compounds* **2023**, *960*, 170681. https://doi.org/10.1016/j.jallcom.2023.170681.

(16) Bettini, P.; Rigamonti, D.; Sala, G. SMA for Composite Aerospace Structures. In *Shape Memory Alloy Engineering (Second Edition)*; Concilio, A., Antonucci, V., Auricchio, F., Lecce, L., Sacco, E., Eds.; Butterworth-Heinemann: Boston, 2021; pp 561–590. https://doi.org/10.1016/B978-0-12-819264-1.00016-9.

(17) Brinson, H. F.; Brinson, L. C. *Polymer Engineering Science and Viscoelasticity: An Introduction, Second Edition*; Springer US, 2015. https://doi.org/10.1007/978-1-4899-7485-3.

(18) Rubinstein, M.; Colby, R. H. *Polymer Physics*; Oxford University Press: Oxford ; New York, 2003.

(19) Gennes, P. G. de. *Scaling Concepts in Polymer Physics*; Cornell University Press: Ithaca, N.Y, 1979.

(20) Higashida, Y.; Watanabe, K.; Kikuma, T. Mechanical Properties of Uniaxially and Biaxially Rolled Polymer Sheets. *ISIJ International* **1991**, *31* (6), 655–660. https://doi.org/10.2355/isijinternational.31.655.

(21) Mailen, R. W.; Liu, Y.; Dickey, M. D.; Zikry, M.; Genzer, J. Modelling of Shape Memory Polymer Sheets That Self-Fold in Response to Localized Heating. *Soft Matter* **2015**, *11* (39), 7827–7834. https://doi.org/10.1039/C5SM01681A.

(22) Wang, Z.; Liu, J.; Guo, J.; Sun, X.; Xu, L. The Study of Thermal, Mechanical and Shape Memory Properties of Chopped Carbon Fiber-Reinforced TPI Shape Memory Polymer Composites. *Polymers* **2017**, *9* (11), 594. https://doi.org/10.3390/POLYM9110594.

(23) *Mechanical Behaviour and Induced Microstructural Development upon Simultaneous and Balanced Biaxial Stretching of Poly(ethylene furandicarboxylate), PEF - PMC*. https://www.ncbi.nlm.nih.gov/pmc/articles/PMC9919262/ (accessed 2023-10-03).

(24) Joshi, A. S.; Lawrence, J. G.; Coleman, M. R. Effect of Biaxial Orientation on Microstructure and Properties of Renewable Copolyesters of Poly(Ethylene Terephthalate) with 2,5-Furandicarboxylic Acid for Packaging Application. *ACS Appl. Polym. Mater.* **2019**, *1* (7), 1798–1810. https://doi.org/10.1021/acsapm.9b00330.

(25) Abdulhafez, M.; Line, J.; Bedewy, M. Sequential Self-Folding of Shape Memory Polymer Sheets by Laser Rastering Toward Origami-Based Manufacturing. *Journal of Manufacturing Science and Engineering* **2021**, *143* (091008). https://doi.org/10.1115/1.4050463.

(26) Tolley, M. T.; Felton, S. M.; Miyashita, S.; Aukes, D.; Rus, D.; Wood, R. J. Self-Folding Origami: Shape Memory Composites Activated by Uniform Heating. *Smart Materials and Structures* **2014**, *23* (9), 094006. https://doi.org/10.1088/0964-1726/23/9/094006.

(27) Zhao, Y.; Hua, M.; Yan, Y.; Wu, S.; Alsaid, Y.; He, X. Stimuli-Responsive Polymers for Soft Robotics. *Annu. Rev. Control Robot. Auton. Syst.* **2022**, *5* (1), 515–545. https://doi.org/10.1146/annurev-control-042920-014327.

(28) Choi, J. G.; Spinks, G. M.; Kim, S. J. Mode Shifting Shape Memory Polymer and Hydrogel Composite Fiber Actuators for Soft Robots. *Sensors and Actuators A: Physical* **2022**, *342*, 113619. https://doi.org/10.1016/j.sna.2022.113619.

(29) Dao, T. D.; Ha, N. S.; Goo, N. S.; Yu, W.-R. Design, Fabrication, and Bending Test of Shape Memory Polymer Composite Hinges for Space Deployable Structures. *Journal of Intelligent Material Systems and Structures* **2018**, *29* (8), 1560–1574. https://doi.org/10.1177/1045389X17742728.

(30) Liu, Y.; Du, H.; Liu, L.; Leng, J. Shape Memory Polymers and Their Composites in Aerospace Applications: A Review. *Smart Materials and Structures* **2014**, *23* (2). https://doi.org/10.1088/0964-1726/23/2/023001.

(31) Qaiss, A.; Bousmina, M. Biaxial Stretching of Polymers Using a Novel and Versatile Stretching System. *Polymer Engineering & Science* **2011**, *51* (7), 1347–1353. https://doi.org/10.1002/pen.21869.

(32) Bazhenov, S. L.; Efimov, A. V.; Sosnovskii, I. V.; Bol'shakova, A. V.; Kechek'yan, A. S.; Volynskii, A. L. Plastic Deformation of Polyethylene Terephthalate Films during Rolling. *Polym. Sci. Ser. A* **2015**, *57* (4), 425–429. https://doi.org/10.1134/S0965545X1504001X.

(33) Hubbard, A. M.; Davis, D. S.; Dickey, M. D.; Genzer, J. Shape Memory Polymers for Self-Folding via Compression of Thermoplastic Sheets. *Journal of Applied Polymer Science* **2018**, *135* (47), 46889. https://doi.org/10.1002/app.46889.

(34) Farotti, E.; Mancini, E.; Lattanzi, A.; Utzeri, M.; Sasso, M. Effect of Temperature and Strain Rate on the Formation of Shear Bands in Polymers under Quasi-Static and Dynamic Compressive Loadings: Proposed Constitutive Model and Numerical Validation. *Polymer* **2022**, *245*, 124690. https://doi.org/10.1016/j.polymer.2022.124690.

(35) Tolcha, M. A.; Altenbach, H. Numerical Modeling Rolling Contact Problem and Elasticity Deformation of Rolling Die under Hot Milling. *Metals 2019, Vol. 9, Page 226* **2019**, *9* (2), 226. https://doi.org/10.3390/MET9020226.

(36) *Fundamentals of Rolling*; Elsevier, 1969. https://doi.org/10.1016/C2013-0-02066-X.

(37) Mailen, R. W.; Dickey, M. D.; Genzer, J.; Zikry, M. A. A Fully Coupled Thermo-Viscoelastic Finite Element Model for Self-Folding Shape Memory Polymer Sheets. *Journal of Polymer Science Part B: Polymer Physics* **2017**, *55* (16), 1207–1219. https://doi.org/10.1002/polb.24372.

(38) Simulia, 3DS. *Abaqus Analysis User's Guide*.

(39) Williams, M. L.; Landel, R. F.; Ferry, J. D. *The Temperature Dependence of Relaxation Mechanisms in Amorphous Polymers and Other Glass-Forming Liquids*; 1955.

(40) Tobushi, H.; Matsui, R.; Hayashi, S.; Shimada, D. The Influence of Shape-Holding Conditions on Shape Recovery of Polyurethane-Shape Memory Polymer Foams. *Smart Materials and Structures* **2004**, *13* (4), 881. https://doi.org/10.1088/0964-1726/13/4/026.

(41) Yan, Y.; Mao, Y.; Li, B.; Zhou, P. Machinability of the Thermoplastic Polymers: PEEK, PI, and PMMA. *Polymers (Basel)* **2020**, *13* (1), 69. https://doi.org/10.3390/polym13010069.

(42) *Eastwood 24 inch Metal Forming and Fabrication Slip Roll*. https://www.eastwood.com/eastwood-24-in-slip-roll.html (accessed 2023-10-01).

(43) *Bead Roller Drive System*. https://www.eastwood.com/eastwood-bead-roller-drive-system.html (accessed 2023-10-01).

Chapter 4

Coupled electro-thermo-mechanical modeling of shape memory polymers

(Siwakoti, M., and Mailen, R.W., "Coupled Electro-Thermo-Mechanical Modeling of Shape Memory Polymers", *Proceedings of Smart Materials, Adaptive Structures and Intelligent Systems (SMASIS)*, 2019, DOI: https://doi.org/10.1115/SMASIS2019-5693)

Abstract

Shape memory polymers (SMPs) are extensively studied for self-folding origami due to their large strain recovery, low cost, and low activation energy. SMPs utilize viscoelastic material behavior to change shape in response to an applied stimulus, for instance light or electricity. Electrical actuation is desirable due to its higher energy density and shorter response time. Previous studies reported empirical results on shape recovery of conductive polymer composites actuated by specific applied voltage or current conditions, which required rigorous experimentation. Here, we introduce a finite element framework capable of predicting the coupled electro-thermo-mechanical response of electrically actuated SMPs. As inputs, this framework requires material properties, such as electrical conductivity and viscoelastic parameters. The viscoelastic response is implemented using a Prony series model that is fit to experimental dynamic mechanical analysis (DMA) data. Using this framework, we predict the shape recovery behavior of electrically actuated SMPs subject to various thermal, electrical, and mechanical loads and evaluate the sensitivity of the response to the material properties. Additionally, we show the effects of material pre-straining conditions and localized conductive pathways on shape recovery and self-folding. This computational framework provides a fundamental understanding of the electro-thermo-mechanical response of electrically actuated SMPs and can be used to design electrically actuated self-folding origami for aerospace applications.

4.1. Introduction

Shape memory polymers (SMPs) are an emerging class of materials with applications in adaptive sensors[1], self-deploying structures[2], heat-shrinking tubes[3], and medical implants for treatment of aneurisms[4]. SMPs possess the ability to change shape in response to external stimuli, such as heat[5–7], light[8–10], and electricity[11–13]. One important application of SMPs is as an actuator for self-folding, wherein the material deforms out-of-plane in response to the provided stimuli. Self-folding in response to external stimuli can result from material property gradients[14,15], material stacking[16,17], and localized activation[9,18,19]. Localized activation provides a route for obtaining complex 3D structures[3,20] and allows the use of sequential folding[8,21,22]. The self-folding response depends on the viscoelastic property of the material[23,24]. Furthermore, the material must be pre-strained, i.e., deformed to a temporary state, in order to obtain the folding response[25,26]. Being able to control the self-folding response of the material to a variety of stimuli is paramount to adapting SMPs to practical applications.

We seek to develop a fundamental understanding of the response of locally activated SMP sheets subjected various external stimuli. Localized activation of the shape memory effect provides an efficient technique for initiation of self-folding and is advantageous due to its compatibility with various actuation stimuli like light[9,10], humidity[27], and electricity[19,28]. For example, ink patterned as a hinge on the surface of the SMP has been demonstrated to absorb energy locally when exposed to an infrared (IR) light, which induces folding[29,30]. When the patterned sample is uniformly exposed to an IR light, the upper surface of the hinge heats up and a temperature gradient develops along the thickness of the sheet. The temperature gradient in turn produces a shrinkage gradient along the thickness of the sheet, which causes the sheet to fold. Previous studies on various actuation methods, e.g., light, heat, and humidity, concluded that the size of the hinge[18,30], and the

support temperature[29] play important roles in determining the folding behavior. Further, a computational model that predicts the self-folding response to local light absorption has been validated against experimental results[9,18].

Recent studies have focused on electrical actuation of the shape memory effect, also known as Joule-heating. The Joule-heating approach converts electric current to thermal energy efficiently in electrically conductive materials[31]. Typically, SMPs are electrically insulating, but can be made conducting by the incorporation of conducting fillers like carbon black[12,32,33], carbon nanotubes[32,34], Nickel[33,35], and short carbon fibers[11,36]. Although electrically activated self-folding has been demonstrated experimentally[28,36], a finite element (FE) framework capable of predicting the material response is missing. To address this need, we develop a nonlinear, 3D FE framework, which couples the electrical, thermal, and mechanical solutions to study the uniform shrinking (in-plane) and folding (out-of-plane) response of Joule heated SMP sheets. The framework introduced here is based on a previous framework for light stimulated SMP sheets, developed by the authors[18]. In the framework, we account for the temperature dependency of the material properties, viscoelasticity, thermal expansion, and electrical conductivity of an SMP embedded with locally patterned conducting fillers.

This chapter is arranged as follows. First, we introduce the FE framework, which combines the viscoelastic, mechanical, and electrical properties of the material in conjunction with the input boundary conditions. Then we apply the framework to a model which accounts for the material pre-straining sequence. Using this model, we study the uniform shrinking of conductive SMP sheets, which heat uniformly when subjected to electric boundary conditions. Finally, we investigate parametrically the effects of applied voltage, electrical conductivity, and hinge width on the self-folding behavior of the SMP.

4.2. Computational approach

We developed a nonlinear, 3D FE framework to study the self-folding response of electrically activated SMP sheets. The framework couples thermal, mechanical, and electrical solutions. An experimentally obtained viscoelastic master curve is modeled by a Prony series[18], which requires dimensionless relaxation moduli, g_i, and relaxation times, τ_i, to calculate the storage modulus, G', and loss modulus, G''[37], according to the relations:

$$G'(\omega) = G_0\left(1 - \sum_{i=1}^{n} g_i\right) + G_0 \sum_{i=1}^{n} \frac{g_i (2\pi\omega\tau_i)^2}{1 + (2\pi\omega\tau_i)^2} \quad (1)$$

$$G''(\omega) = G_0 \sum_{i=1}^{n} \frac{g_i (2\pi\omega\tau_i)}{1 + (2\pi\omega\tau_i)^2} \quad (2)$$

$$tan\,\delta = \frac{G''(\omega)}{G'(\omega)} \quad (3)$$

where G_0 is the instantaneous shear modulus, ω is the frequency in Hz and δ is the phase angle, which indicates the amount of energy dissipated.

The relaxation times are temperature dependent and is updated for the viscoelastic material model as the temperature changes using the WLF equation[38] as:

$$log(a_T) = -\frac{C_1 (T - T_g)}{C_2 + (T - T_g)} \quad (4)$$

where, a_T is the shift factor for the time and temperature dependent properties, C_1 and C_2 are constants, T is the temperature and T_g is the glass transition temperature. For polystyrene, the values of C_1 = 17.44; C_2 = 51.6 and T_g = 103°C was used[39]. The WLF equation was used to update the relaxation times, τ_i, for the viscoelastic material model as the temperatures change.

The thermal solution in the framework accounts for electrically induced Joule heating. The Joule-heating heat flux, $\dot{q}_J$, which results from electrical resistive heating, was calculated as[37]:

$$\dot{q}_J = \boldsymbol{J} \cdot \boldsymbol{E} = \nabla\varphi \cdot \boldsymbol{\sigma}^E \cdot \nabla\varphi \tag{5}$$

where, $\boldsymbol{J} = -\boldsymbol{\sigma}^{\boldsymbol{E}} \cdot \nabla\varphi$ is the electric current density (current per unit area) entering the control volume, $\boldsymbol{\sigma}^E$ is the electrical conductivity matrix, φ is the electrical potential and $\boldsymbol{E} = -\nabla\varphi$ is the electric field intensity. Equation (5) represents a heat source term produced from the Joule heating and contributes additively to the heat equation as

$$\dot{q}_t = \dot{q}_J + \dot{q}_e \tag{6}$$

$$\rho C_p \frac{\partial T}{\partial t} - \nabla \cdot (k\nabla T) = \dot{q}_t \tag{7}$$

where, $\dot{q}_t$ and $\dot{q}_e$ represent the total heat flux and heat flux from external sources, e.g., convection, respectively. The variables ρ, C_p and k are the density, specific heat and thermal conductivity of the material respectively.

4.3. Results and Discussion

4.3.1. Pre-straining sequence

We applied the FE framework to model the coupled electro-thermo-mechanical response with hybrid, 3D, eight-node, trilinear brick elements. We used previously published material data for a commercially available polystyrene based SMP sheet known as Grafix® shrink film in our framework[18]. We used the FE framework to study two cases: (1) uniform shrinking recovery and (2) localized folding recovery. Both models are subjected to a pre-strain sequence before applying boundary conditions for material recovery. For the uniform shrinking case, the material shrank from the pre-strained state when Joule heated above T_g. For the folding case, a localized current is applied along the hinge, that heat the material, causing it to shrink locally and fold along the hinge.

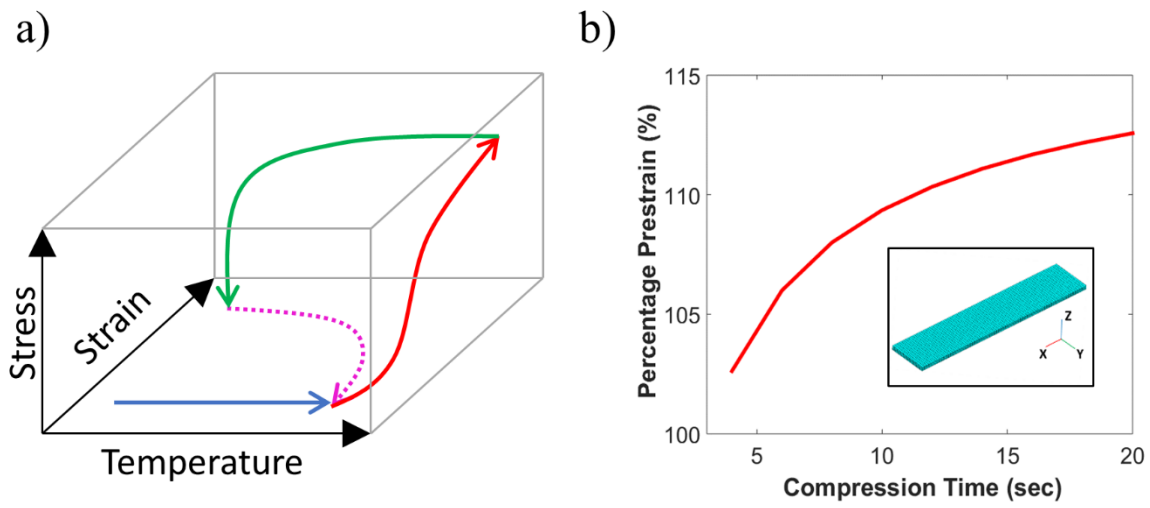

Figure 4.1: Pre-straining sequence. (a) Step-by-step application of thermomechanical boundary conditions. Blue: Elevated temperature, Red: Compression, Green: Cooling, Broken magenta: Recovery. (b) Pre-strain percent imparted on the sample for various compression times.

We subjected the material to a thermal and mechanical loading sequence to impart pre-strain to the material before the recovery process. This loading sequence and boundary conditions are illustrated in Figure 4.1a. We heat the material at an initial temperature of 108°C specified uniformly throughout the model. The model was then compressed along the thickness of the sheet with a compressive displacement boundary condition. This compression imparts strains in both directions in the transverse plane. The initial temperature and the displacement used were similar to those used in previous experimental studies of the Grafix® SMPs[18], and are representative of the actual SMP pre-straining conditions. Following the compression, we linearly decrease the surface temperature on the top and bottom surfaces of the SMP from 108°C to 25°C using a specified temperature boundary condition, which reduces the temperature throughout the model. As a final step, we remove the compressive displacement.

We performed an initial investigation of the effects of compression time on the pre-strain imparted to the sample shown in the inset of Figure 4.1b. The pre-strain is measured after removal of the compressive displacement boundary condition at the end of the pre-strain sequence and the results are shown in Figure 4.1b. These results indicate that increasing the compression time increases the amount of pre-strain imparted to the material. For the remainder of this chapter, we will use a compression time of 12 seconds, which corresponds to a pre-strain of 110%. Following the pre-straining sequence, we applied the recovery boundary conditions depending on the desired type of recovery (shrinking or folding).

4.3.2. Uniform shrinking

Following the pre-strain sequence, we study the uniform shrinking recovery of electrically activated SMP sheets. The geometry is shown in Figure 4.2a, and applied boundary conditions for the pre-straining sequence are shown in Figure 4.2b. Joule heating was achieved by applying an electric voltage on two ends of the sample in its pre-strained state as shown in Figure 4.2c. The percent shrinkage of the material as a function of time was calculated as[18]:

$$S(t) = \left(1 - \frac{l(t)}{l_p}\right) \times 100\% \tag{8}$$

where l_p is the pre-strained length and $l(t)$ is the instantaneous length of the sample during uniform shrinking.

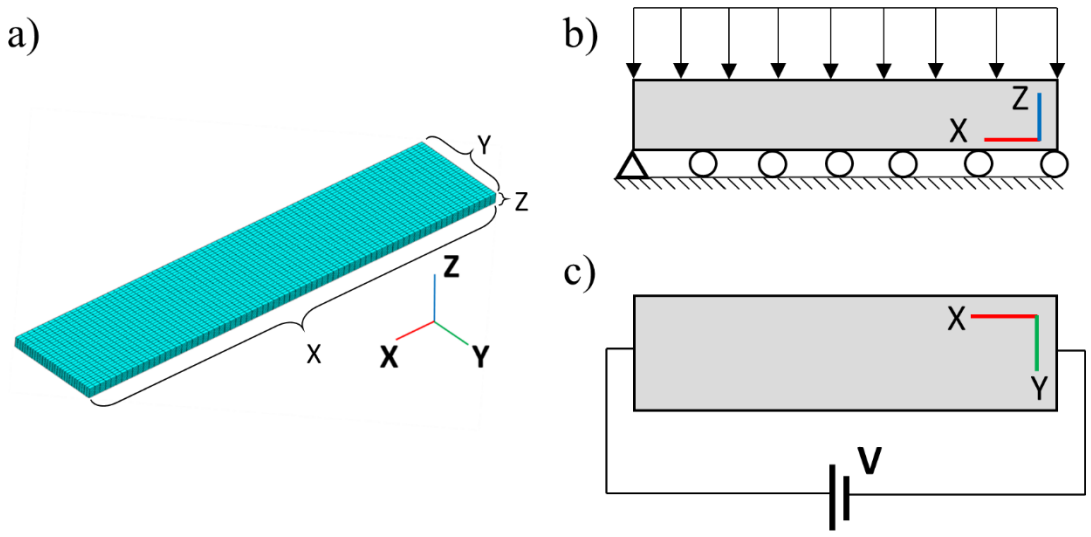

Figure 4.2: Uniform Shrinking Model. (a) Shrinking model depicting mesh. Labels specify the dimensions of the sample before pre-strain. X = 50 mm (75 elements), Y = 10 mm (30 elements) and Z = 1 mm (10 elements). (b) Mechanical boundary condition during pre-straining sequence. (c) Electrical boundary condition during recovery sequence.

Figure 4.3a shows the temperature histories of the samples subjected to 10, 50, 75, 85, 95 and 100 volts of potential difference. The voltages were applied after the sample was pre-strained and were applied separately for each sample. The temperature histories displayed represent the average nodal temperature throughout the sample. As expected, the heating rate depends on the applied voltage for a fixed electrical conductivity value, with higher voltages producing faster heating. The results show an initial linear increase in temperature which results from the conversion of electrical energy to thermal energy. The material shrinkage histories are shown in Figure 4.3b. The sample expands initially due to thermal expansion but begins to shrink due to the greater effect of viscoelastic recovery as the temperature approaches and exceeds T_g. The maximum shrinkage is 52% using the previously described pre-straining sequence. This maximum shrinkage is similar to commercially available SMP sheets[18]. The material does not begin to shrink

instantaneously after applying the voltage. Rather, the time to begin shrinking depended on the applied voltage. Noticeable shrinking occurred when the material exceeded a threshold temperature of 108°C. This temperature is reasonable as it is above T_g (=103°C) of the sample. These results verify our pre-straining approach and the use of Joule-heating to induce shape recovery. Furthermore, the results indicate that increasing the applied voltage results in faster shrinkage only after a threshold temperature is exceeded.

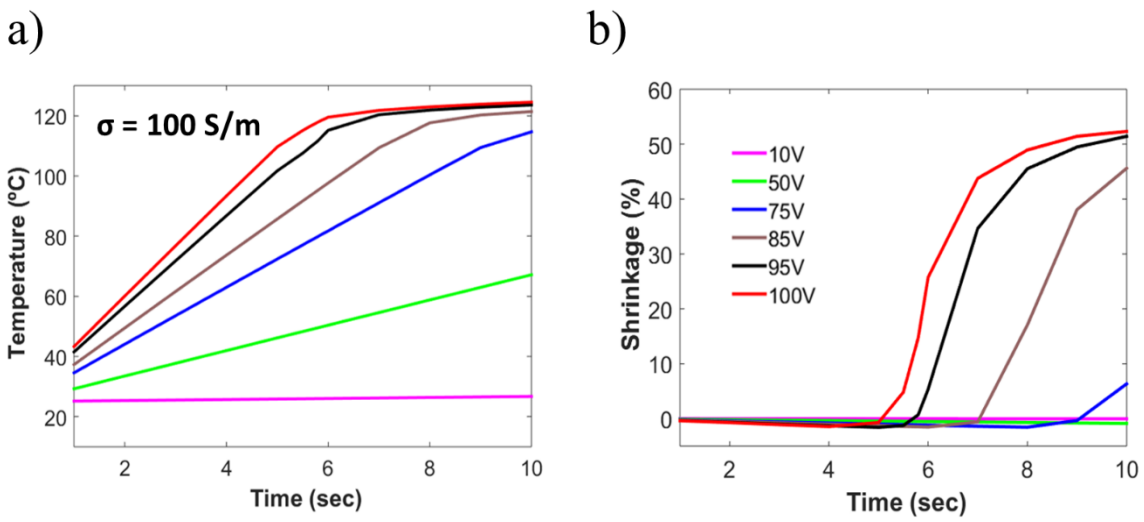

Figure 4.3: Computed results for different voltages applied in the recovery sequence of uniformly shrinking model. (a) Average nodal temperature of the sample. (b) Corresponding amount of shrinkage.

4.3.3. Localized folding

We modeled the localized folding recovery by introducing a conductive pathway (hinge) along the width of the sample Figure 4.4a. The hinge region is representative of locally patterned conductive filler in the SMP matrix. As a result, the hinge has an electrical conductivity value higher than its surrounding material. We imposed mechanical boundary conditions to avoid rigid body motion during pre-straining sequence Figure 4.4b. After the pre-strain sequence, we applied

an electrical boundary condition along the length of the hinge, as shown in Figure 4.4c. Application of this voltage causes the conductive region of the material to heat locally, which produces a localized temperature increase in the vicinity of the hinge. This increase in temperature is sufficient to initiate localized shrinking of the sample. Due to the gradient in temperature and shrinkage, the material folds similar to experimental results for self-folding SMP sheets activated by local light absorption[9,18].

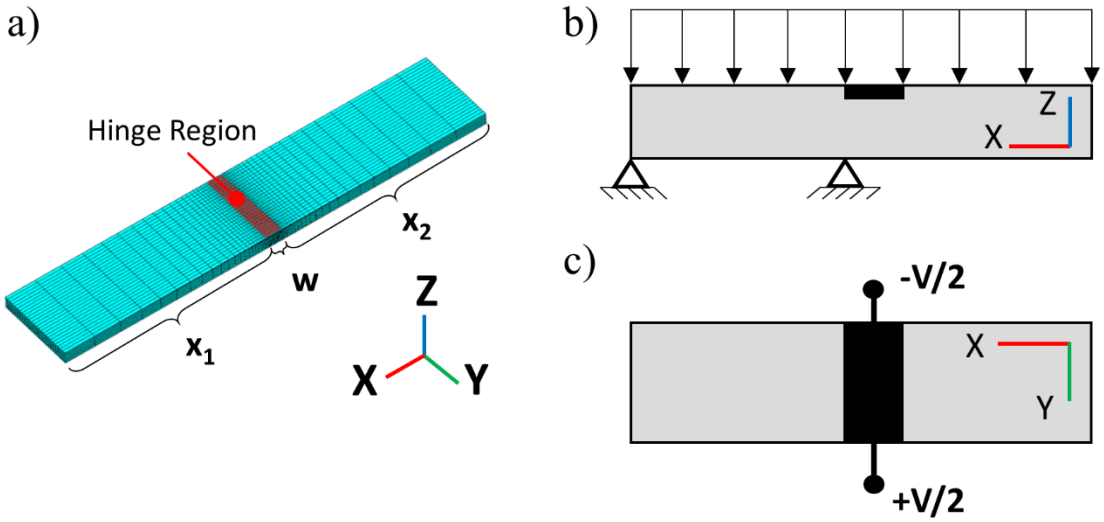

Figure 4.4: Localized Folding Model. (a) Geometry of the folding model. The overall dimensions are the same as in uniform shrinking geometry. Labels specify the length of the regions. $X_1 = X_2 = 25$ elements and hinge width (w) = 20 elements. (b) Mechanical boundary condition during pre-straining sequence. (c) Electrical boundary condition during recovery sequence.

Figure 4.5a shows the average hinge temperature and corresponding bending angle for 1, 1.5, 2, 2.5 mm hinge widths at a total potential difference of 20V and an electrical conductivity of 1000 S/m. The specified hinge widths were obtained before pre-straining the sample. The temperature displayed represents the average nodal temperature of the top surface of the hinge. We

note that the average hinge temperature is the same for all hinge widths. The results for bending angle, α_b, which is the angle subtended by the sheet as it folds, are shown in Figure 4.5b. For clarity, the image inset in Figure 4.5b depicts the definition of α_b. In general, the results indicate an increase in maximum bending angle for increasing hinge widths. This is because the applied voltage works over a wider cross-section area for wider hinges, thus activating more material. Furthermore, the results show that there is a certain time lag between the application of the voltage and initiation of the folding for all hinges. The time lag suggests the gradual development of temperature and shrinkage gradients through the thickness of the sheet, which was reported in previous studies[9,18].

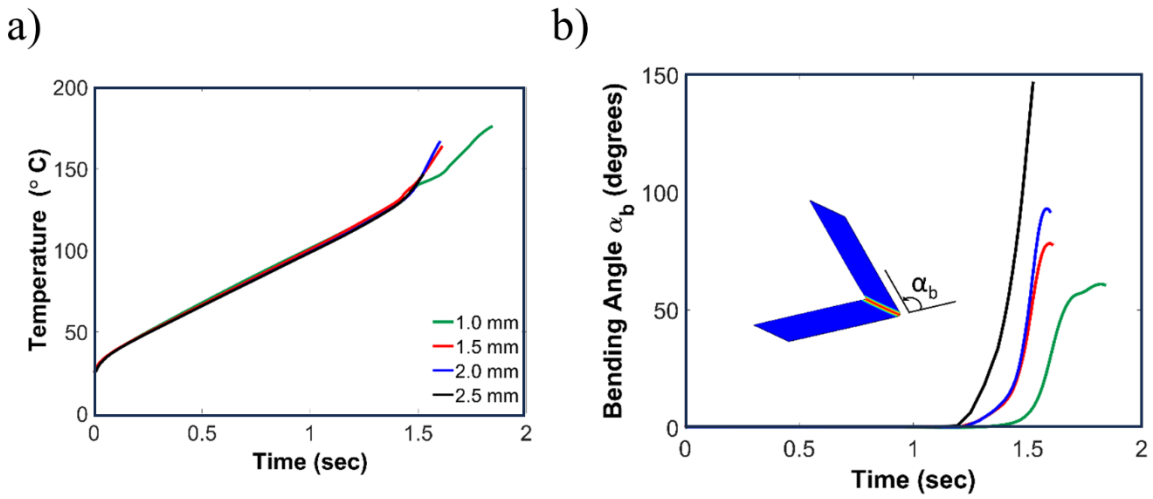

Figure 4.5: Computed results for localized folding at 20V potential difference for various hinge widths. (a) Average nodal temperature on the upper surface of the hinge. Note, the temperature profile is almost the same for various hinges. (b) Corresponding bending angles (α_b) during local folding.

Next, we investigate the effects of electrical conductivity on hinge temperature and bending angle. Figure 4.6a demonstrates the effects of varying electrical conductivity on the hinge

temperature of the sample with an applied potential difference of 15V and a 1.5 mm hinge width. Increasing electrical conductivity results in faster heating in the hinge region. The results for bending angle, shown in Figure 4.6b, indicate that increasing the conductivity produces a larger maximum bending angle. The simulations were terminated if the bending angle exceeded 180° due to contact of the folding faces. Moreover, the rate of folding increases while the time lag between the application of voltage and initiation of folding decreases for increasing conductivity. This is expected as the increased electrical conductivity facilitates the conversion of electrical energy to thermal energy much faster.

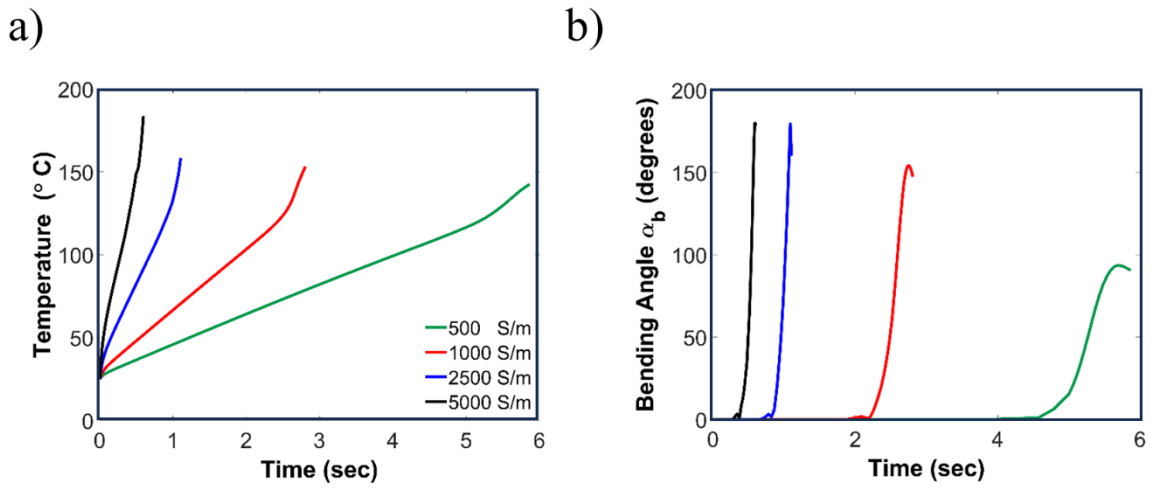

Figure 4.6: Predicted folding results at 15V potential difference, 1.5 mm wide hinge for various electrical conductivity of the sample. (a) The temperature variation at different conductivity. (b) Corresponding bending angles (α_b)

Finally, we investigate the effects of applied voltage on folding by considering applied potential differences of 15, 20, 25V on a sample with a 1.5 mm hinge width and 1000 S/m conductivity. Figure 4.7a shows the temperature histories for varying applied voltages, and Figure 4.7b shows the corresponding bending angle. It is seen that while the folding rate remains fairly similar at all voltages, the time lag is reduced for increased applied voltages. The thermal

conductivity of the material controls the temperature gradient through the thickness of the sheet, which influences the folding rate. Changes in thermal conductivity were not considered in the present study.

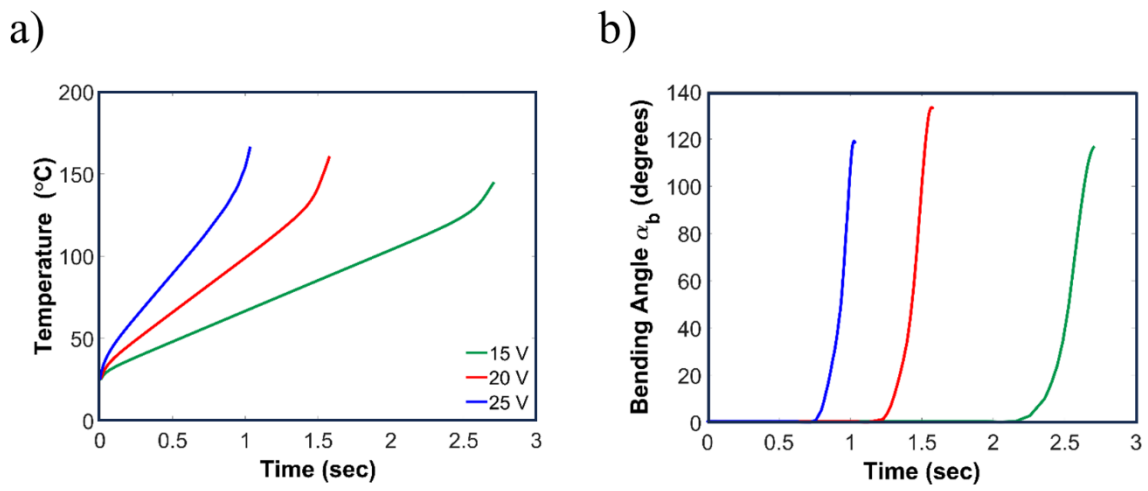

Figure 4.7: Predicted folding results at electrical conductivity of 1000 S/m, 1.5 mm wide hinge for various potential difference applied to the sample. (a) The temperature variation resulting from different applied voltages. (b) Corresponding bending angles (α_b)

4.4. Conclusion

We developed a three-dimensional finite element framework capable of predicting the electro-thermo-mechanical response of SMPs containing a conductive filler. The viscoelastic material properties were based on previously published rheological data but can be applied to other thermally activated systems. We applied the model to commercially available SMPs, embedded with conductive fillers, and subjected the model to various electro-thermo-mechanical boundary conditions. We used the model to investigate the shrinking behavior to different potential differences and the self-folding behavior of the SMP to varying voltages, conductivity, and hinge width.

In the uniform shrinking model, we observed an increase in heating rate at higher applied voltages, which allowed the sample to heat and shrink faster. The polymer must be heated above a critical temperature for shrinking to occur, which for this system was 108°C. In the folding model we observed an increase in maximum bending angle and rate of folding for wider hinge widths and higher electrical conductivity values. Also, the onset of folding time was reduced at higher applied voltages, wider hinge widths, and for highly conducting sample. For folding to occur a critical surface temperature must be exceeded, similar to the shrinking behavior. Our computational approach provides a fundamental understanding of the Joule-heated self-folding of an SMP. The finite element framework makes it easier to modify material property data to evaluate the effects on self-folding. Furthermore, the model provides an insight to shape recovery and self-folding behavior, which is vital in predicting complex origami geometries.

4.5. References

(1) Zhao, W.; Liu, L.; Lan, X.; Su, B.; Leng, J.; Liu, Y. Adaptive Repair Device Concept with Shape Memory Polymer. *Smart Materials and Structures* **2017**, *26* (2), 025027. https://doi.org/10.1088/1361-665X/aa5595.

(2) Hu, J.; Chen, S. A Review of Actively Moving Polymers in Textile Applications. *Journal of Materials Chemistry* **2010**, *20* (17), 3346–3355. https://doi.org/10.1039/b922872a.

(3) Tolley, M. T.; Felton, S. M.; Miyashita, S.; Aukes, D.; Rus, D.; Wood, R. J. Self-Folding Origami: Shape Memory Composites Activated by Uniform Heating. *Smart Materials and Structures* **2014**, *23* (9), 094006. https://doi.org/10.1088/0964-1726/23/9/094006.

(4) Small, W.; Buckley, P. R.; Wilson, T. S.; Benett, W. J.; Hartman, J.; Saloner, D.; Maitland, D. J. Shape Memory Polymer Stent With Expandable Foam: A New Concept for Endovascular

Embolization of Fusiform Aneurysms. *IEEE Transactions on Biomedical Engineering* **2007**, *54* (6), 1157–1160. https://doi.org/10.1109/TBME.2006.889771.

(5) Srivastava, V.; Chester, S. A.; Anand, L. Thermally Actuated Shape-Memory Polymers: Experiments, Theory, and Numerical Simulations. *Journal of the Mechanics and Physics of Solids* **2010**, *58* (8), 1100–1124. https://doi.org/10.1016/J.JMPS.2010.04.004.

(6) Nishikawa, M.; Wakatsuki, K.; Yoshimura, A.; Takeda, N. Effect of Fiber Arrangement on Shape Fixity and Shape Recovery in Thermally Activated Shape Memory Polymer-Based Composites. *Composites Part A: Applied Science and Manufacturing* **2012**, *43* (1), 165–173. https://doi.org/10.1016/j.compositesa.2011.10.005.

(7) Voit, W.; Ware, T.; Dasari, R. R.; Smith, P.; Danz, L.; Simon, D.; Barlow, S.; Marder, S. R.; Gall, K. High-Strain Shape-Memory Polymers. *Advanced Functional Materials* **2010**, *20* (1), 162–171. https://doi.org/10.1002/adfm.200901409.

(8) Lee, Y.; Lee, H.; Hwang, T.; Lee, J.-G.; Cho, M. Sequential Folding Using Light-Activated Polystyrene Sheet. *Scientific Reports* **2015**, *5* (1), 16544. https://doi.org/10.1038/srep16544.

(9) Liu, Y.; Boyles, J. K.; Genzer, J.; Dickey, M. D. Self-Folding of Polymer Sheets Using Local Light Absorption. *Soft Matter* **2012**, *8* (6), 1764–1769. https://doi.org/10.1039/C1SM06564E.

(10) Hubbard, A. M.; Mailen, R. W.; Zikry, M. A.; Dickey, M. D.; Genzer, J. Controllable Curvature from Planar Polymer Sheets in Response to Light. *Soft Matter* **2017**, *13* (12), 2299–2308. https://doi.org/10.1039/C7SM00088J.

(11) Gong, X.; Liu, L.; Liu, Y.; Leng, J. An Electrical-Heating and Self-Sensing Shape Memory Polymer Composite Incorporated with Carbon Fiber Felt. *Smart Materials and Structures* **2016**, *25* (3), 035036. https://doi.org/10.1088/0964-1726/25/3/035036.

(12) Liu, Y.; Lv, H.; Lan, X.; Du, S. Review of Electro-Active Shape-Memory Polymer Composite. *Composites Science and Technology* **2009**, *69* (13), 2064–2068. https://doi.org/10.1016/J.COMPSCITECH.2008.08.016.

(13) Luo, X.; Mather, P. T. Conductive Shape Memory Nanocomposites for High Speed Electrical Actuation. *Soft Matter* **2010**, *6* (10), 2146. https://doi.org/10.1039/c001295e.

(14) Egunov, A. I.; Korvink, J. G.; Luchnikov, V. A. Polydimethylsiloxane Bilayer Films with an Embedded Spontaneous Curvature. *Soft Matter* **2016**, *12* (1), 45–52. https://doi.org/10.1039/C5SM01139F.

(15) Stoychev, G.; Turcaud, S.; Dunlop, J. W. C.; Ionov, L. Hierarchical Multi-Step Folding of Polymer Bilayers. *Advanced Functional Materials* **2013**, *23* (18), 2295–2300. https://doi.org/10.1002/adfm.201203245.

(16) Timoshenko, S. Analysis of Bi-Metal Thermostats. *Journal of the Optical Society of America* **1925**, *11* (3), 233. https://doi.org/10.1364/JOSA.11.000233.

(17) Cendula, P.; Kiravittaya, S.; Mei, Y. F.; Deneke, Ch.; Schmidt, O. G. Bending and Wrinkling as Competing Relaxation Pathways for Strained Free-Hanging Films. *Physical Review B* **2009**, *79* (8), 085429. https://doi.org/10.1103/PhysRevB.79.085429.

(18) Mailen, R. W.; Liu, Y.; Dickey, M. D.; Zikry, M.; Genzer, J. Modelling of Shape Memory Polymer Sheets That Self-Fold in Response to Localized Heating. *Soft Matter* **2015**, *11* (39), 7827–7834. https://doi.org/10.1039/C5SM01681A.

(19) Cho, J. W.; Kim, J. W.; Jung, Y. C.; Goo, N. S. Electroactive Shape-Memory Polyurethane Composites Incorporating Carbon Nanotubes. *Macromolecular Rapid Communications* **2005**, *26* (5), 412–416. https://doi.org/10.1002/marc.200400492.

(20) Felton, S. M.; Tolley, M. T.; Shin, B.; Onal, C. D.; Demaine, E. D.; Rus, D.; Wood, R. J. Self-Folding with Shape Memory Composites. *Soft Matter* **2013**, *9* (32), 7688. https://doi.org/10.1039/c3sm51003d.

(21) Cui, J.; Yao, S.; Huang, Q.; Adams, J. G. M.; Zhu, Y. Controlling the Self-Folding of a Polymer Sheet Using a Local Heater: The Effect of the Polymer-Heater Interface. *Soft Matter* **2017**, *13* (21), 3863–3870. https://doi.org/10.1039/c7sm00568g.

(22) So, S.; Hayward, R. C. Tunable Upper Critical Solution Temperature of Poly(N-Isopropylacrylamide) in Ionic Liquids for Sequential and Reversible Self-Folding. *ACS Applied Materials & Interfaces* **2017**, *9* (18), 15785–15790. https://doi.org/10.1021/acsami.7b02953.

(23) Martinez-Agirre, M.; Illescas, S.; Elejabarrieta, M. J. Characterisation and Modelling of Prestrained Viscoelastic Films. *International Journal of Adhesion and Adhesives* **2014**, *50*, 183–190. https://doi.org/10.1016/J.IJADHADH.2014.01.029.

(24) Häusler, K. On the Viscoelastic Properties of Prestrained Rubber. *ZAMP Zeitschrift für angewandte Mathematik und Physik* **1983**, *34* (1), 25–50. https://doi.org/10.1007/BF00962613.

(25) Ge, T.; Robbins, M. O. Anisotropic Plasticity and Chain Orientation in Polymer Glasses. *Journal of Polymer Science Part B: Polymer Physics* **2010**, *48* (13), 1473–1482. https://doi.org/10.1002/polb.22015.

(26) Siwakoti, M.; Mailen, R. W. Relationship between Recovered Enthalpy and the Shape-Memory Effect in Shape Memory Polymers. *Journal of Applied Polymer Science n/a* (n/a), e54727. https://doi.org/10.1002/app.54727.

(27) Bassik, N.; Abebe, B. T.; Laflin, K. E.; Gracias, D. H. Photolithographically Patterned Smart Hydrogel Based Bilayer Actuators. *Polymer* **2010**, *51* (26), 6093–6098. https://doi.org/10.1016/J.POLYMER.2010.10.035.

(28) Wang, J.; Lee, D.; Liu, Y. Joule-Heating Activated Flexible Composite Structures Using Shape Memory Epoxy. In *Volume 1: Advances in Aerospace Technology*; ASME, 2017; p V001T03A028. https://doi.org/10.1115/IMECE2017-72141.

(29) Mailen, R. W.; Dickey, M. D.; Genzer, J.; Zikry, M. A. A Fully Coupled Thermo-Viscoelastic Finite Element Model for Self-Folding Shape Memory Polymer Sheets. *Journal of Polymer Science Part B: Polymer Physics* **2017**, *55* (16), 1207–1219. https://doi.org/10.1002/polb.24372.

(30) Mailen, R. W.; Dickey, M. D.; Genzer, J.; Zikry, M. Effects of Thermo-Mechanical Behavior and Hinge Geometry on Folding Response of Shape Memory Polymer Sheets. *Journal of Applied Physics* **2017**, *122* (19), 195103. https://doi.org/10.1063/1.5000040.

(31) Wang, D.; Lu, C.; Zhao, J.; Han, S.; Wu, M.; Chen, W. High Energy Conversion Efficiency Conducting Polymer Actuators Based on PEDOT:PSS/MWCNTs Composite Electrode †. **2017**. https://doi.org/10.1039/c7ra05469f.

(32) Yu, K.; Zhang, Z.; Liu, Y.; Leng, J. Carbon Nanotube Chains in a Shape Memory Polymer/Carbon Black Composite: To Significantly Reduce the Electrical Resistivity. *Applied Physics Letters* **2011**, *98* (7), 074102. https://doi.org/10.1063/1.3556621.

(33) Leng, J. S.; Huang, W. M.; Lan, X.; Liu, Y. J.; Du, S. Y. Significantly Reducing Electrical Resistivity by Forming Conductive Ni Chains in a Polyurethane Shape-Memory Polymer/Carbon-Black Composite. *Applied Physics Letters* **2008**, *92* (20), 204101. https://doi.org/10.1063/1.2931049.

(34) Sahoo, N. G.; Jung, Y. C.; Yoo, H. J.; Cho, J. W. *Preparation and Properties of Polyurethane Nanocomposites by Functionalization of Multi-Walled Carbon Nanotubes*; 2006.

(35) Leng, J. S.; Lan, X.; Liu, Y. J.; Du, S. Y.; Huang, W. M.; Liu, N.; Phee, S. J.; Yuan, Q. Electrical Conductivity of Thermoresponsive Shape-Memory Polymer with Embedded Micron Sized Ni Powder Chains. *Applied Physics Letters* **2008**, *92* (1), 014104. https://doi.org/10.1063/1.2829388.

(36) Leng, J.; Lv, H.; Liu, Y.; Du, S. Electroactivate Shape-Memory Polymer Filled with Nanocarbon Particles and Short Carbon Fibers. *Applied Physics Letters* **2007**, *91* (14), 144105. https://doi.org/10.1063/1.2790497.

(37) Simulia, 3DS. *Abaqus Analysis User's Guide*.

(38) Williams, M. L.; Landel, R. F.; Ferry, J. D. *The Temperature Dependence of Relaxation Mechanisms in Amorphous Polymers and Other Glass-Forming Liquids*; 1955.

(39) Brinson, H. F.; Brinson, L. C. *Polymer Engineering Science and Viscoelasticity: An Introduction, Second Edition*; Springer US, 2015. https://doi.org/10.1007/978-1-4899-7485-3.

Chapter 5

Relationship between recovered enthalpy and the shape-memory effect in shape memory polymers

(Siwakoti, M., and Mailen, R.W., "Relationship between recovered enthalpy and the shape-memory effect in shape memory polymers", *Journal of Applied Polymer Science*, 2023, DOI: https://doi.org/10.1002/app.54727)

Abstract

SMPs maintain a temporary shape after pre-straining, wherein the polymer chains are constrained in a non-equilibrium thermodynamic state. Physical aging lowers the chain conformational energy, which affects the mechanical properties. Herein, we investigate the relationship between physical aging and the shape recovery of SMP sheets, whereas both processes involve motion of polymer chains. We induce conformational changes to polymer chains either by physical aging or via a thermomechanical pre-straining process. We then quantify structural relaxation via recovered enthalpy measurements using modulated differential scanning calorimetry (MDSC), and the shape recovery performance using dynamic mechanical analysis (DMA). We vary pre-straining holding time, amount, and rate and observe the relationship between physical aging, recovered enthalpy, and the shape recovery performance. The results indicate that an increase in recovered enthalpy correlates with an increase in characteristic shape recovery time. Further, a maximum decrease in recovery time of 65% is observed at the highest strain rate, and only small amounts of recovered enthalpy occur for aging times longer than 16 hours. The results provide insight into the relationship between physical aging and its effects on shape memory, which is important for applications requiring storage for long durations.

5.1. Introduction

Shape memory polymers (SMPs)[1–3] are promising materials for deployable structures using concepts like self-folding origami.[4,5] Benefits of SMPs include their large recoverable strain[6,7], simple pre-straining process[8,9] and variety of external stimuli available to initiate shape change.[10,11] SMPs can retain a temporary shape following a thermomechanical pre-strain sequence and recover their original shape upon the application of external stimuli, such as heat, electromagnetic waves and electricity.[10,12] Pre-straining consists of a series of steps wherein the material is deformed at an elevated temperature (usually above the glass transition temperature, T_g for amorphous polymer or the melting temperature T_m for semi-crystalline polymers), rapidly cooled below T_g and released in the temporary shape.[12] Pre-straining imparts temporary conformations to the polymer chains, manifesting as a residual strain in the bulk material. These temporary conformations are in a thermodynamically non-equilibrium state as the polymer chains are inhibited from rearranging to an equilibrium state due to interactions with neighboring chains, thereby preventing shape recovery.

Pre-strained SMPs are usually stored at temperatures much lower than T_g for potentially long times before their intended end use. During this time, the polymer chains experience a structural relaxation process, also known as *physical aging*[13,14], wherein the higher energy polymer chains slowly approach equilibrium through chain relaxation. During physical aging, non-equilibrium thermodynamic variables, such as enthalpy, entropy, and specific volume decrease monotonically and approach equilibrium.[15,16] These changes occur due to localized changes in polymer chain conformations, which leads to reduced free volume and chain stiffening.[14,17–19] Aging can cause undesired changes to material properties like decreased toughness and increased brittleness.[20–22] In addition, physical aging can cause changes to the characteristic relaxation time

of the polymer.[15,23] Unlike the irreversible processes of chemical[24,25] and hydrothermal aging[26,27], physical aging can be reversed through thermal rejuvenation mechanisms like super-T_g reheating.[28,29] During thermal rejuvenation, the polymer chains are brought to an equilibrium state with their surrounding by raising their temperature above T_g and any previous effects of aging and mechanical loading are erased.[30]

It is predicted that physical aging will also affect the shape recovery performance of SMPs. Previous studies primarily have focused on the effects of naturally occurring physical aging processes[30,31], kinetics, and thermodynamics of aging[15,20,32] on conventional polymers in the absence of a pre-strain sequence. Aging is a relatively slow process, and the material potentially requires a long time to reach its thermodynamic equilibrium, sometimes even millions of years.[31] Recovered enthalpy, one of the thermodynamic variables to measure the extent of aging, has been shown to be largely dependent on the thermal history applied to the polymer, such as aging time, aging temperature, and cooling rate.[15,33,34] Although physical aging has been shown to change the shape recovery performance of an SMP[35,36], the effects of pre-straining on thermodynamic properties, such as recovered enthalpy, were not considered. Further a correlation between physical aging and the shape memory response, *i.e.*, thermally and mechanically induced changes in chain conformations, has not been systematically studied.

In this chapter, we investigate the relationship between physical aging and the shape memory effect for polystyrene (PS) based SMP using dynamic mechanical analysis (DMA)[35,37] and modulated differential scanning calorimetry (MDSC).[31,36] Amorphous PS SMP is selected for its low cost, availability, recyclability, and ease of processing. We start by thermally characterizing unaged PS using DSC then pre-strain the material in a DMA. Pre-straining induces a non-equilibrium state in the polymer chains, which evolves as the material relaxes. We quantify this

effect using MDSC. Finally, we conduct a free-recovery experiment, where the material is allowed to recover its pre-strain without the influence of external force. During free recovery, we measure the performance of the SMP through its characteristic recovery time. These results help us quantify the effects of physically induced aging in the shape recovery performance of SMPs, which in turn provides insight into the processing conditions of the polymer and how those conditions affect their performance.

5.2. Material and methods

Our experimental approach involves an initial characterization of the polystyrene through Fourier transform infrared spectroscopy (FTIR), DSC and DMA, followed by physical aging and pre-straining of polystyrene SMP samples. Changes in the physical and thermodynamic properties due to physical aging and pre-straining are further evaluated through FTIR, MDSC, and DMA as described below.

5.2.1. Sample preparation and initial characterization

The material used in this study is white, 1.5 mm thick amorphous PS sheet, which was purchased from McMaster-Carr and is used in its as-received condition. This material has a number averaged molecular weight of 165000 gm mol^{-1} as measured by gel permeation chromatography (GPC), which is well above the entanglement molecular weight of 12960-14470 gm mol^{-1} as reported in literature.[38] In thermoplastic shape memory polymers, physical entanglements act as anchoring sites to facilitate the shape recovery process. Contrast this with chemical crosslinks in thermosetting SMPs. Amorphous thermoplastic PS offers a low-cost and recyclable SMP with an activation temperature significantly above room temperature, which prevents unintentional activation. The PS sheet was cut into a dog-bone shape, using a CO_2 laser. The overall dimension

of the sample was 44 x 10 x 1.5 mm. The gage section was 15 x 4 mm. The following characterization techniques were utilized to determine the baseline properties of the sample.

5.2.1.1. Fourier transform infrared (FTIR) spectroscopy

FTIR analysis was performed on the sample using a Nicolet 6700 spectrometer. The FTIR test was carried out in the spectrum of 400 cm^{-1} to 4000 cm^{-1} wavenumbers (25 μm to 2.5 μm wavelength respectively), at 64 scans per spectrum and spectral resolution of 2 cm^{-1}. The tests were carried out at room temperature, and an average of three scans were considered for each sample.

5.2.1.2. Differential scanning calorimetry

The T_g was measured using a TA Instruments DSC25. A PS sample (mass = 11.85mg) was subjected to a heat-cool-heat cycle from 40°C to 150°C at a heating and cooling rate of 5°C min^{-1}. The glass transition temperature was measured to be 99.4°C using the midpoint of the change in heat flow during the second heating cycle. This agrees with other measured values of T_g for PS SMP from literature.[1]

5.2.1.3. Dynamic mechanical analysis (DMA)

The viscoelastic properties of PS samples were analyzed using a TA Instruments Discovery HR20 multidrive rheometer through a temperature ramp procedure using a torsion clamp. An ETC is used to control the temperature above ambient throughout the test. The sample was ramped from 80°C to 140°C at a heating rate of 5°C min^{-1}. A fixed angular frequency of 1 rad sec^{-1} was used. These results indicate how the viscoelastic properties of the material vary through the glass transition and are important in understanding the shape recovery response of the amorphous polymer.

5.2.2. Physical aging

A set of the dog-bone samples described in Section 5.2.1 were thermally aged at 90°C (T_g *-10°C*) for various durations in a VWR gravity convection oven. The aging time ranged from 1 hour to 720 hours (30 days). After specific periods of time, individual samples were removed from the oven and characterized. The FTIR spectroscopy and viscoelastic characterization are performed following the procedure mentioned in Section 5.2.1.1 and 5.2.1.3 respectively. However, the calorimetric analysis requires a decomposition of the overlapping signals for glass transition and recovered enthalpy thermal events. For this, the calorimetric analysis is done using a modulated DSC (MDSC) technique. MDSC decomposes the total heat flow signal (received from DSC) into two signals: reversing and non-reversing according to the following relation:[39]

$$\frac{dQ}{dt} = C_p \frac{dT}{dt} + f(T,t) \quad (1)$$

where, *dQ/dt* is the total heat flow, C_p is specific heat capacity, and *dT/dt* is the measured heating rate, which contains both linear and modulated temperature components. The term $C_p\, dT/dt$ is the reversing component of the heat flow, and *f(T,t)* is the non-reversing component of the heat flow, calculated as the difference between the total heat flow and reversing heat flow[40,41] as shown in Figure 5.1a. The reversing heat flow signal represents any changes due to specific heat capacity, such as glass transition, and the non-reversing heat flow signal quantifies all other changes, such as recovered enthalpy.

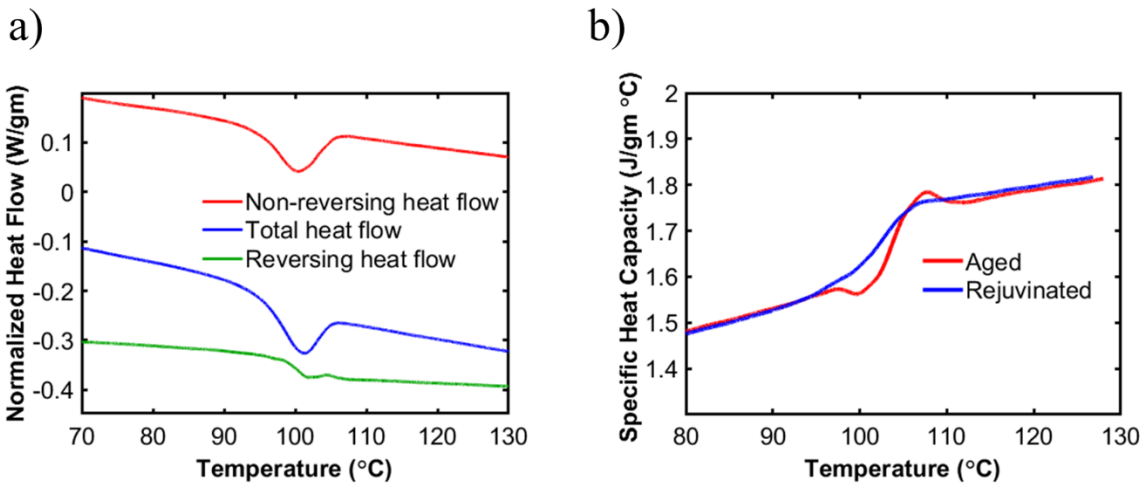

Figure 5.1: a) Example MDSC results where Tg and recovered enthalpy signals are separated through an MDSC test by separating total heat flow into reversing and non-reversing components. b) The changes in specific heat capacities of aged (red) and rejuvenated (blue) samples are used to calculate recovered enthalpy

In the MDSC characterization, the temperature was ramped from 40°C to 150°C at 5°C min^{-1} with a sinusoidal amplitude of 0.796°C and a 60 sec period.[42] After the initial heating ramp, the sample was held at 150°C for 10 mins to thermally rejuvenate, *i.e.*, anneal, the sample. The sample was then cooled to the initial temperature of 50°C at 5°C min^{-1}. One more heating ramp with the same condition as the first ramp was applied to the thermally rejuvenated sample for recovered enthalpy measurement. Recovered enthalpy can be calculated from the two heating cycles according to:[43]

$$\Delta H_a = \int_{T_1}^{T_2} \left(C_p^{aged}(T) - C_p^{rejuv}(T) \right) dT \quad (2)$$

where, C_p^{aged} and C_p^{rejuv} are the heat capacity values of the aged and rejuvenated sample respectively. T_1 and T_2 are temperatures far below and above T_g. The graphical interpretation of this equation is presented in Figure 5.1b. The recovered enthalpy was measured by calculating the difference in the area under the curve of aged and rejuvenated heating cycles.

5.2.3. Thermomechanical processing

The unaged samples were subjected to a thermomechanical pre-straining sequence using a TA Instruments Discovery HR20 multidrive rheometer with DMA mode. A tension fixture was used for mechanical loading and an environmental test chamber (ETC) was used to control temperature.

5.2.3.1. Pre-straining sequence

The thermomechanical loading sequence followed a typical pre-straining procedure shown in Figure 5.2a. First, the temperature was ramped to 110°C, followed by an isotherm for 180 seconds. Then a tensile strain (ε_m) was applied at a constant strain rate ($\dot{\varepsilon}$), followed by cooling the test cell to 90°C at 5°C min^{-1} while holding the strain constant. The temperature and strain were held for a specific time (t_{hold}), *i.e.,* physical aging at 90°C. The material contracts to ε_u following removal of the mechanical load. The efficiency of pre-straining sequence is calculated through shape fixity (R_f) according to the relation:[44]

$$R_f = \frac{\varepsilon_u}{\varepsilon_m} \cdot 100\% \tag{3}$$

To observe the effects of pre-straining variables, the applied pre-strain (ε_m), pre-strain rate ($\dot{\varepsilon}$) and holding time (t_{hold}) were varied individually while keeping the other parameters constant.

The pre-straining sequence was applied to samples for two different experiments. In the first group, the pre-strained samples were cooled to room temperature, removed from the DMA, and a portion of the strained region was collected. From this portion of the sample, we measured the recovered enthalpy for variations on the pre-straining conditions, such as applied strain, strain rate and holding time, following the procedure described in Section 5.2.2. Samples from the second group were kept in the DMA and subjected to shape recovery test after the pre-straining sequence, as described in Section 5.2.3.2.

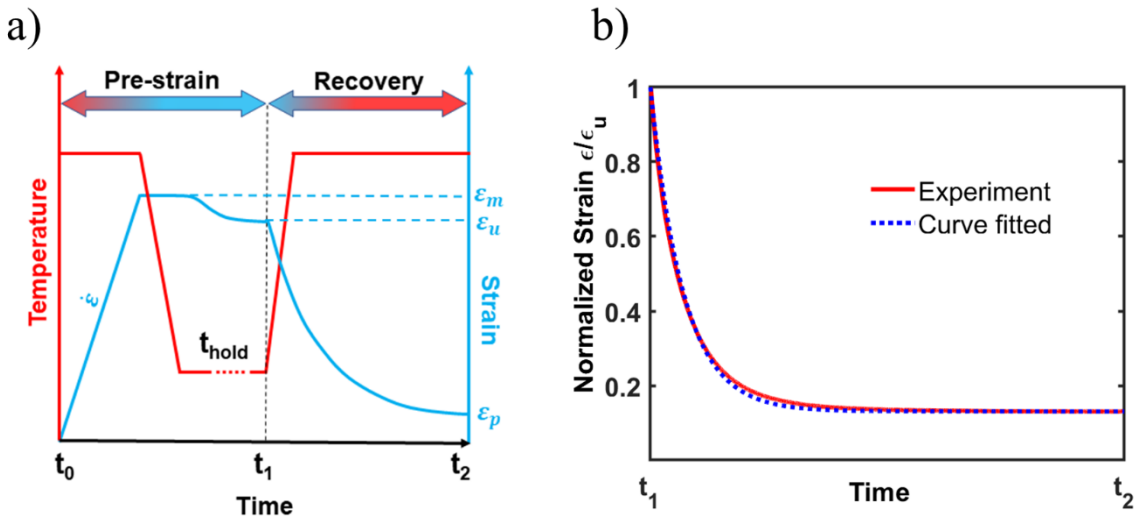

Figure 5.2: a) Thermomechanical loading depicting pre-straining and recovery sequences. Red and blue represents temperature and strain respectively during each procedure and the variables $\varepsilon_m, \dot{\varepsilon}$ and t_{hold} are varied individually to observe their effects on shape recovery performance. b) Representative normalized results of the shape recovery process from t_1 to t_2 approximated with an exponential fit (Equation 3)

5.2.3.2. Shape recovery test

A set of pre-strained samples was subjected to a free-recovery test, wherein the samples were allowed to recover freely from time $t = t_1$ to $t = t_2$ in the DMA under zero-load condition as shown in Figure 5.2a. After pre-straining, the axial force in the sample was set to 0 N +/- 0.1 N. The temperature was then ramped linearly from 90°C to 110°C at a rate of 5°C min^{-1} and held for an hour while the recovery strain was recorded. The recovery strain follows the blue line of the recovery section in Figure 5.2a. The recovery strain normalized with the unloaded strain $(\varepsilon/\varepsilon_u)$ were analyzed to determine a single characteristic recovery time, τ, associated with the sample during shape recovery, *cf.* Figure 5.2b using an exponential fit as:

$$\frac{\varepsilon}{\varepsilon_u} = A + \left((B - A) \cdot \left(1 - e^{-\frac{t}{\tau}}\right)\right) \quad (4)$$

where, the variables A and B are the normalized instantaneous and long-term strains and τ is used to evaluate the speed of recovery. A lower value of τ corresponds to faster recovery of the sample. The efficiency of the recovery process is calculated through shape recovery (R_r) according to the relation:[44]

$$R_r = \frac{\varepsilon_m - \varepsilon_p}{\varepsilon_m} \cdot 100\% \quad (5)$$

5.3. Results and discussion

We report the effects of physical aging on the unstrained polymers via FTIR analysis, followed by characterizing changes in thermodynamic and viscoelastic properties in Section 5.3.1. In Section , we report the effects of pre-straining on recovered enthalpy, evaluate the shape recovery performance of the pre-strained samples using DMA, and relate changes in shape memory performance to recovered enthalpy.

5.3.1. Effects of aging through thermal load

In this section, we report the results from analysis performed according to Sections 5.2.1 through 5.2.3. The changes in various material structure and conformation are reported through FTIR, calorimetric and thermodynamic changes are reported through DSC, and viscoelastic changes are reported using DMA.

5.3.1.1. FTIR spectroscopy

We performed FTIR analysis of unaged and aged PS samples to evaluate conformational changes of the polymer chains due to physical aging. Noteworthy FTIR peaks, *cf.* Figure 5.3 (inset), include the band at 536 cm^{-1}, which is assigned to the conformationally sensitive out-of-plane deformation of the phenyl ring, and the band at 1451 cm^{-1}, which is assigned to the conformationally insensitive CH_2 bend of the polymer chain.[45]

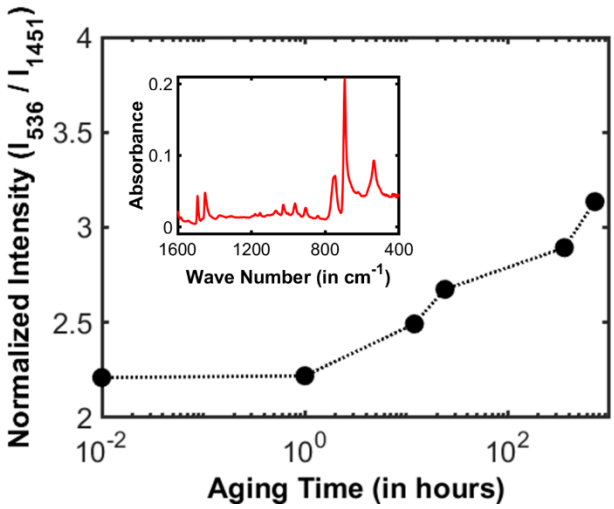

Figure 5.3: Results from FTIR analysis of PS sample. Inset: noteworthy peaks at 536 cm^{-},[1] representing absorption of conformationally sensitive out-of-plane deformation of the phenyl ring, and at 1451 cm^{-1},representing the conformationally insensitive CH_2 bend of the polymer chain. The dots in the main plot represent the normalized intensity of these peaks for various aging time (0 to 720 hours)

Figure 5.3 shows the change in intensity of the peak at 536 cm^{-1} normalized by the peak at 1451 cm^{-1} with increasing aging time. The increase in normalized intensity relates to an increase in the number of phenyl rings that have transitioned to lower-energy conformations during longer aging durations. This relates to physical aging, wherein the polymer chains approach equilibrium by transitioning from high-energy (trans-gauche conformation) to low-energy (trans-trans conformation).[18,46]

5.3.1.2. Calorimetric changes in thermally aged samples

The calorimetric changes of aged samples were analyzed using DSC and compared with an unaged sample following the process described in Section 5.2.2. Figure 5.4a shows the variation in the heat flow signal for the aged samples. In this plot, an increasingly larger endothermic peak in the normalized heat flow near T_g (~100°C) represents an energy barrier (requirement of

additional heat) to heat the material beyond T_g. The endothermic peak is observed to increase significantly with increased aging time as aging allows the polymer chains to relax into lower energy conformations.

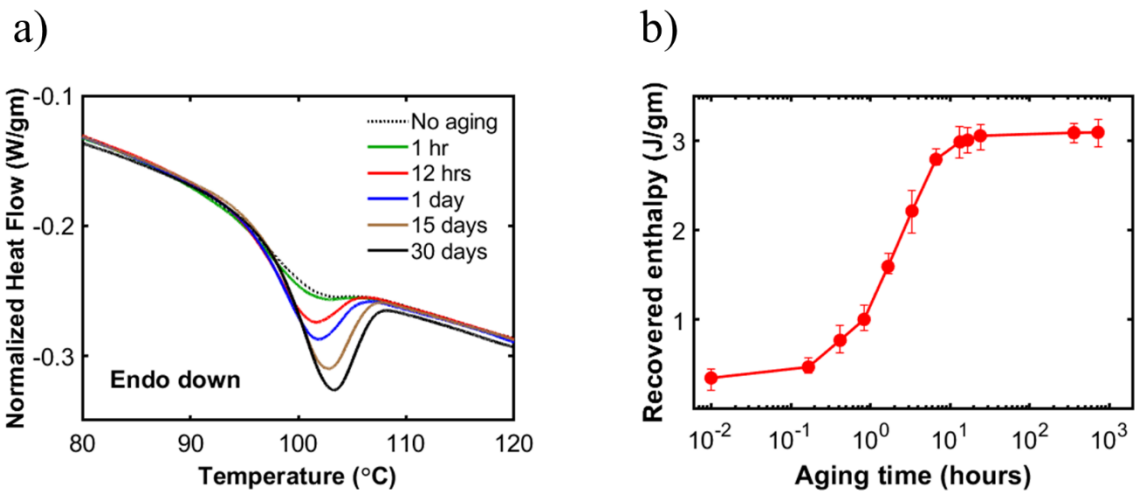

Figure 5.4: a) DSC thermogram showing the amount of heat required to increase the temperature of samples aged at 90°C. b) Recovered enthalpy of polymer samples aged up to 30 days.

The transition to a lower energy conformation creates an additional energy barrier that must be overcome to increase the temperature of the aged sample beyond its T_g. In addition, a small change in glass transition temperature (using the midpoint method), from 99.4°C to 100.6°C, is observed with increasing aging time. This shift is related to the increasing endothermic peak. Figure 5.4b shows the variation in recovered enthalpy of polymer samples aged for up to 30 days. The non-linear growth of recovered enthalpy with increasing aging time relates to the structural relaxation of polymer chains during the aging process, where conformational energy is lost as the chains approach thermodynamic equilibrium at a constant temperature ($T < T_g$). The abrupt increase in recovered enthalpy with aging time between 0.5 hours and 12 hours indicates a higher number of polymer chains relaxing to a lower energy conformation. However, at longer aging

time, the number of polymer chains attaining lower energy configurations saturates and we see very small change in recovered enthalpy with aging time beyond 12 hours at 90°C.

5.3.1.3. Viscoelastic characterization:

The viscoelastic properties of the progressively aged samples are evaluated using DMA. In this analysis of physically aged samples, increased aging time results in structural relaxation of the individual chains, which affects thermodynamic and thermomechanical properties of the polymer. Figure 5.5a shows the storage modulus of samples aged up to 720 hours (30 days). Figure 5.5b shows the changes in loss modulus and Figure 5.5c shows the changes in $\tan\delta$ and the glass transition temperature (peak in $\tan\delta$) with aging time. The change in glass transition temperature according to DMA is small, ranging from 113.13°C to 115.73°C, but has a similar trend to what was observed from DSC. This is explained through the reduction of free volume of the polymer chain during aging[14,15,19], which results in lower mobility and thus stiffening of the polymer chains and a delay in glass transition. The trend of increasing storage modulus due to aging was reported previously.[30,47,48] It is also observed that $\tan\delta$ increases with aging time. Previous studies have discussed the increase in $\tan\delta$ to represent increased damping in the polymer.[49,50] This is counterintuitive to what is expected as typically damping decreases as stiffness increases.

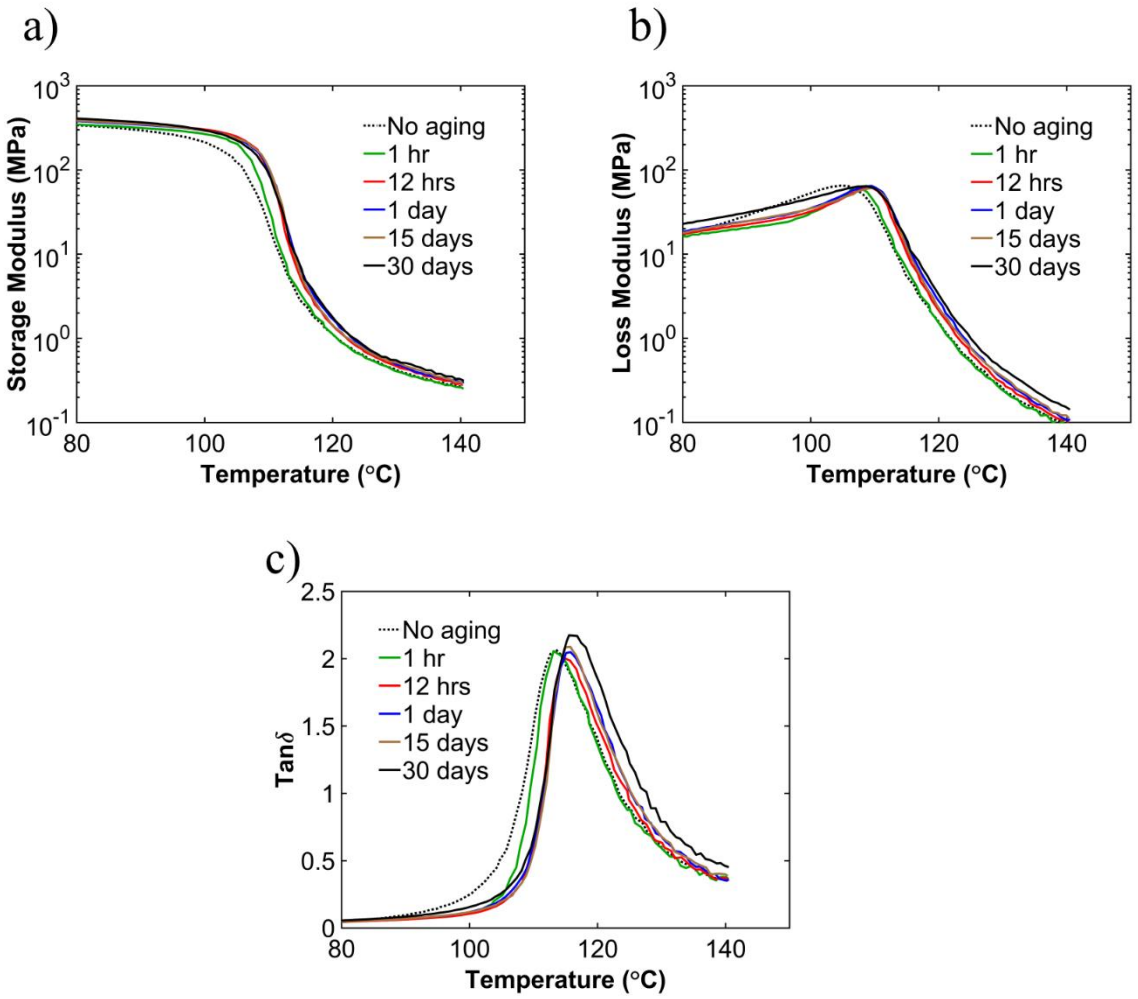

Figure 5.5: Changes in viscoelastic properties reported by a) storage modulus, b) loss modulus and c) tan δ.

We hypothesize that the changes in loss modulus and $\tan\delta$ arise from the chains in the aged polymer being in lower energy conformations, thus offering an ability to absorb more energy by transitioning to higher energy conformations during glass transition. We note here that T_g measured by DMA typically is higher than that by DSC. We also note that the most significant changes in viscoelastic properties occur for samples aged up to 12 hours, and beyond 12 hours of aging, the properties remain constant. This is consistent with the recovered enthalpy results reported in the previous section.

5.3.2. Effects of pre-strain on recovered enthalpy and shape recovery

Next, we report the changes in the thermodynamic state, quantified by recovered enthalpy, of a pre-strained polymer subjected to changes in pre-straining parameters such as holding time, applied strain, and strain rate. This analysis is done after taking the sample out of the DMA at the end of pre-straining sequence and evaluating the pre-strained region of the sample using MDSC as described in Section 5.2.2. Separately, we characterize the shape-recovery performance of similarly pre-strained samples using DMA, as described in Section 5.2.3.2. Herein, we have not attempted to optimize the pre-strain processing conditions. Rather, we focus on the effects of pre-straining conditions on the recovered enthalpy and how this relates to shape recovery. However, the shape fixity and shape recovery ratios for all samples were above 90% and are shown in Figure S5.7.

5.3.2.1. Effects of holding time

Figure 5.6a shows the recovered enthalpy (in red) and the characteristic recovery time (in blue) of pre-strained samples with varying holding times at 90°C . This is equivalent to aging the material for up to 16 hours. The upper limit of 16 hours was due to the limit set by the equipment. It is observed that holding time has a significant effect on recovered enthalpy between 5 minutes (0.083 hours) and 360 minutes (6 hours). The change in holding time has a similar effect on recovered enthalpy as that of physical aging, *cf.* Figure 5.4b and Figure 5.6a, and is attributed to changes in chain conformations to lower-energy states. In addition, structural relaxation slows down at longer times as evidence of almost constant recovered enthalpy beyond a certain time in both processes. This structural relaxation also increases the characteristic recovery time during the shape recovery test, indicating a 25% increase across 16 hours, cf. Figure 5.6a.

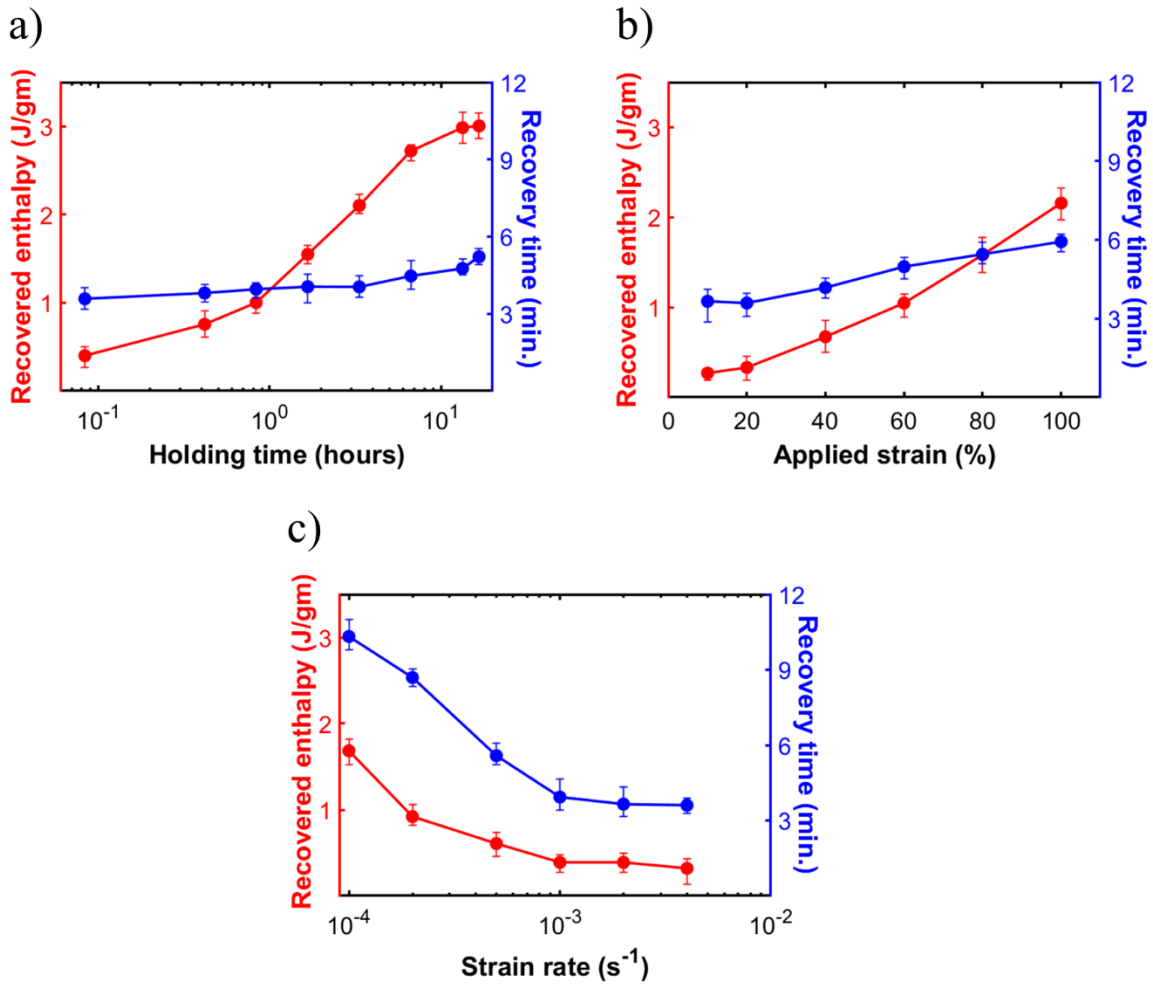

Figure 5.6: Changes in thermodynamic and shape recovery performance parameters considering different pre-straining conditions. Changes in recovered enthalpy (in red) and characteristic recovery time (in blue) are shown for different a) holding time, b) applied strain and c) strain rate.

5.3.2.2. Effects of applied pre-strain

Figure 5.6b shows the recovered enthalpy and the characteristic recovery time of samples with varying amounts of pre-strain . The recovered enthalpy and the characteristic recovery time are seen to increase monotonically with increasing strain amount. Polymer chains experiencing higher amounts of pre-strain become more mechanically aligned, and individual segments rotate to reduce the overall energy in the chain. In turn, the increase in recovered enthalpy correlates to

an increase in characteristic recovery time, with a trend similar to what was observed when changing the holding time at the end of the pre-straining sequence. For samples strained up to 100%, the recovered enthalpy and characteristic recovery time do not saturate. The upper limit of 100% strain was set to minimize the effects of plastic straining, as evidenced by samples having recovery ratios of 93% at 100% strain. When varying the pre-strain amount, the recovered enthalpy follows a polynomial trend, but the characteristic recovery time is fairly linear, again increasing by approximately 25%.

5.3.2.3. Effects of strain rate

Figure 5.6c shows the recovered enthalpy and the characteristic recovery time of samples pre-strained with varying strain rates. Both the recovered enthalpy (in red) and the characteristic recovery time (in blue) are seen to decrease exponentially with increasing strain rate. This can also be explained by the alignment and structural relaxation of polymer chains. At lower strain rates, the polymer chains are able to realign themselves and relax to lower energy conformations. This results in losing more conformational energy and increasing recovered enthalpy in the process. However, at higher strain rates, there is not enough time for the chains to realign and reach lower energy conformations before cooling. This directly affects the shape recovery response of the polymer, where the characteristic recovery time is seen to decrease with higher strain rates. We theorize that the energy stored in these chains is related to bending and stretching of carbon-carbon bonds in the polymer chain backbone, thus accelerating the recovery. However, Increasing the strain rate beyond 10^{-3} s^{-1} has limited effect on both recovered enthalpy and characteristic recovery time.

A trend of recovered enthalpy and characteristic recovery time, therefore, can be established with these results, where the decrease in recovered enthalpy is desirable to achieve

faster shape recovery performance in a shape memory polymer. In consideration of the above, we can now make comparisons between physical aging and shape memory. With increased aging, polymer chains take on lower energy conformations through structural relaxation. This causes an increase in recovered enthalpy with increased aging time. Pre-straining of a polymer induces alignment of the polymer chains, and the energy stored in these chains, as measured by recovered enthalpy, depends on the pre-straining conditions. Further, a correlation between the recovered enthalpy and characteristic recovery time is observed.

5.4. Conclusion

In this chapter, we investigated the relationship between recovered enthalpy and the shape recovery response of SMPs. The effects of physical aging at elevated temperatures and changes to pre-strain variables were considered. Results from FTIR spectroscopy confirmed an increase in the presence of low-energy polymer chain conformations with increased aging time. Further, an increase in recovered enthalpy with increasing aging time was accompanied by an increase in storage modulus. However, only small changes in recovered enthalpy occur for aging times longer than 16 hours. A small but noticeable change in glass transition temperature due to aging was also observed in both MDSC and DMA tests.

In characterizing the shape recovery behavior, we observed that decreases in recovered enthalpy correlate to decreases in characteristic recovery time. For instance, it was observed that a maximum decrease in recovery time of 65% occurred for the highest strain rate, which also caused a significant decrease in recovered enthalpy. Conversely, an increase in recovered enthalpy meant reduction in the shape recovery performance of the polymer. The increase in recovered enthalpy results in a need for additional heating to overcome T_g and an increase in characteristic recovery time. This study enhances our understanding of the relationship between thermodynamic

and thermomechanical properties of SMPs and evaluates new possibilities for quantifying the shape recovery performance of such materials.

5.5. Acknowledgement

The authors would like to acknowledge the work of Dr. Bryan Beckingham and Harrish Kumar for their assistance in performing the GPC analysis.

5.6. Data Availability Statement

The data that support the findings of this study are available from the corresponding author upon reasonable request.

5.7. References

(1) Liu, Y.; Boyles, J. K.; Genzer, J.; Dickey, M. D. Self-Folding of Polymer Sheets Using Local Light Absorption. *Soft Matter* **2012**, *8* (6), 1764–1769. https://doi.org/10.1039/C1SM06564E.

(2) Lendlein, A.; Behl, M.; Hiebl, B.; Wischke, C. Shape-Memory Polymers as a Technology Platform for Biomedical Applications. *Expert Rev Med Devices* **2014**, *7* (3), 357–379.

(3) Kausar, A. Shape Memory Polystyrene-Based Nanocomposite: Present Status and Future Opportunities. *Journal of Macromolecular Science, Part A* **2021**, *58* (3), 182–191. https://doi.org/10.1080/10601325.2020.1840919.

(4) Yasuda, H.; Yang, J. Reentrant Origami-Based Metamaterials with Negative Poisson's Ratio and Bistability. *Phys Rev Lett* **2015**, *114* (18). https://doi.org/10.1103/PhysRevLett.114.185502.

(5) Peraza Hernandez, E. A.; Hartl, D. J.; Akleman, E.; Lagoudas, D. C. Modeling and Analysis of Origami Structures with Smooth Folds. *Computer-Aided Design* **2016**, *78*, 93–106. https://doi.org/10.1016/J.CAD.2016.05.010.

(6) Liu, C.; Qin, H.; Mather, P. T. Review of Progress in Shape-Memory Polymers. *J Mater Chem* **2007**, *17* (16), 1543–1558. https://doi.org/10.1039/b615954k.

(7) Mather, P. T.; Luo, X.; Rousseau, I. A. Shape Memory Polymer Research. *Annu Rev Mater Res* **2009**, *39*, 445–471. https://doi.org/10.1146/ANNUREV-MATSCI-082908-145419.

(8) Atli, B.; Gandhi, F.; Karst, G. Thermomechanical Characterization of Shape Memory Polymers. *J Intell Mater Syst Struct* **2009**, *20* (1), 87–95. https://doi.org/10.1177/1045389X07086689.

(9) van Manen, T.; Janbaz, S.; Zadpoor, A. A. Programming the Shape-Shifting of Flat Soft Matter. *Materials Today* **2017**. https://doi.org/10.1016/j.mattod.2017.08.026.

(10) Meng, H.; Li, G. A Review of Stimuli-Responsive Shape Memory Polymer Composites. *Polymer (Guildf)* **2013**, *54* (9), 2199–2221. https://doi.org/10.1016/J.POLYMER.2013.02.023.

(11) Zende, R.; Ghase, V.; Jamdar, V. A Review on Shape Memory Polymers. *Polymer-Plastics Technology and Materials* **2022**. https://doi.org/10.1080/25740881.2022.2121216.

(12) Mailen, R. W.; Liu, Y.; Dickey, M. D.; Zikry, M.; Genzer, J. Modelling of Shape Memory Polymer Sheets That Self-Fold in Response to Localized Heating. *Soft Matter* **2015**, *11* (39), 7827–7834. https://doi.org/10.1039/C5SM01681A.

(13) Moynihan, C. T.; Macedo, P. B.; Montrose, C. J.; Montrose, C. J.; Gupta, P. K.; DeBolt, M. A.; Dill, J. F.; Dom, B. E.; Drake, P. W.; Easteal, A. J.; Elterman, P. B.; Moeller, R. P.; Sasabe, H.; Wilder, J. A. STRUCTURAL RELAXATION IN VITREOUS MATERIALS*. *Ann N Y Acad Sci* **1976**, *279* (1), 15–35. https://doi.org/10.1111/J.1749-6632.1976.TB39688.X.

(14) Hutchinson, J. M. Physical Aging of Polymers. *Prog Polym Sci* **1995**, *20* (4), 703–760. https://doi.org/10.1016/0079-6700(94)00001-I.

(15) McKenna, G. B.; Simon, S. L. 50th Anniversary Perspective: Challenges in the Dynamics and Kinetics of Glass-Forming Polymers. *Macromolecules* **2017**, *50* (17), 6333–6361. https://doi.org/10.1021/ACS.MACROMOL.7B01014.

(16) Perez-De Eulate, N. G.; Cangialosi, D. The Very Long-Term Physical Aging of Glassy Polymers. *Physical Chemistry Chemical Physics* **2018**, *20* (18), 12356–12361. https://doi.org/10.1039/C8CP01940A.

(17) Campanale, C.; Savino, I.; Massarelli, C.; Uricchio, V. F. Fourier Transform Infrared Spectroscopy to Assess the Degree of Alteration of Artificially Aged and Environmentally Weathered Microplastics. *Polymers 2023, Vol. 15, Page 911* **2023**, *15* (4), 911. https://doi.org/10.3390/POLYM15040911.

(18) Grigoriadi, K.; Putzeys, T.; Wübbenhorst, M.; van Breemen, L. C. A.; Anderson, P. D.; Hütter, M. Effect of Low-Temperature Physical Aging on the Dynamic Transitions of Atactic Polystyrene in the Glassy State. *J Polym Sci B Polym Phys* **2019**, *57* (20), 1394–1401. https://doi.org/10.1002/POLB.24883.

(19) Harms, S.; Rätzke, K.; Faupel, F.; Chaukura, N.; Budd, P. M.; Egger, W.; Ravelli, L. Aging and Free Volume in a Polymer of Intrinsic Microporosity (PIM-1). *J Adhes* **2012**, *88* (7), 608–619. https://doi.org/10.1080/00218464.2012.682902.

(20) Golovchak, R.; Kozdras, A.; Balitska, V.; Shpotyuk, O. Step-Wise Kinetics of Natural Physical Ageing in Arsenic Selenide Glasses. *Journal of Physics: Condensed Matter* **2012**, *24* (50), 505106. https://doi.org/10.1088/0953-8984/24/50/505106.

(21) Shpotyuk, O.; Golovchak, R.; Kozdras, A. Physical Ageing of Chalcogenide Glasses. *Chalcogenide Glasses* **2013**, 209–264. https://doi.org/10.1533/9780857093561.1.209.

(22) Amada, H. T.; Shigeru, O. A.; Kobayashi, K. Physical and Mechanical Properties and Enthalpy Relaxation Behavior of Polyphenylenesulfidesulfone (PPSS). *Polym J* **1993**, *25* (4), 339–346. https://doi.org/10.1295/polymj.25.339.

(23) Nemilov, S. V.; Johari, G. P. A Mechanism for Spontaneous Relaxation of Glass at Room Temperature. *Philosophical Magazine* **2008**, *83* (27), 3117–3132. https://doi.org/10.1080/14786430310001593456.

(24) Lu, X.; Isacsson, U. Artificial Aging of Polymer Modified Bitumens. *J Appl Polym Sci* **2000**, *76*, 1811–1824. https://doi.org/10.1002/(SICI)1097-4628(20000620)76:12.

(25) Yan, C.; Huang, W.; Lin, P.; Zhang, Y.; Lv, Q. Chemical and Rheological Evaluation of Aging Properties of High Content SBS Polymer Modified Asphalt. *Fuel* **2019**, *252*, 417–426. https://doi.org/10.1016/J.FUEL.2019.04.022.

(26) Braun, C. A.; Nam, S. L.; de la Mata, A. P.; Harynuk, J.; Chung, H. J.; Dolez, P. I. Hydrothermal Aging of Polyimide Film. *J Appl Polym Sci* **2022**, *139* (20), 52183. https://doi.org/10.1002/APP.52183.

(27) Dao, B.; Hodgkin, J. H.; Krstina, J.; Mardel, J.; Tian, W. Accelerated Ageing versus Realistic Ageing in Aerospace Composite Materials. IV. Hot/Wet Ageing Effects in a Low Temperature Cure Epoxy Composite. *J Appl Polym Sci* **2007**, *106* (6), 4264–4276. https://doi.org/10.1002/APP.27104.

(28) Cowie, J. M. G.; Ferguson, R. Physical Aging Studies in Polymer Blends. 2. Enthalpy Relaxation as a Function of Aging Temperature in a Poly(Vinyl Methyl Ether)/Polystyrene Blend. *Macromolecules* **1989**, *22* (5), 2312–2317. https://doi.org/10.1021/MA00195A054.

(29) McKenna, G. B.; Kovacs, A. J. Physical Aging of Poly(Methyl Methacrylate) in the Nonlinear Range: Torque and Normal Force Measurements. *Polym Eng Sci* **1984**, *24* (14), 1138–1141. https://doi.org/10.1002/PEN.760241410.

(30) Odegard, G. M.; Bandyopadhyay, A. Physical Aging of Epoxy Polymers and Their Composites. *J Polym Sci B Polym Phys* **2011**, *49* (24), 1695–1716. https://doi.org/10.1002/POLB.22384.

(31) Zhao, J.; Simon, S. L.; McKenna, G. B. Using 20-Million-Year-Old Amber to Test the Super-Arrhenius Behaviour of Glass-Forming Systems. *Nature Communications 2013 4:1* **2013**, *4* (1), 1–6. https://doi.org/10.1038/ncomms2809.

(32) Xu, S.; Sun, C.; Yuan, W.; Zhou, J.; Xu, W.; Zheng, Y.; Yu, C.; Pan, P. Evolution of Thermal Behavior, Mechanical Properties, and Microstructure in Stereocomplexable Poly(Lactic Acid) during Physical Ageing. *Polymer (Guildf)* **2022**, *249*, 124840. https://doi.org/10.1016/J.POLYMER.2022.124840.

(33) Gruber, E. L. G. E. Struik: Physical Aging in Amorphous Polymers and Other Materials. Elsevier Sci. Publ. Comp., Amsterdam-Oxford-New York 1978. 229. *Berichte der Bunsengesellschaft für physikalische Chemie* **1978**, *82* (9), 1019–1019. https://doi.org/10.1002/BBPC.19780820975.

(34) Cangialosi, D.; Boucher, V. M.; Alegría, A.; Colmenero, J. Physical Aging in Polymers and Polymer Nanocomposites: Recent Results and Open Questions. *Soft Matter* **2013**, *9* (36), 8619–8630. https://doi.org/10.1039/C3SM51077H.

(35) Choi, J.; Ortega, A. M.; Xiao, R.; Yakacki, C. M.; Nguyen, T. D. Effect of Physical Aging on the Shape-Memory Behavior of Amorphous Networks. *Polymer (Guildf)* **2012**, *53* (12), 2453–2464. https://doi.org/10.1016/J.POLYMER.2012.03.066.

(36) Hutchinson, J. M.; Cortés, P. Physical Aging of Shape Memory Polymers Based upon Epoxy-Thiol "Click" Systems. *Polym Test* **2018**, *65*, 480–490. https://doi.org/10.1016/J.POLYMERTESTING.2017.12.024.

(37) Guo, J.; Xiao, R.; Tian, C.; Jiang, M. Optimizing Physical Aging in Poly(Ethylene Terephthalate)-Glycol (PETG). *J Non Cryst Solids* **2018**, *502*, 15–21. https://doi.org/10.1016/J.JNONCRYSOL.2018.10.021.

(38) Likhtman, A. E.; McLeish, T. C. B. Quantitative Theory for Linear Dynamics of Linear Entangled Polymers. *Macromolecules* **2002**, *35* (16), 6332–6343. https://doi.org/10.1021/ma0200219.

(39) Thomas, L. C. *Modulated DSC ® Paper #1 Why Modulated DSC ® ? ; An Overview and Summary of Advantages and Disadvantages Relative to Traditional DSC*; 2005.

(40) Verdonck, E.; Schaap, K.; Thomas, L. C. A Discussion of the Principles and Applications of Modulated Temperature DSC (MTDSC). *Int J Pharm* **1999**, *192* (1), 3–20. https://doi.org/10.1016/S0378-5173(99)00267-7.

(41) Dweck, J. Obtaining Modulated Temperature DSC Curves through a Non-Conventional DSC Method. *J Therm Anal Calorim* **2000**, *60* (3), 785–793. https://doi.org/10.1023/A:1010191220888.

(42) Thomas, L. C. *Modulated DSC ® Paper #3 Modulated DSC ® Basics; Optimization of MDSC ® Experimental Conditions*; TA Instruments, 2005. https://www.tainstruments.com/pdf/literature/TP_008_MDSC_num_3_Optimization_of_Experimental_Conditions.pdf.

(43) Brunacci, A.; Cowie, J. M. G.; Ferguson, R.; McEwen, I. J. Enthalpy Relaxation in Glassy Polystyrenes: 1. *Polymer (Guildf)* **1997**, *38* (4), 865–870. https://doi.org/10.1016/S0032-3861(96)00575-7.

(44) Tobushi, H.; Hara, H.; Yamada, E.; Hayashi, S. Thermomechanical Properties in a Thin Film of Shape Memory Polymer of Polyurethane Series. *Smart Mater Struct* **1996**, *5* (4), 483–491. https://doi.org/10.1088/0964-1726/5/4/012.

(45) Jung, M. R.; Horgen, F. D.; Orski, S. V.; Rodriguez C., V.; Beers, K. L.; Balazs, G. H.; Jones, T. T.; Work, T. M.; Brignac, K. C.; Royer, S. J.; Hyrenbach, K. D.; Jensen, B. A.; Lynch, J. M. Validation of ATR FT-IR to Identify Polymers of Plastic Marine Debris, Including Those Ingested by Marine Organisms. *Mar Pollut Bull* **2018**, *127*, 704–716. https://doi.org/10.1016/J.MARPOLBUL.2017.12.061.

(46) Enns, J. B.; Boyer, R. F.; Ishida, H.; Koenig, J. L. Fourier Transform Infrared Spectroscopic Study of Transitions above Tg in Atactic Polystyrene. *Polym Eng Sci* **1979**, *19* (10), 756–759. https://doi.org/10.1002/PEN.760191016.

(47) Soloukhin, V. A.; Brokken-Zijp, J. C. M.; Van Asselen, O. L. J.; De With, G. Physical Aging of Polycarbonate: Elastic Modulus, Hardness, Creep, Endothermic Peak, Molecular Weight Distribution, and Infrared Data. **2003**. https://doi.org/10.1021/ma0342980.

(48) Barral, L.; Cano, J.; Lopez, J.; Lopez-Bueno, I.; Nogueira, P.; Abad, M. J.; Ramirez, C. Physical Aging of an Epoxy/Cycloaliphatic Amine Resin. *Eur Polym J* **1999**, *35* (3), 403–411. https://doi.org/10.1016/S0014-3057(98)00132-3.

(49) Jafari, S.; Nourany, M.; Zakizadeh, M.; Taghilou, A.; Ranjbar, H. A.; Noormohammadi, F. The Effect of Controlled Phase Separation of PEG/PCL-2000 Homopolymer Polyols Using Their

PCL500-PEG1000-PCL500 Tri-Block Copolymer and CNCs in the Final Polyurethane Hydrogels on Their Shape Memory Behavior. *Composites Communications* **2020**, *19*, 194–202. https://doi.org/10.1016/j.coco.2020.03.016.

(50) Aboueimehrizi, E.; Makaremy, M. A.; Bazrpash, S.; Noormohammadi, F.; Darestani, Y. R.; Nourany, M. Synthesis of High-Modulus Thermoset PUs of PCL-PTMG/CNW Biomaterials with Different Soft Domain Architecture and Composition for High Shape Memory Performance. *Cellulose* **2022**, *29* (16), 8651–8674. https://doi.org/10.1007/s10570-022-04796-z.

5.8. Supplemental Information

Relationship between recovered enthalpy and the shape-memory effect in shape memory polymers

Figure S5.7 shows the shape fixity and shape recovery ratios for the pre-strained samples. These results indicate high shape memory performance, with both properties being above 90% for all samples.

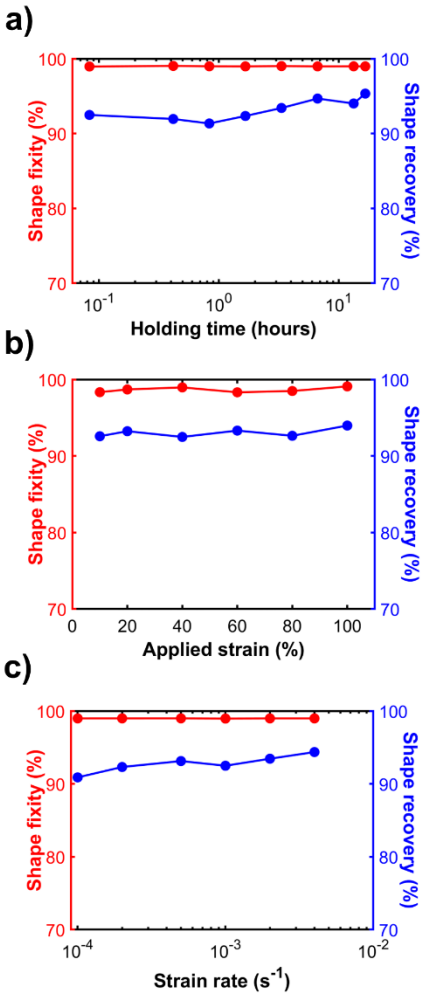

Figure S5.7: Shape fixity and shape recovery ratios for all samples as a function of (a) holding time, (b) applied strain, and (c) strain rate.

Chapter 6

Effects of UV-aging on shape recovery performance of shape memory polymers

(This chapter is being prepared for submission)

Abstract

Space represents a harsh environment for all materials. This is particularly challenging for shape memory polymers (SMPs), which show significant potential for lightweight actuators for deployable space structures. Relevant environmental conditions in low earth orbit (LEO) space include UV radiation, temperature variations, and vacuum. Polymers, when exposed to such an environment for prolonged period (aging), begin to break down structurally and thermodynamic properties, such as enthalpy, entropy, and specific volume, change over time. This leads to permanent modification of mechanical properties such as decreased strength and increased brittleness of the polymer. In addition, performance of SMPs rely on structural configurations of their polymer chains, which when exposed to prolonged UV radiations, decreases significantly. Previous studies focused on the effects of UV exposure on chemical degradation of polymers. However, limited research has been conducted towards studying the effect of UV aging on shape recovery performance of SMPs. In this study, we expose a polymer in a UV environment followed by shape recovery experiments where the material is pre-strained and recovered. Furthermore, we use characterization techniques such as FTIR and DSC to evaluate the amount of degradation of SMP as a result of UV aging process. The results obtained from this study will provide insight into recovery capabilities of a SMP for space exploration.

6.1. Introduction

Shape memory polymers (SMPs) are a class of active materials that possess the ability to change their shape in response to external stimuli, such as heat and light.[1–3] SMPs are preferred

over other active materials due to their low cost[4,5], large recoverable strain[6,7], and availability of numerous external stimuli[8,9]. SMPs are widely used to transform two-dimensional sheets into three-dimensional structures through the self-folding origami process[10,11]. Self-folding of such polymer requires thermomechanical programming (pre-straining) of a polymer and its subsequent shape recovery response[12,13]. SMPs have attracted significant attention in recent years due to their potential applications in fields such as biomedicine[14,15], soft robotics[16,17], and space exploration[2,18]. However, the long-term durability of SMPs under various environmental conditions, such as high temperature, moisture, sunlight, and UV exposure, remains a critical challenge for their practical applications. Exposure to such conditions can degrade the polymers reversibly (through physical aging)[19–22] or irreversibly (through photochemical degradation)[23–25]. The irreversible degradation, such as degradation due to UV-C exposure (wavelength of 100-280nm)[23,25] and atomic oxygen[26,27] in the low earth orbit (LEO), irreversibly affect the structural configuration of the polymer. UV radiation and atomic oxygen are present in an abundant amount in LEO space[28,29] and therefore, needs to be investigated for applications that require shape recovery performance of SMPs at LEO.

UV radiation is a common environmental factor that has irreversible effects on the performance of polymers[25,30,31]. Energetic UV-C radiation breaks down polymer chains through chain scission[32,33] and introduces foreign functional groups that weaken the polymer chains[25,34]. Prolonged exposure to UV radiation (UV aging) can cause irreversible photochemical degradation of the polymer chains, resulting in a reduction of mechanical[35–37] and thermal properties[34,36] of the material. Despite the importance of understanding the effects of UV aging on SMPs, there is a lack of systematic studies on how UV aging affects the shape memory performance. Previous studies on UV aging of polymers have reported changes in physical properties such as discoloration and cracks[38,39], reduction in mechanical properties such as hardness, tensile, and flexure strength[40–42],

and surface properties, such as wear resistance and surface degradation of aged polymers[40,41,43]. In addition, UV aging has been shown to change the viscoelastic response of a polymer[44,45]. However, a fundamental study of this change connecting the recovery of SMPs is missing.

This chapter examines the effects of prolonged UV and atomic oxygen exposure on viscoelastic behavior of polystyrene and its subsequent effect on shape recovery performance of the SMP. We use various characterizing techniques such as Fourier transform infrared spectroscopy (FTIR), dynamic mechanical analysis (DMA), and differential scanning calorimetry (DSC) to evaluate and analyze the effects caused by UV aging of SMP on its recovery response. We start by aging the polymer under UV-C radiation of wavelength 254nm for multiple periods of time, ranging from 1 hour to 24 hours. This induces irreversible damage to the polymer chains which we evaluate through spectroscopic study using FTIR. We quantify the thermal property changes through DSC and the viscoelastic changes through DMA. We perform the shape recovery tests to measure the performance of the SMP and evaluate the effects of UV exposure on the performance. In free recovery, the sample is allowed to recover freely without the influence of external force, while in constrained recovery tests, it is constrained from recovering and the evolution of axial force is measured. These results help us quantify the effects of prolonged UV aging in the shape recovery performance of SMPs, which in turn provides insight into the long-term usage of such polymers in harsh space environments.

6.2. Materials and method

This study involves an initial characterization of polystyrene through FTIR, DSC and DMA, followed by UV aging and thermomechanical pre-straining of our samples. Changes in the physical properties due to UV aging are further evaluated through FTIR, DSC, and DMA as described below.

6.2.1. Sample preparation and initial characterization

The material used in this study is an amorphous PS sheet, (number averaged molecular weight, M_n = 165000 gm mol^{-1}) of thickness 1.5 mm, purchased from McMaster-Carr and is used in its as-received condition. The PS sheet was cut into a dog-bone shape, using a CO_2 laser. The overall dimension of the sample was 44 x 10 x 1.5 mm with the gage section being 15 x 4 mm as shown in Figure 6.1. The following characterization techniques were utilized to determine the baseline properties of the sample.

Figure 6.1: Polystyrene sample used for UV aging, pre-straining and shape recovery tests

6.2.1.1. Fourier transform infrared (FTIR) spectroscopy

FTIR analysis was performed on the sample using a Nicolet 6700 spectrometer. The FTIR test was carried out in the spectrum of 400 cm^{-1} to 4000 cm^{-1} wavenumbers (25 μm to 2.5 μm wavelength respectively), at 64 scans per spectrum and spectral resolution of 2 cm^{-1}. The tests were carried out at room temperature, and an average of three scans were considered for each sample.

6.2.1.2. Differential scanning calorimetry

The T_g was measured using a TA Instruments DSC25. A PS sample (mass = 10 - 15mg) was subjected to a heat-cool-heat cycle from 40°C to 150°C at a heating and cooling rate of 5°C min^{-1}. The glass transition temperature was measured to be 99.4°C using the midpoint of the change in heat flow during the second heating cycle. This agrees with other measured values of T_g for PS SMP from literature[46].

6.2.1.3. Dynamic mechanical analysis (DMA)

The viscoelastic properties of PS samples were analyzed using a TA Instruments Discovery HR20 multidrive rheometer through a temperature ramp procedure using a torsion clamp. An environment test chamber (ETC) is used to control the temperature above ambient throughout the test. The sample was ramped from 80°C to 140°C at a heating rate of 5°C min^{-1}. A fixed angular frequency of 1 rad sec^{-1} was used. The results of this test indicate how the viscoelastic properties of the material vary through the glass transition and are important in understanding the shape recovery response of the amorphous polymer.

6.2.2. UV aging

A set of the dog-bone samples described in Section 3.1 were UV aged from 1 hour to 24 hours in a Jelight Model 18 UV+O cleaner, cf. Figure 6.2a. According to the manufacturer, UV radiation of 254nm wavelength with an average intensity of 30mW/cm^{-2} at a distance of 4mm was emitted from the Mercury vapor UV grid lamp[47]. The samples were removed from the UV cleaner at a specific time and were characterized for spectroscopic analysis using FTIR, calorimetric analysis using DSC, and viscoelastic analysis using DMA.

Polystyrene undergoes rapid photo oxidation in the presence of UV light and oxygen. Photo oxidation process at shorter wavelengths (~254nm), is initiated from the absorption of light by the phenyl group present in the polystyrene chain backbone[48]. The energy absorbed by the phenyl group (*R*) leads to the initial scission of tertiary C-H bond and forms a radical (H°) according to[25]:.

$$RH \rightarrow R^{\circ} + H^{\circ} \quad (1)$$

The H° radical reacts with oxygen to form a peroxy radical (ROO°), which in turn abstracts hydrogen from nearby polymer chains to form a hydroperoxide (R-OOH).

$$R^{\circ} + O_2 \rightarrow ROO^{\circ} \quad (2)$$

$$ROO^{\circ} + RH \rightarrow ROOH + R^{\circ} \quad (3)$$

The hydroperoxide then decomposes with a chain scission leading to the formation of acetophenone ($C_6H_5C(=O)\text{-}CH_3$), ketone (R-C(=O)-R'), and water.

$$ROOH \rightarrow RO^{\circ} + OH^{\circ} \quad (4)$$

$$2ROOH \rightarrow RO^{\circ} + ROO^{\circ} + H_2O \quad (5)$$

The prolonged exposure to UV-aging will thus break the polymer chain backbone through chain scission and weakens the structural configuration and mechanical properties of the polymer.

Further, the prolonged exposure to the UV radiation causes color change in polymers where the color of the polymer surfaces changes to yellow for multiple aging time, as seen in Figure 6.2b. This has been known to occur due to the formation of chromophoric groups such as polyene (diene, triene and tetraene) and acetophenone[49].

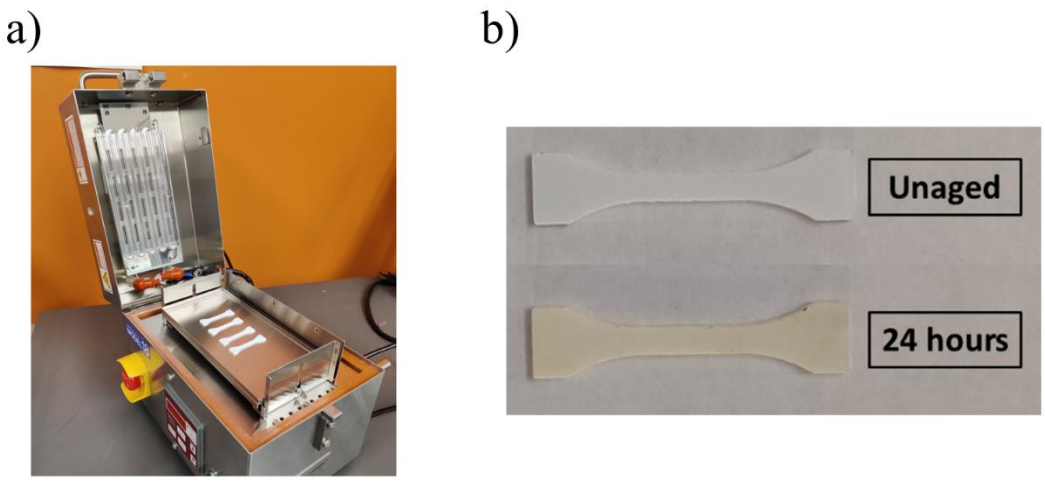

Figure 6.2: Prolonged exposure of polymer samples to UV-C radiation and atomic oxygen in a) Jelight Model 18 UV+O cleaner. The samples were kept at 4mm distance from the light source, and b) polystyrene changing color to yellow as a result of prolonged UV exposure.

6.2.3. Pre-straining and shape recovery

The aged and unaged samples were subjected to a thermomechanical pre-straining sequence using a TA Instruments Discovery HR20 multidrive rheometer with DMA mode. A tension fixture was used for mechanical loading and an environmental test chamber (ETC) was used to control temperature.

The thermomechanical loading sequence followed a typical pre-straining procedure shown in Figure 6.3. First, the temperature was ramped to 110°C, followed by an isotherm for 180 seconds. Then a tensile strain (ε_m) was applied at a constant strain rate ($\dot{\varepsilon}$), followed by cooling the test cell to 90°C at 5°C min^{-1} while holding the strain constant. The temperature and strain were held for 5 minutes. The material contracts to ε_u following removal of the mechanical load.

The pre-strained sample was subjected to a free-recovery test, wherein the samples were allowed to recover freely from time $t = t_1$ to $t = t_2$ in the DMA under zero-load condition as shown

in Figure 6.3. After pre-straining, the axial force in the sample was set to 0 N +/- 0.1 N (limited by the equipment). The temperature was then ramped linearly from 90°C to 110°C at a rate of 5°C min^{-1} and held for an hour while the recovery strain was recorded. The recovery strain follows the blue line of the recovery section in Figure 6.3.

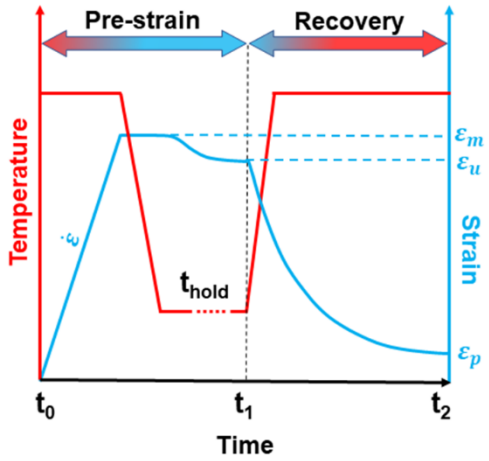

Figure 6.3: Thermomechanical loading depicting pre-straining and recovery sequences. Red and blue represents temperature and strain respectively during each procedure.

The efficiency of the recovery process is calculated through shape recovery (R_r) according to the relation:[44]

$$R_r = \frac{\varepsilon_m - \varepsilon_p}{\varepsilon_m} \cdot 100\% \quad (6)$$

6.3. Results and discussion

In this section, we report the results from analysis performed according to Sections 6.2.1 through 6.2.3. The changes seen from prolonged UV exposure in polymer chain backbone are reported through FTIR, calorimetric changes are reported through DSC, viscoelastic changes and shape recovery are reported using DMA.

6.3.1. FTIR spectroscopy

We performed FTIR analysis of unaged and aged polystyrene samples to evaluate chain scission of the polymer chains due to UV aging. The IR spectra is shown in Figure 6.4a, where the spectrum of interest is shown in the inset. The presence of chain scission through photooxidative degradation was calculated through the oxidation index (OI). It is the ratio between the intensity of carbonyl functional group (formed due to chain scission during UV aging) at 1720 cm^{-1} and that of reference group at 1600 cm^{-1} as[50]

$$OI = \frac{I_{1720}}{I_{1600}} \tag{7}$$

Figure 6.4b shows an increase in the oxidation index with exposure time. The increase in oxidation index confirms the structural degradation of polymer chains during prolonged UV aging and is comparable to the existing literature[50,51].

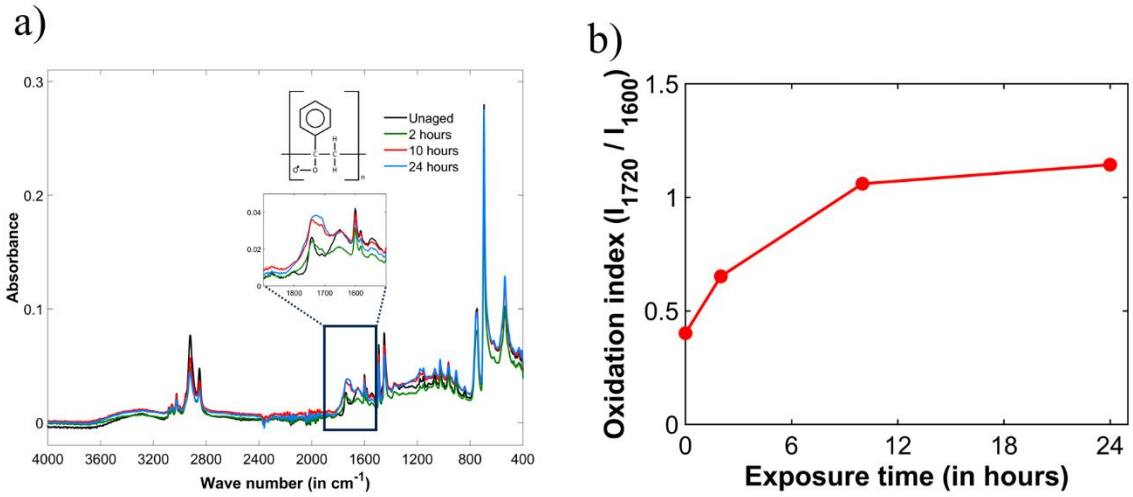

Figure 6.4: Results from FTIR analysis of UV aged polystyrene. Inset: spectrum of interest for carbonyl functional group formed during UV aging. b) Oxidation index with exposure time, showing an increase in the intensity of chain scission in polymer chains with UV aging.

6.3.2. DSC calorimetry

The calorimetric changes of UV aged samples were analyzed using DSC and compared with an unaged sample following the process described in Section 6.2.2. Figure 6.5 shows the variation in glass transition temperature with UV aging time. An initial decrease in T_g can be seen with samples aged for 4 hours and remains fairly constant throughout the end (24 hours). This is explained by a large number of polymer chains undergoing chain scission during the initial aging time. This introduces a number of new functional groups in the polymer chain and breaks the chain structure, which in turn reduces the glass transition temperature. At higher aging time however, the chain scission within the polymer chains saturate and we see very little change in the glass transition temperature.

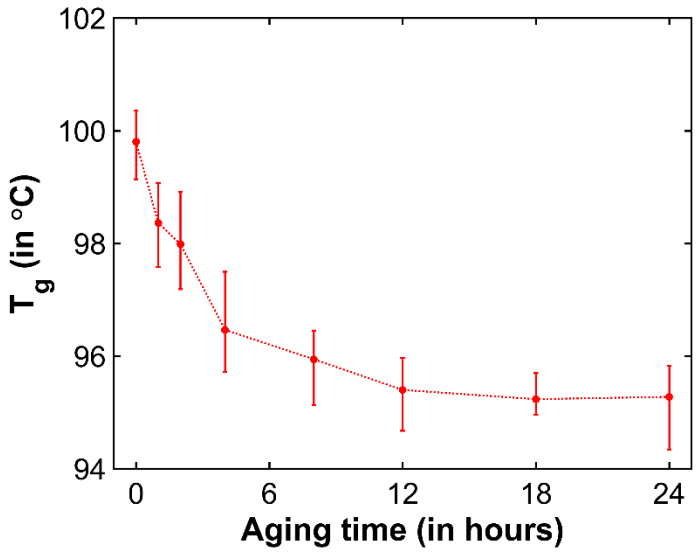

Figure 6.5: Glass transition temperature at multiple UV aging time. Multiple samples were aged from 1 to 24 hours and their average glass transition temperatures were recorded through multiple DSC runs.

6.3.3. Viscoelastic characterization

The viscoelastic properties of the UV aged samples are evaluated using the DMA. Figure 6.6a shows the change in storage modulus of the polymer for progressively increasing aging time, Figure 6.6b shows the change in loss modulus and Figure 6.6c shows the changes in tanδ with aging. We see an increase in storage modulus with aging time. It is due to the fact that with UV aging, the polymer chains breaks down and entangles with each other more, thereby requiring more energy to go through the glass transition.

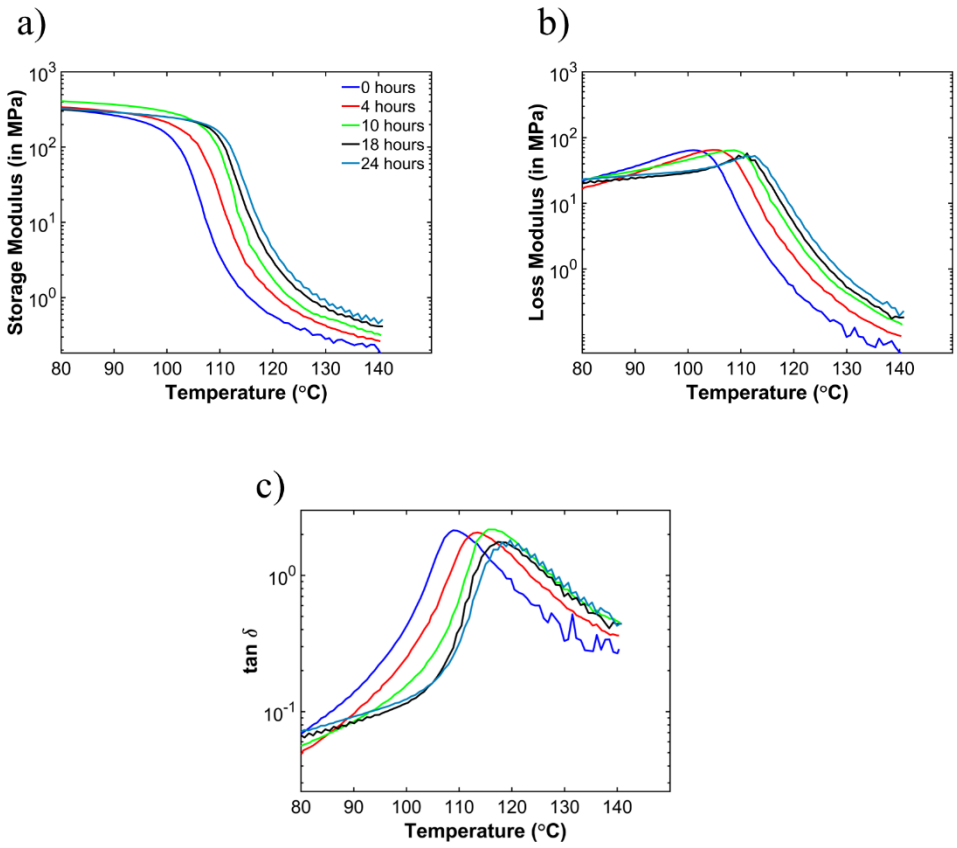

Figure 6.6: Changes in viscoelastic properties reported by a) storage modulus, b) loss modulus and c) tan δ.

6.3.4. Shape recovery characterization

The shape recovery performance of the UV aged samples are evaluated using the DMA. Figure 6.7 shows shape recovery ratio of samples aged for multiple time periods. In the inset of Figure 6.7, it can be seen that the recovery ratio is decreasing with increasing aging time. This signifies a loss in shape recovery performance of the UV aged polymer caused due to chain scission of polymer chains. This reduces the amount of strain recovered from the polymer and diminishes the shape memory performance of samples aged for longer period of time.

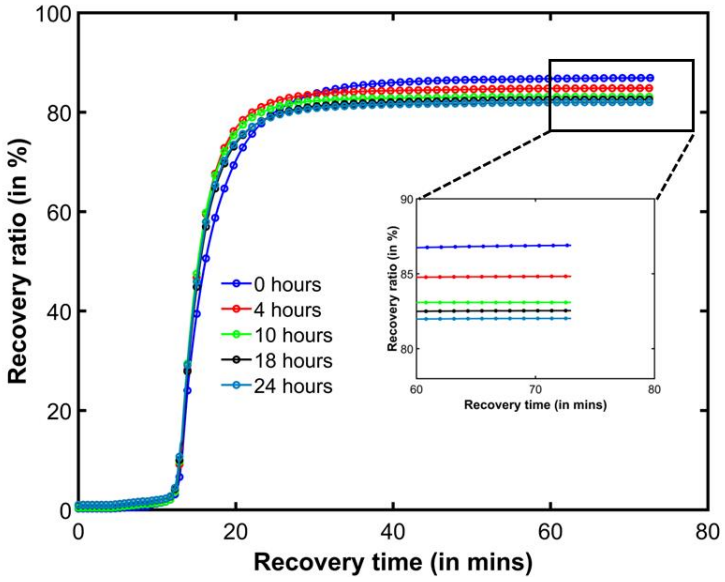

Figure 6.7: Shape recovery performance measured by the recovery ratio. The pre-strained sample were freely recovered for an hour and the corresponding shape recovery ratio is recorded for multiple aging time.

6.4. Conclusion

In this chapter, we studied the effects of UV radiation and atomic oxygen in shape recovery performance of SMPs. Prolonged exposure to UV radiation degrades the polymer chains by chain scission, introducing foreign functional groups and weakening the polymer. Initial results include

yellowing of the polymer with aging and FTIR spectroscopy confirmed an increase in the presence of carbonyl functional group generated by UV aging through chain scission in the polymer chains. The calorimetric analysis show a decrease of glass transition temperature with aging time, however viscoelastic analysis show an increase of glass transition temperature with aging time. This is an ongoing study and needs to be analyzed closely.

The analysis of shape recovery behavior shows a decrease in final shape recovery ratio with increasing aging time, signifying a reduction in shape recovery performance of UV aged polymer. To overcome this reduction in mechanical and viscoelastic performance, we would suggest either limiting the exposure of these polymers to UV radiation or coating the polymer with UV reflective coating on the surface. This study improves our understanding of the effects of prolonged UV exposure in shape recovery behavior and laid the experimental foundation for the next phase of this study, i.e., sending samples to the LEO for 6 months and analyzing the effects of environmental conditions such as exposure to UV radiation and atomic oxygen.

6.5. Future Works

This chapter presents an experimental setup for evaluating shape memory polymers undergoing prolonged UV and atomic oxygen exposure. The samples are exposed to these conditions for a maximum of an hour and need further exposure time to get a complete picture. As a continuation of this work, we have sent some of our samples to the international space station (ISS), where these samples are exposed to space environments, such as UV-C radiation and atomic oxygen for 6-months. The experiment is a part of materials international space station experiments (MISSE), where the samples will be exposed to the space environments at two different orbital directions, zenith and wake[52]. As a part of this experiment, a total of 8 samples were sent. First set of 5 samples were thermoplastics polymers, including polystyrene, aluminum coated polystyrene,

Polyimide (Kapton) coated polystyrene, acrylic, and polyethylene terephthalate glycol (PETG), each with a dimension of 1 in. x 1.5 in with thickness of less than 0.4 in.

The other set of 3 samples were thermoset polymer resin mixed at different combinations. The constituents chemicals used to prepare the thermoset resin were an epoxy base of EPON 826, Jeffamine D-230, used as crosslinker, and neopentyl glycol diglycidyl ether (NGDE) was used as a reactive diluent[53]. These materials were mixed in combinations following the literature[53]. The solution was prepared by pre-melting EPON 826 at 75°C for 15 minutes, followed by mixing Jeffamine and NGDE and mixing it vigorously by hand for 5 minutes. The solution is then transferred to a Teflon mold and cured at 100°C for 1 hour, followed by a second cure at 130°C for 1 hour. The thermoset polymers were left to cool and collected for the MISSE experiment.

The prolonged exposure to the space environment will degrade the polymers and weaken their thermomechanical performance. We will evaluate this degradation by subjecting the samples, brought back from the ISS to the experiment procedures outlined in this chapter. This will increase the exposure time of the samples and provide a better understanding of shape recovery performance of SMPs for future space exploration.

6.6. References

(1) Herath, M.; Epaarachchi, J.; Islam, M.; Fang, L.; Leng, J. Light Activated Shape Memory Polymers and Composites: A Review. *European Polymer Journal* **2020**, *136*, 109912. https://doi.org/10.1016/J.EURPOLYMJ.2020.109912.

(2) Jayalath, S.; Herath, M.; Epaarachchi, J.; Trifoni, E.; Gdoutos, E. E.; Fang, L. Durability and Long-Term Behaviour of Shape Memory Polymers and Composites for the Space Industry -

A Review of Current Status and Future Perspectives. *Polymer Degradation and Stability* **2023**, *211*, 110297. https://doi.org/10.1016/J.POLYMDEGRADSTAB.2023.110297.

(3) Mailen, R. W.; Liu, Y.; Dickey, M. D.; Zikry, M.; Genzer, J. Modelling of Shape Memory Polymer Sheets That Self-Fold in Response to Localized Heating. *Soft Matter* **2015**, *11* (39), 7827–7834. https://doi.org/10.1039/C5SM01681A.

(4) Cooper, C. B.; Nikzad, S.; Yan, H.; Ochiai, Y.; Lai, J. C.; Yu, Z.; Chen, G.; Kang, J.; Bao, Z. High Energy Density Shape Memory Polymers Using Strain-Induced Supramolecular Nanostructures. *ACS Central Science* **2021**, *7* (10), 1657–1667. https://doi.org/10.1021/ACSCENTSCI.1C00829.

(5) Pieczyska, E. A.; Staszczak, M.; Maj, M.; Kowalczyk-Gajewska, K.; Golasiński, K.; Cristea, M.; Tobushi, H.; Hayashi, S. Investigation of Thermomechanical Couplings, Strain Localization and Shape Memory Properties in a Shape Memory Polymer Subjected to Loading at Various Strain Rates. *Smart Materials and Structures* **2016**, *25* (8), 085002. https://doi.org/10.1088/0964-1726/25/8/085002.

(6) Liu, C.; Qin, H.; Mather, P. T. Review of Progress in Shape-Memory Polymers. *Journal of Materials Chemistry* **2007**, *17* (16), 1543–1558. https://doi.org/10.1039/b615954k.

(7) Mather, P. T.; Luo, X.; Rousseau, I. A. Shape Memory Polymer Research. *Annual Review of Materials Research* **2009**, *39*, 445–471. https://doi.org/10.1146/ANNUREV-MATSCI-082908-145419.

(8) Meng, H.; Li, G. A Review of Stimuli-Responsive Shape Memory Polymer Composites. *Polymer* **2013**, *54* (9), 2199–2221. https://doi.org/10.1016/J.POLYMER.2013.02.023.

(9) Zende, R.; Ghase, V.; Jamdar, V. A Review on Shape Memory Polymers. *Polymer-Plastics Technology and Materials* **2022**. https://doi.org/10.1080/25740881.2022.2121216.

(10) Peraza-Hernandez, E. A.; Hartl, D. J.; Malak, R. J.; Lagoudas, D. C. Origami-Inspired Active Structures: A Synthesis and Review. *Smart Materials and Structures* **2014**, *23* (9). https://doi.org/10.1088/0964-1726/23/9/094001.

(11) Kamrava, S.; Mousanezhad, D.; Ebrahimi, H.; Ghosh, R.; Vaziri, A. Origami-Based Cellular Metamaterial with Auxetic, Bistable, and Self-Locking Properties. *Scientific Reports* **2017**, *7*. https://doi.org/10.1038/SREP46046.

(12) Atli, B.; Gandhi, F.; Karst, G. Thermomechanical Characterization of Shape Memory Polymers. *Journal of Intelligent Material Systems and Structures* **2009**, *20* (1), 87–95. https://doi.org/10.1177/1045389X07086689.

(13) Shojaei, A.; Xu, W.; Yan, C.; Yang, Q.; Li, G. Insight in Thermomechanical Constitutive Modeling of Shape Memory Polymers. *Frontiers in Mechanical Engineering* **2022**, *8*, 83. https://doi.org/10.3389/FMECH.2022.956129/BIBTEX.

(14) Lendlein, A.; Behl, M.; Hiebl, B.; Wischke, C. Shape-Memory Polymers as a Technology Platform for Biomedical Applications. *Expert Review of Medical Devices* **2014**, *7* (3), 357–379. https://doi.org/10.1586/ERD.10.8.

(15) Hager, M. D.; Bode, S.; Weber, C.; Schubert, U. S. Shape Memory Polymers: Past, Present and Future Developments. *Progress in Polymer Science* **2015**, *49–50*, 3–33. https://doi.org/10.1016/J.PROGPOLYMSCI.2015.04.002.

(16) Lendlein, A.; Gould, O. E. C. Reprogrammable Recovery and Actuation Behaviour of Shape-Memory Polymers. *Nature Reviews Materials 2018 4:2* **2019**, *4* (2), 116–133. https://doi.org/10.1038/s41578-018-0078-8.

(17) Xia, Y.; He, Y.; Zhang, F.; Liu, Y.; Leng, J.; Xia, Y.; He, Y.; Zhang, F.; Leng, J.; Liu, Y. A Review of Shape Memory Polymers and Composites: Mechanisms, Materials, and Applications. *Advanced Materials* **2021**, *33* (6), 2000713. https://doi.org/10.1002/ADMA.202000713.

(18) Li, F.; Liu, Y.; Leng, J. Progress of Shape Memory Polymers and Their Composites in Aerospace Applications. *SMaS* **2019**, *28* (10), 103003. https://doi.org/10.1088/1361-665X/AB3D5F.

(19) Brunacci, A.; Cowie, J. M. G.; Ferguson, R.; Mcewen, I. J. Enthalpy Relaxation in Glassy Polystyrenes: 1. **1997**, *38* (4), 865–870.

(20) McKenna, G. B.; Kovacs, A. J. Physical Aging of Poly(Methyl Methacrylate) in the Nonlinear Range: Torque and Normal Force Measurements. *Polymer Engineering & Science* **1984**, *24* (14), 1138–1141. https://doi.org/10.1002/PEN.760241410.

(21) McKenna, G. B.; Simon, S. L. 50th Anniversary Perspective: Challenges in the Dynamics and Kinetics of Glass-Forming Polymers. *Macromolecules* **2017**, *50* (17), 6333–6361. https://doi.org/10.1021/ACS.MACROMOL.7B01014.

(22) Siwakoti, M.; Mailen, R. W. Relationship between Recovered Enthalpy and the Shape-Memory Effect in Shape Memory Polymers. *Journal of Applied Polymer Science n/a* (n/a), e54727. https://doi.org/10.1002/app.54727.

(23) Amza, C. G.; Zapciu, A.; Baciu, F.; Radu, C. Effect of UV-C Radiation on 3D Printed ABS-PC Polymers. *Polymers* **2023**, *15* (8). https://doi.org/10.3390/POLYM15081966.

(24) Angulo, A. L.; Rodriguez, C. L. C.; Fechine, G. J. M. Photooxidative Behavior of Polystyrene Nanocomposites Filled with Two-Dimensional Molybdenum Disulfide. *Polymers 2023, Vol. 15, Page 2099* **2023**, *15* (9), 2099. https://doi.org/10.3390/POLYM15092099.

(25) Yousif, E.; Haddad, R. Photodegradation and Photostabilization of Polymers, Especially Polystyrene: Review. *SpringerPlus* **2013**, *2* (1). https://doi.org/10.1186/2193-1801-2-398.

(26) Goto, A.; Umeda, K.; Yukumatsu, K.; Kimoto, Y. Property Changes in Materials Due to Atomic Oxygen in the Low Earth Orbit. *CEAS Space J* **2021**, *13* (3), 415–432. https://doi.org/10.1007/s12567-021-00376-2.

(27) Tennyson, R. C. Atomic Oxygen Effects on Polymer-Based Materials. *Can. J. Phys.* **1991**, *69* (8–9), 1190–1208. https://doi.org/10.1139/p91-180.

(28) Han, J.-H.; Kim, C.-G. Low Earth Orbit Space Environment Simulation and Its Effects on Graphite/Epoxy Composites. *Composite Structures* **2006**, *72* (2), 218–226. https://doi.org/10.1016/j.compstruct.2004.11.007.

(29) Kemnitz, R. A.; Cobb, G. R.; Singh, A. K.; Hartsfield, C. R. Characterization of Simulated Low Earth Orbit Space Environment Effects on Acid-Spun Carbon Nanotube Yarns. *Materials & Design* **2019**, *184*, 108178. https://doi.org/10.1016/j.matdes.2019.108178.

(30) Naveen, R.; Kumar, M.; Ramesh, M.; Abinaya, R.; Prasath, M. An Investigation on Effect of Ultraviolet (UV) Rays on Mechanical Properties of Epoxy Laminates. *Materials Today: Proceedings* **2023**. https://doi.org/10.1016/j.matpr.2023.06.257.

(31) Regel, V. R.; Chernyi, N. N.; Kryzhanovskii, V. G.; Boboev, T. B. Effect of Ultraviolet Radiation on the Creep Rate of Polymers. *Polymer Mechanics* **1967**, *3* (3), 272–275. https://doi.org/10.1007/BF00858764.

(32) Aslanzadeh, S.; Kish, M. H. Photo-Oxidation of Polypropylene Fibers Exposed to Short Wavelength UV Radiations. *Fibers and Polymers* **2010**, *11* (5), 710–718. https://doi.org/10.1007/S12221-010-0710-8/METRICS.

(33) Bocchini, S.; Frache, A. Comparative Study of Filler Influence on Polylactide Photooxidation. *Express Polymer Letters* **2013**, *7* (5), 431–442. https://doi.org/10.3144/EXPRESSPOLYMLETT.2013.40.

(34) Tidjani, A. Photooxidation of Polypropylene Under Natural and Accelerated Weathering Conditions. *J Appl Polym Sci* **1997**, *64*, 2497–2503. https://doi.org/10.1002/(SICI)1097-4628(19970627)64:13.

(35) Frigione, M.; Rodríguez-Prieto, A. Can Accelerated Aging Procedures Predict the Long Term Behavior of Polymers Exposed to Different Environments? *Polymers 2021, Vol. 13, Page 2688* **2021**, *13* (16), 2688. https://doi.org/10.3390/POLYM13162688.

(36) Boubakri, A.; Guermazi, N.; Elleuch, K.; Ayedi, H. F. Study of UV-Aging of Thermoplastic Polyurethane Material. *Materials Science and Engineering: A* **2010**, *527* (7–8), 1649–1654. https://doi.org/10.1016/J.MSEA.2010.01.014.

(37) Rodriguez, A. K.; Mansoor, B.; Ayoub, G.; Colin, X.; Benzerga, A. A. Effect of UV-Aging on the Mechanical and Fracture Behavior of Low Density Polyethylene. *Polymer Degradation and Stability* **2020**, *180*, 109185. https://doi.org/10.1016/J.POLYMDEGRADSTAB.2020.109185.

(38) Nakatani, H.; Ohshima, Y.; Uchiyama, T.; Suguru, M. Degradation and Fragmentation Behavior of Polypropylene and Polystyrene in Water. *Scientific Reports 2022 12:1* **2022**, *12* (1), 1–7. https://doi.org/10.1038/s41598-022-23435-y.

(39) Gulmine, J. V.; Akcelrud, L. Correlations between Structure and Accelerated Artificial Ageing of XLPE. *European Polymer Journal* **2006**, *42* (3), 553–562. https://doi.org/10.1016/J.EURPOLYMJ.2005.09.006.

(40) Redjala, S.; Aït Hocine, N.; Ferhoum, R.; Gratton, M.; Poirot, N.; Azem, S. UV Aging Effects on Polycarbonate Properties. *Journal of Failure Analysis and Prevention* **2020**, *20* (6), 1907–1916. https://doi.org/10.1007/S11668-020-01002-9.

(41) Shi, Z.; Zou, C.; Zhou, F.; Zhao, J. Analysis of the Mechanical Properties and Damage Mechanism of Carbon Fiber/Epoxy Composites under UV Aging. *Materials* **2022**, *15* (8). https://doi.org/10.3390/MA15082919.

(42) Lizárraga-Laborín, L. L.; Quiroz-Castillo, J. M.; Encinas-Encinas, J. C.; Castillo-Ortega, M. M.; Burruel-Ibarra, S. E.; Romero-García, J.; Torres-Ochoa, J. A.; Cabrera-Germán, D.; Rodríguez-Félix, D. E. Accelerated Weathering Study of Extruded Polyethylene/Poly (Lactic Acid)/Chitosan Films. *Polymer Degradation and Stability* **2018**, *155*, 43–51. https://doi.org/10.1016/J.POLYMDEGRADSTAB.2018.06.007.

(43) Toohey, K. S.; Blanchet, T. A.; Heckelman, D. D. Effect of Accelerated Aging Conditions on Resultant Depth-Dependent Oxidation and Wear Resistance of UHMWPE Joint Replacement Bearing Materials. *Wear* **2003**, *255* (7–12), 1076–1084. https://doi.org/10.1016/S0043-1648(03)00270-9.

(44) Farroni, F.; Sakhnevych, A.; Timpone, F.; Genovese, A. Ultraviolet Light Radiation Effects on Viscoelastic Property Variation in Polymers. *Journal of Materials Engineering and Performance 2023 32:9* **2023**, *32* (9), 3896–3904. https://doi.org/10.1007/S11665-023-08180-1.

(45) Varghese, A. M.; Rangaraj, V. M.; Luckachan, G.; Mittal, V. UV Aging Behavior of Functionalized Mullite Nanofiber-Reinforced Polypropylene. *ACS Omega* **2020**, *5* (42), 27083–27093. https://doi.org/10.1021/ACSOMEGA.0C02437.

(46) Liu, Y.; Boyles, J. K.; Genzer, J.; Dickey, M. D. Self-Folding of Polymer Sheets Using Local Light Absorption. *Soft Matter* **2012**, *8* (6), 1764–1769. https://doi.org/10.1039/C1SM06564E.

(47) UVO-CLEANER - Instruction Manual. https://www.jelight.com/manuals/.

(48) Rabek, Jan. F. *Polymer Photodegradation*; Springer Netherlands: Dordrecht, 1995. https://doi.org/10.1007/978-94-011-1274-1.

(49) Kim, H.-Y.; Ashim, J.; Park, S.; Kim, W.; Ji, S.; Lee, S.-W.; Jung, Y.-R.; Jeong, S. W.; Lee, S.-G.; Kim, H.-C.; Lee, Y.-J.; Kwon, M. K.; Hwang, J.-S.; Shin, J. M.; Lee, S.-J.; Yu, W.; Park, J.-K.; Choi, S.-K. A Preliminary Study about the Potential Risks of the UV-Weathered Microplastic: The Proteome-Level Changes in the Brain in Response to Polystyrene Derived Weathered

Microplastics. *Environmental Research* **2023**, *233*, 116411. https://doi.org/10.1016/j.envres.2023.116411.

(50) Castro Monsores, K. G. de; Silva, A. O. da; Sant' Ana Oliveira, S. de; Weber, R. P.; Filho, P. F.; Monteiro, S. N. Influence of Ultraviolet Radiation on Polystyrene. *Journal of Materials Research and Technology* **2021**, *13*, 359–365. https://doi.org/10.1016/j.jmrt.2021.04.035.

(51) Remili, C.; Kaci, M.; Kachbi, S.; Bruzaud, S.; Grohens, Y. Photo-Oxidation of Polystyrene/Clay Nanocomposites under Accelerated UV Exposure: Effect on the Structure and Molecular Weight. *Journal of Applied Polymer Science* **2009**, *112* (5), 2868–2875. https://doi.org/10.1002/app.29806.

(52) *MISSE*. Glenn Research Center | NASA. https://www1.grc.nasa.gov/space/iss-research/misse/ (accessed 2023-10-02).

(53) Rousseau, I. A.; Xie, T. Shape Memory Epoxy: Composition, Structure, Properties and Shape Memory Performances. *Journal of Materials Chemistry* **2010**, *20* (17), 3431–3441. https://doi.org/10.1039/B923394F.

Chapter 7

Characterization of electrospun, conducting polymer electrodes enabling mobility for all

(This chapter is being prepared for submission)

Abstract

Humans have evolved sensitive biological sensors, e.g., eyes and ears, to observe and respond to changes in their environments. Signals from these sensors can initiate a response before the human is even consciously aware of their reaction. This response plays out in the form of muscle activations, i.e., an electrochemical reaction that activates a muscular response. In this work, we seek to design, fabricate, and characterize compliant, conformal, electrospun fabric-based sensors capable of measuring wearer stress levels and intent detection. These sensors may be integrated at the human-machine interface in such a way that enables collection of rich data streams, e.g., surface electromyography (sEMG), electrodermal activity (EDA, or galvanic skin response), and pressure, that can be used to improve operator safety. Further, these fabric-based sensors are intended to be minimally intrusive, which will enhance wearer comfort and thereby lead to more regular use. Herein, we will utilize electrospinning of conducting polymers to fabricate non-woven electrodes and sensors. We will characterize the electrical, thermal, and mechanical performance of these electrodes and make comparisons to state-of-art sensors. These capabilities will enable novel end-use cases, including capturing vehicle operator states, improving the quality of prosthetic socket design, and the control of wearable exoskeletons to enable walking and fall prevention, with particular benefit for individuals with reduced sensation and motor abilities, such as those recovering from stroke or spinal cord injuries (SCI).

7.1. Introduction

Electrospinning is a fiber manufacturing process that produces nanofibers in the order of nanometers to micrometers in diameter.[1] It is a versatile fiber manufacturing technique used in the field of nanotextiles[2,3], drug delivery[4], and industrial products ranging from pollutant filtration[5] to commodity goods such as face masks.[6] Due to their high surface-area-to-volume ratio, electrospun fibers can mimic the morphology of fibers found in human tissue and have been used in applications such as wound-healing[7] and tissue engineering[8]. In addition to biomedical applications, electrospun fiber of conducting polymers, unlike the majority of organic polymers, have unique electrical properties, making them advantageous for applications such as energy storage[9], sensors[10], and flexible electronics wearables[11,12].

The electrospinning process involves applying high electric voltages, in the order of tens of kV, to create an electrostatic field that draws a polymer solution from a syringe or spinneret towards a grounded collector plate, cf. Figure 7.1a[13,14]. The polymer solution can be fed through the syringe at a constant rate using a syringe pump. When an electrostatic field is created from the applied electric voltage, the polymer solution droplet at the syringe nozzle gets electrically charged and the charges are distributed over the surface. The collection of these charges deforms the droplet into a cone, known as the Taylor cone, cf. Figure 7.1b. This accumulation of charges creates a repulsive force which overcomes the surface tension of the droplet at higher electrostatic field strength and a jet of polymer solution is ejected from the Taylor cone[15,16]. The jet of polymer solution goes through a process of evaporation and extreme elongation due to the applied electric field, thereby leaving behind a solid, continuous fiber.

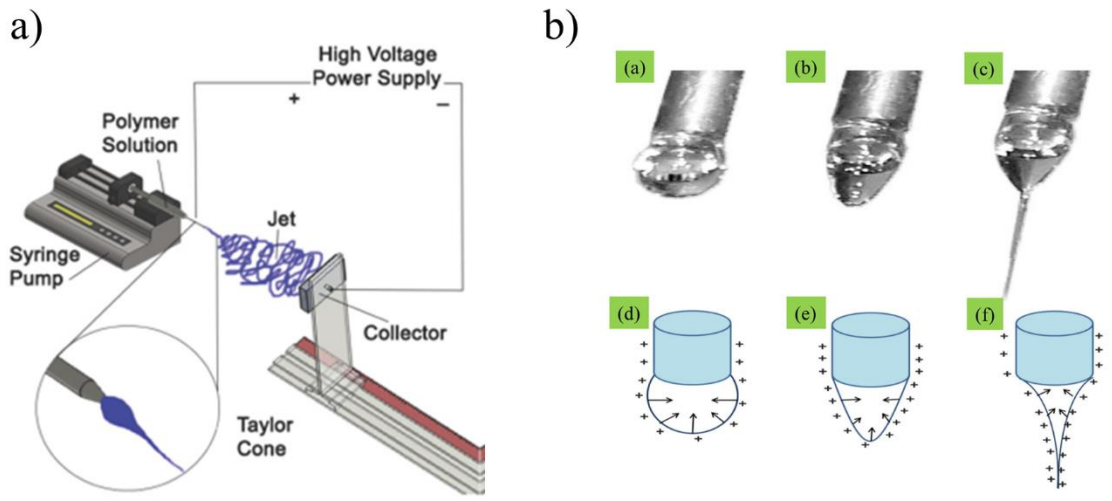

Figure 7.1: a) Electrospinning schematic showing polymer solution being pushed through a nozzle by a syringe pump. The high voltage power supplied deforms the solution droplet into a Taylor cone (inset)[14]. b) The charge accumulated creates a repulsive force that overcomes the surface tension of the droplet that stretches the polymer solution and deposits the fiber to the grounded collector plate[15,16].

These fibers are collected in a grounded collector plate, or a grounded spinning drum to create a fiber mat.[1] One of the key advantages of electrospinning conducting polymer fibers is their tunable properties. By adjusting various processing parameters, such as polymer concentration, applied electric voltages, and the collector distance, researchers can control the diameter, morphology, and alignment of the resulting fibers.[13] This level of control allows for tailoring the fibers to specific applications. In addition to morphology, electrospinning processes can also be tailored for applications requiring electrical conductivity from the fiber mats.

In recent years, researchers have used polymers such as polyaniline[17,18], polypyrrole[19,20], and poly(3,4-ethylenedioxythiophene) polystyrene sulfonate (PEDOT:PSS)[21], cf. Figure 7.2a-c to

electrospin fiber mats with an electrical conductivity range of 10^{-6} to 10^{1} S/cm.[22–24] The source of electrical conductivity in these polymers are due to the conjugated polymer chain backbone, i.e., their polymer chain consists of alternating single and double bonds as seen in Figure 7.2b.[25,26] Both of these bonds contain strong σ-bond between them while double bonds also contain a weaker π-bond. The electrons in p-orbitals of the π-bonds are overlapped and can move freely between the backbone atoms, thus providing the source of electrical conductivity.[25–29] The conductivity of these polymers can often be enhanced by introducing dopants such as camphorsulfonic acid (CSA) and p-toluene sulfonic acid (PTSA).[30,31] The addition of dopants introduces charge carriers into the backbone, by adding or removing electrons to or from the polymer backbone.[26,27,32]

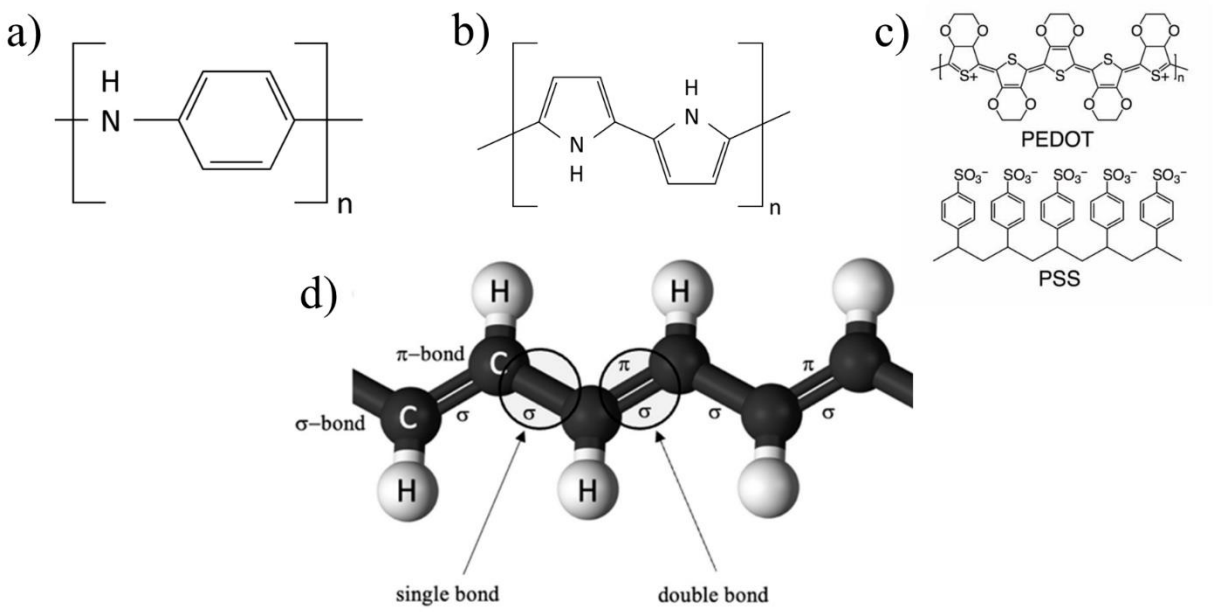

Figure 7.2: Monomer unit of a) polyaniline, b) polypyrrole and c) PEDOT:PSS containing alternating single and double bond. d) The chemical structure depicting the σ and π bond present in the alternating single and double bond. The overlap of electrons in p-orbitals of the π bonds can move freely between the atoms, thus providing the source of electrical conductivity in these polymers.

Apart from electrical conductivity, biocompatibility is another property that is crucial in creating electrospun biological sensors. Polymers with excellent biocompatibility have been used to assist drug delivery for the treatment of spinal cord injury (SCI)[33] or injured arterial vessels.[34]

In this work, we developed an in-house electrospinning process to fabricate conducting polymer fiber mats, with a goal to use in biosensing applications. Next, we performed mechanical, morphological and electrical characterization of these fiber mats. Finally, we studied their signal sensing performance based on electrical signals received from muscle actuations during various hand gestures.

7.2. Material and methods

We start our experiment procedure by first preparing the polymer solvents. Next, we produce fiber mats through electrospinning process. Next, we carry out the mechanical, morphological and electrical characterization of the fiber mat.

7.2.1. Materials

In the preparation of the electrospinning solutions, Polyaniline (*PANI*) doped with PTSA (Alfa Aesar, 043683, M_w = 17,500 gm/mol), N,N-Dimethylformamide (*DMF*) (VWR, BDH1117-4LP, M_w = 73.09 gm/mol), Polyvinyl alcohol (*PVA*) (VWR, 470302-040, M_w = 100,000 gm/mol), Poly(3,4-ethylenedioxythiophene) polystyrene sulfonate (*PEDOT:PSS*) (synthesized in-house at department of chemical engineering, Auburn University) and deionized (DI) water were used as received.

7.2.2. Solution preparation

The first set of conducting polymer solution was prepared by dissolving 0.2 5 wt% to 1 wt% doped PANI powder in DMF and stirring it with a magnetic stirrer for 24 hours at room

temperature. The second set of conducting polymer (PEDOT:PSS) was used in its as received condition. The processability of these conducting polymers are poor, therefore a carrier polymer, such as PVA, is mixed with the conducting polymer solution to assist in electrospinning process[35]. 10 wt% PVA solution was prepared by dissolving PVA powder in DI water and stirred for 24 hours at 80°C. Each conducting polymer solution was mixed in ratio of 1:3 PANI : PVA (or PEDOT:PSS : PVA) and was transferred to a 10ml syringe for electrospinning. This mixing ratio provided the best processability of the conducting polymer solution during electrospinning and produced the best conductivity value.

7.2.3. Electrospinning

The polymer solution prepared from section 7.2.2 was electrospun at room temperature. The solution was electrospun through a 20 gage blunt-tip needle, at 1ml hr^{-1} flow rate, 18-20kV voltage, and 10cm gap between the needle-tip and the collector plate. The collector plate was covered with aluminum foil for fiber collection and was grounded. The electrospinning was done for 2 hours and characterization of these electrospun fibers were performed.

7.2.4. Characterization of electrospun fibers

Fibers produced from section 7.2.3 were characterized using the following characterization techniques.

7.2.4.1. Scanning electron microscopy (SEM)

SEM images of the electrospun fibers were taken from Thermoscientific Phenom ProX desktop SEM. The sample fibers were attached to a copper tape and analyzed under 5kV of accelerating voltage.

7.2.4.2. Tensile testing

The tensile test of the electrospun fibers were carried out in TA Instruments' HR20 equipped with a 50 N load cell, with a crosshead separation speed of 3 mm min^{-1}. The width of the sample was measured using a digital caliper and the thickness was measured using Mitutoyo IP42 digital indicator on a flat granite base. Six measurements were performed, and average value was reported as its thickness. The fibers were then anchored to the test frame by wrapping their endpoints in Aluminum foil to avoid slippage during the test[36]. The test was performed at room temperature until the strain applied reached 100%. The mechanical design criteria of the electrospun fibers was to withstand 10-15% strain without breaking, as is expected from muscle actuation during EDA sensing.

7.2.4.3. 4-point probe conductivity

DC electrical conductivity measurements were carried out through an in-house 4-point probe shown in Figure 7.3a. The 4-point probe were acquired from the electrical engineering department at Auburn University and consists of four retractable pogo pins for proper fiber contact. The pins were placed equidistant along the board and the electrical measurements were taken by Keysight 34465A digital multimeter.

The sheet resistance of the fiber was measured from the schematic shown in Figure 7.3b according to the relation[37]:

$$R_S = \frac{2\pi}{ln(2)} \cdot \frac{\Delta V}{I} \quad (1)$$

where, ΔV and I are the applied voltage and resulting current output respectively. The electrical conductivity is calculated according to the relation[37]:

$$\sigma = \frac{1}{R_s \cdot t} \tag{2}$$

where, t is the average thickness of the fiber. For each fiber mat, the thickness measurements were carried out six times, electrical conductivity measurements were carried out nine times and average value is reported.

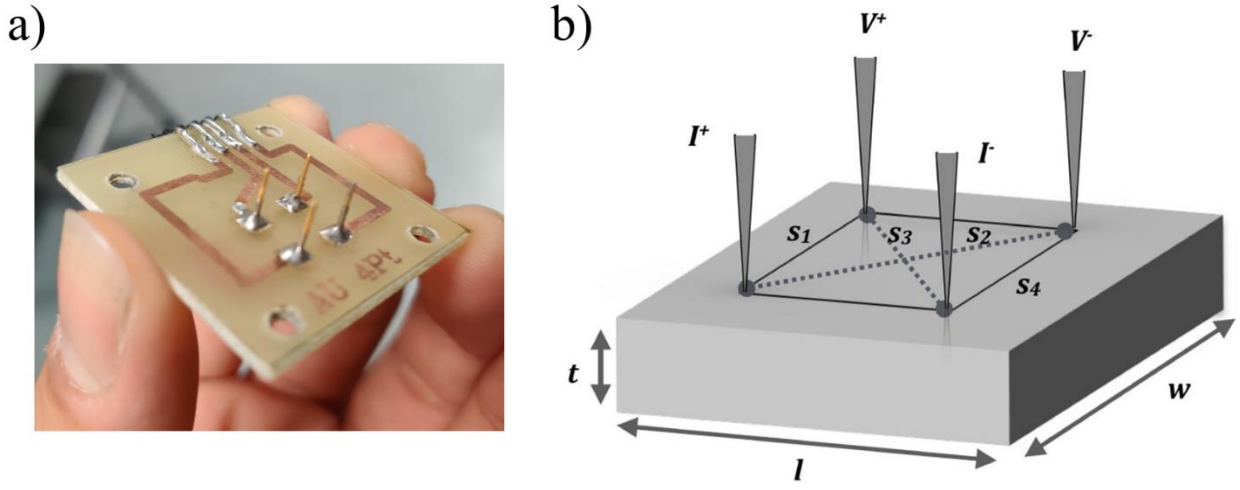

Figure 7.3: a) The in-house four-point probe used to measure the electrical conductivity of the electrospun fibers. b) Schematic for measuring the sheet resistance of fibers[37]. Among the four points, two are used to apply electric voltage and the current output is measured from the other two points.

7.3. Results and discussion

We start with electrospinning only the conducting polymer solutions as prepared in section 7.2.2. The conducting polymer solutions, in absence of a carrier polymer, deposited visible droplets instead of fibers. This has been reported in previous works and it occurs due to the poor processability and low molecular weight of the conducting polymer solution that did not allow it to reach a sufficient elongation threshold to be electrospun properly[38–40]. Addition of carrier

polymers has been shown to improve the processability and aid in electrospinning of conducting polymer solution[41,42], therefore, we prepare a mixture of conducting polymer solution and carrier polymer as described in section 7.2.2.

The electrospun fibers produced from section 7.2.3 are placed on a copper tape and evaluated using the SEM, cf. Figure 7.4a. The resulting SEM images shown are the electrospun PVA fibers without the presence of any conducting polymers, cf. Figure 7.4b. PVA fibers appear to have a high aspect ratio and are randomly oriented under SEM.

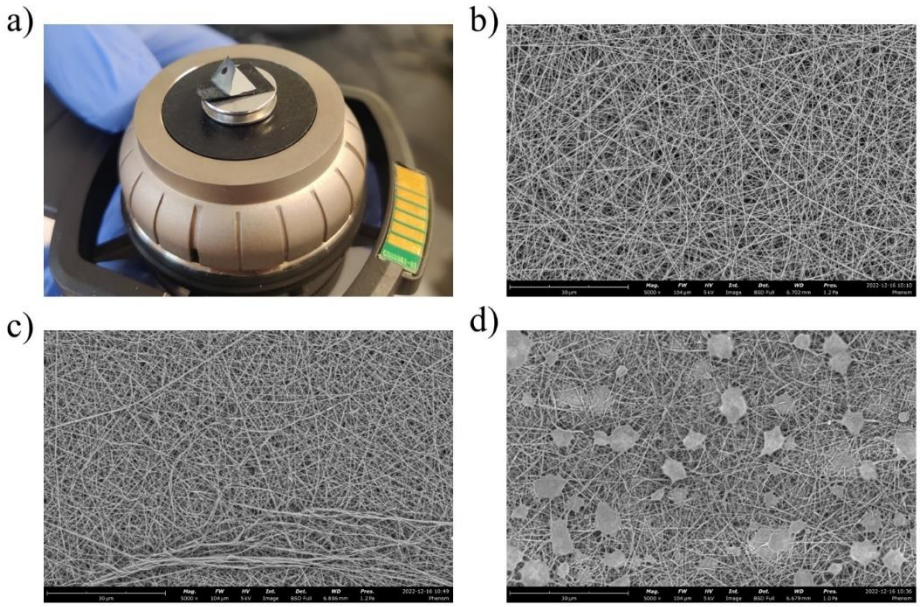

Figure 7.4: Morphological analysis of electrospun fibers. a) The sample fiber mat being attached to the carbon tape before SEM analysis. The resulting SEM images are shown for b) fibers of PVA without the presence of conducting polymers, c) fibers of PANI:DMF and PVA solution and d) fibers of PEDOT:PSS and PVA solutions. The presence of beads in PEDOT:PSS fibers is due to the polymer solution being unable to overcome the surface tension of the solution droplet during electrospinning. The formation of beads are associated with decreased electrical conductivity.

The polymer solution containing PVA and PANI:DMF solution has similar morphology as that of PVA fibers as seen in Figure 7.4c. However, a mixture of PVA and PEDOT:PSS contains beady structures in the middle of the fibers, as seen in Figure 7.4d. This has been previously reported as the viscosity of the polymer solution being unable to overcome the surface tension of solution droplet during electrospinning and failing to form fibers[43,44]. Bead formation in the electrospun fiber has been associated with decreased electrical conductivity and is advisable to minimize them through addition of salt or surfactant to the polymer solution[43,45,46].

Next, we performed mechanical characterization through tensile test of these fibers following the steps mentioned in section 7.2.4.2. The results, shown in Figure 7.5 shows the mechanical response of electrospun fibers to the applied load. PVA fiber is seen to have better elongation at break point compared to PANI+PVA and PEDOT+PVA. The PEDOT+PVA fiber was found to be brittle and failed before the expected elongation of 10-15%. Therefore, PVA+PANI solution was selected to be suitable for EDA sensing application.

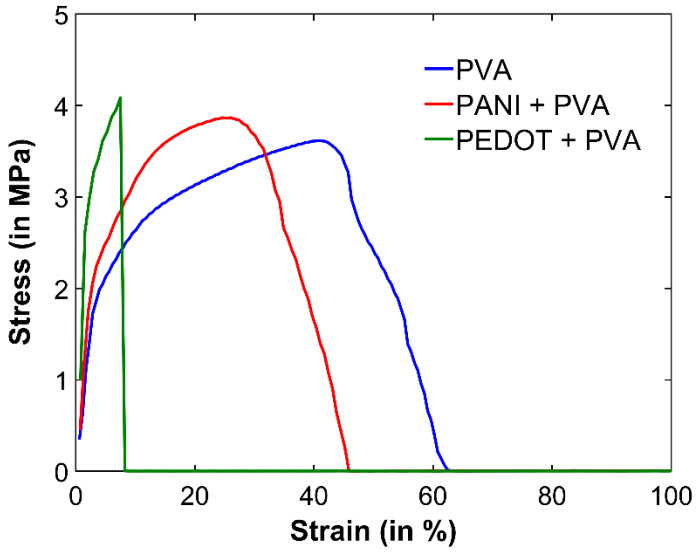

Figure 7.5: Tensile test results for pure PVA fiber (in blue), PANI:DMF and PVA fiber (in red) and PEDOT:PSS and PVA fiber (in green).

Next, we performed the electrical conductivity test following the steps mentioned in section 7.2.4.3. The initial measurement of the surface resistance showed some electrical conductivity in the fiber; however, it tend to diminish over a span of few days to a week and completely loses conductivity at the end of the week. This loss of conductivity over time has been studied earlier and was associated with several processes such as loss/migration of dopant molecule after electrospinning or hydrolysis of conducting polymer chain[47,48]. We postulate the presence of water molecules on the fiber mat, which leads to a loss of electrical conductivity, therefore, we formulated a separate electrospinning process with an addition of the post processing step. In the new electrospinning step, a PVA solution without the conducting polymer is electrospun, followed by a thermal treatment at 45°C for 30 minutes. This ensures evaporation of water molecules (if any) present in the fiber mat. Next, we drop 1ml of conducting polymer solution on electrospun PVA fiber mat, cf. Figure 7.6a. This allowed the retention of electrical conductivity for several weeks and the results are shown in Figure 7.6b. Here, an increase in the amount of conductivity is

seen with an increase in the concentration of conducting polymer solution. An increasing trend of electrical conductivity is to be expected with increasing concentration of conducting polymer[31], however, due to the cytotoxic nature of PANI[49,50] and DMF[51], it was imperative to limit the concentration of conducting polymer solvent for optimized electrical sensing applications.

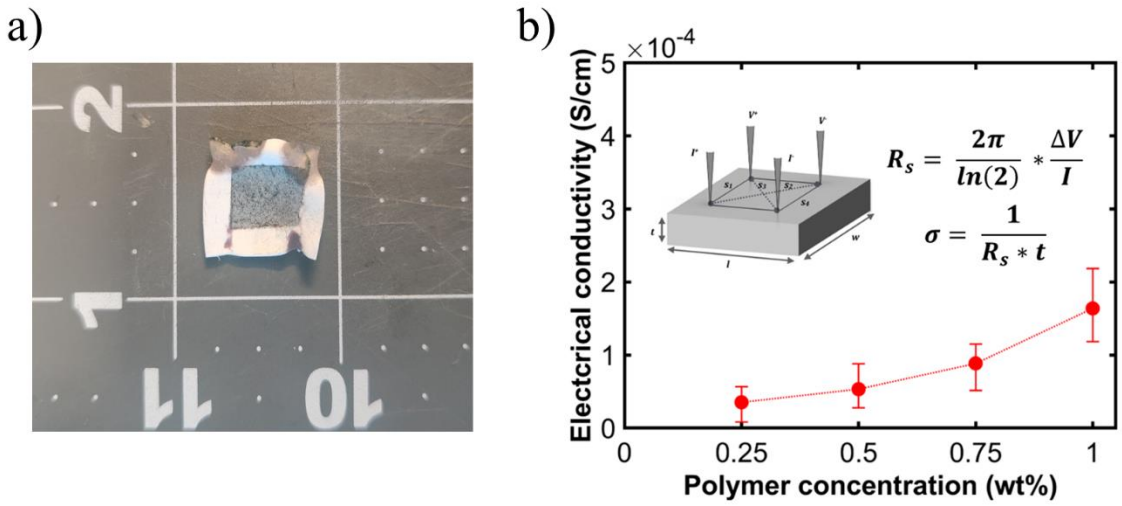

Figure 7.6: a) Electrospun PVA fiber mat after dropping the conducting polymer solution. b) Electrical conductivity of conducting polymer fiber at different concentrations of conducting polymer solution.

7.4. Conclusion

In this chapter, we developed a conducting fiber mat by electrospinning the conducting polymer solution. We electrospun different sets of conducting polymer fiber mat and initial morphological analysis revealed presence of beads on PEDOT:PSS that impeded the electrical conductivity properties. In addition, the mechanical test showed incompatibility of PEDOT:PSS fiber with the design criteria, therefore PANI fiber was chosen to be the optimized solution.

A loss in electrical conductivity of the fiber mat was observed within a week of electrospinning. The fiber production process was improved through a new procedure of

electrospinning the carrier polymer, followed by a post processing step that helped retain the electrical conductivity for several weeks. An increase in electrical conductivity of the fiber mat was observed with an increase in concentration of the conducting polymer. Furthermore, the fiber mat was successfully tested for electrodermal activity and signal sensing analysis was performed for multiple hand gestures.

This study intends to develop an intelligent interface between a human and a prosthetic limb which can sense the user input through electrodermal activity of muscle actuation and enables mobility of wide range of motion in patients with paralysis and spinal cord injuries.

7.5. Acknowledgements

The authors would like to acknowledge the support of Dr. Leily Majidi, Avinash Bhaskaran, Dr. Chad Rose, Armin Seyed Esfahani, Bhargav Yelamanchili, Drew Sellers and Dr. Xinyu Zhang for their assistance in various parts of the project. The authors would also like to thank Toyota Motor Engineering & Manufacturing North America (TEMA) for sponsoring the project.

7.6. References

(1) Wang, L.; Ryan, A. J. Introduction to Electrospinning. In *Electrospinning for Tissue Regeneration*; Bosworth, L. A., Downes, S., Eds.; Woodhead Publishing Series in Biomaterials; Woodhead Publishing, 2011; pp 3–33. https://doi.org/10.1533/9780857092915.1.3.

(2) Wu, S.; Dong, T.; Li, Y.; Sun, M.; Qi, Y.; Liu, J.; Kuss, M. A.; Chen, S.; Duan, B. State-of-the-Art Review of Advanced Electrospun Nanofiber Yarn-Based Textiles for Biomedical Applications. *Appl. Mater. Today* **2022**, *27*, 101473. https://doi.org/10.1016/j.apmt.2022.101473.

(3) Reshmi, C. R.; Nair, S. V.; Menon, D. From Nonwoven Fibers to Woven Nanotextiles: Electrospinning in Drug Delivery. In *Biomedical Applications of Electrospinning and Electrospraying*; Kasoju, N., Ye, H., Eds.; Woodhead Publishing Series in Biomaterials; Woodhead Publishing, 2021; pp 123–156. https://doi.org/10.1016/B978-0-12-822476-2.00003-0.

(4) Barud, H. S.; De Sousa, F. B. Electrospun Materials for Biomedical Applications. *Pharmaceutics* **2022**, *14* (8), 1556. https://doi.org/10.3390/pharmaceutics14081556.

(5) Zhou, Y.; Liu, Y.; Zhang, M.; Feng, Z.; Yu, D.-G.; Wang, K. Electrospun Nanofiber Membranes for Air Filtration: A Review. *Nanomaterials* **2022**, *12* (7), 1077. https://doi.org/10.3390/nano12071077.

(6) Naragund, V. S.; Panda, P. K. Electrospun Nanofiber-Based Respiratory Face Masks—a Review. *Emergent Mater.* **2022**, *5* (2), 261–278. https://doi.org/10.1007/s42247-022-00350-6.

(7) Liu, X.; Xu, H.; Zhang, M.; Yu, D.-G. Electrospun Medicated Nanofibers for Wound Healing: Review. *Membranes* **2021**, *11* (10), 770. https://doi.org/10.3390/membranes11100770.

(8) Balint, R.; Cassidy, N. J.; Cartmell, S. H. Conductive Polymers: Towards a Smart Biomaterial for Tissue Engineering. *Acta Biomater.* **2014**, *10* (6), 2341–2353. https://doi.org/10.1016/J.ACTBIO.2014.02.015.

(9) Sun, G.; Sun, L.; Xie, H.; Liu, J. Electrospinning of Nanofibers for Energy Applications. *Nanomaterials* **2016**, *6* (7), 129. https://doi.org/10.3390/nano6070129.

(10) Halicka, K.; Cabaj, J. Electrospun Nanofibers for Sensing and Biosensing Applications—A Review. *Int. J. Mol. Sci.* **2021**, *22* (12), 6357. https://doi.org/10.3390/ijms22126357.

(11) Das, R.; Zeng, W.; Asci, C.; Del-Rio-Ruiz, R.; Sonkusale, S. Recent Progress in Electrospun Nanomaterials for Wearables. *APL Bioeng.* **2022**, *6* (2), 21505. https://doi.org/10.1063/5.0088136.

(12) Wang, Y.; Yokota, T.; Someya, T. Electrospun Nanofiber-Based Soft Electronics. *NPG Asia Mater.* **2021**, *13* (1), 1–22. https://doi.org/10.1038/s41427-020-00267-8.

(13) Xue, J.; Wu, T.; Dai, Y.; Xia, Y. Electrospinning and Electrospun Nanofibers: Methods, Materials, and Applications. *Chem. Rev.* **2019**, *119* (8), 5298–5415. https://doi.org/10.1021/acs.chemrev.8b00593.

(14) Velasco Barraza, R. D.; Álvarez Suarez, A. S.; Villarreal Gómez, L. J.; Paz González, J. A.; Iglesias, A. L.; Vera Graziano, R.; Velasco Barraza, R. D.; Álvarez Suarez, A. S.; Villarreal Gómez, L. J.; Paz González, J. A.; Iglesias, A. L.; Vera Graziano, R. Designing a Low Cost Electrospinning Device for Practical Learning in a Bioengineering Biomaterials Course. *Rev. Mex. Ing. Bioméd.* **2016**, *37* (1), 7–16. https://doi.org/10.17488/RMIB.37.1.1.

(15) Laudenslager, M. J.; Sigmund, W. M. Electrospinning. *Encycl. Nanotechnol. Bhushan B Ed Springer Dordr. Neth.* **2012**, 769–775.

(16) Haider, A.; Haider, S.; Kang, I.-K. A Comprehensive Review Summarizing the Effect of Electrospinning Parameters and Potential Applications of Nanofibers in Biomedical and Biotechnology. *Arab. J. Chem.* **2018**, *11* (8), 1165–1188. https://doi.org/10.1016/j.arabjc.2015.11.015.

(17) Bavatharani, C.; Muthusankar, E.; Wabaidur, S. M.; Alothman, Z. A.; Alsheetan, K. M.; AL-Anazy, M. mana; Ragupathy, D. Electrospinning Technique for Production of Polyaniline

Nanocomposites/Nanofibres for Multi-Functional Applications: A Review. *Synth. Met.* **2021**, *271*, 116609. https://doi.org/10.1016/j.synthmet.2020.116609.

(18) Abd Razak, S. I.; Wahab, I. F.; Fadil, F.; Dahli, F. N.; Md Khudzari, A. Z.; Adeli, H. A Review of Electrospun Conductive Polyaniline Based Nanofiber Composites and Blends: Processing Features, Applications, and Future Directions. *Adv. Mater. Sci. Eng.* **2015**, *2015*, e356286. https://doi.org/10.1155/2015/356286.

(19) Zhou, J.; Wang, Y.; Cheng, L.; Wu, Z.; Sun, X.; Peng, J. Preparation of Polypyrrole-Embedded Electrospun Poly(Lactic Acid) Nanofibrous Scaffolds for Nerve Tissue Engineering. *Neural Regen. Res.* **2016**, *11* (10), 1644–1652. https://doi.org/10.4103/1673-5374.193245.

(20) Chronakis, I. S.; Grapenson, S.; Jakob, A. Conductive Polypyrrole Nanofibers via Electrospinning: Electrical and Morphological Properties. *Polymer* **2006**, *47* (5), 1597–1603. https://doi.org/10.1016/j.polymer.2006.01.032.

(21) Chan, E. W. C.; Bennet, D.; Baek, P.; Barker, D.; Kim, S.; Travas-Sejdic, J. Electrospun Polythiophene Phenylenes for Tissue Engineering. *Biomacromolecules* **2018**, *19* (5), 1456–1468. https://doi.org/10.1021/acs.biomac.8b00341.

(22) Bhattacharya, S.; Roy, I.; Tice, A.; Chapman, C.; Udangawa, R.; Chakrapani, V.; Plawsky, J. L.; Linhardt, R. J. High-Conductivity and High-Capacitance Electrospun Fibers for Supercapacitor Applications. *ACS Appl. Mater. Interfaces* **2020**, *12* (17), 19369–19376. https://doi.org/10.1021/acsami.9b21696.

(23) Li, Y.; Góra, A.; Anariba, F.; Baji, A. Enhanced Tensile Strength and Electrical Conductivity of Electrospun Polyacrylonitrile Yarns via Post-Treatment. *Polym. Compos.* **2019**, *40* (5), 1702–1707. https://doi.org/10.1002/pc.24920.

(24) Garrudo, F. F. F.; Chapman, C. A.; Hoffman, P. R.; Udangawa, R. W.; Silva, J. C.; Mikael, P. E.; Rodrigues, C. A. V.; Cabral, J. M. S.; Morgado, J. M. F.; Ferreira, F. C.; Linhardt, R. J. Polyaniline-Polycaprolactone Blended Nanofibers for Neural Cell Culture. *Eur. Polym. J.* **2019**, *117*, 28–37. https://doi.org/10.1016/j.eurpolymj.2019.04.048.

(25) Shirakawa, H.; J. Louis, E.; G. MacDiarmid, A.; K. Chiang, C.; J. Heeger, A. Synthesis of Electrically Conducting Organic Polymers: Halogen Derivatives of Polyacetylene, (CH) x. *J. Chem. Soc. Chem. Commun.* **1977**, *0* (16), 578–580. https://doi.org/10.1039/C39770000578.

(26) Ghasemi-Mobarakeh, L.; Prabhakaran, M. P.; Morshed, M.; Nasr-Esfahani, M. H.; Baharvand, H.; Kiani, S.; Al-Deyab, S. S.; Ramakrishna, S. Application of Conductive Polymers, Scaffolds and Electrical Stimulation for Nerve Tissue Engineering. *J. Tissue Eng. Regen. Med.* **2011**, *5* (4), e17–e35. https://doi.org/10.1002/term.383.

(27) Bredas, J. L.; Street, G. B. Polarons, Bipolarons, and Solitons in Conducting Polymers. *Acc. Chem. Res.* **1985**, *18* (10), 309–315. https://doi.org/10.1021/ar00118a005.

(28) Kim, D.-H.; Richardson-Burns, S. M.; Hendricks, J. L.; Sequera, C.; Martin, D. C. Effect of Immobilized Nerve Growth Factor on Conductive Polymers: Electrical Properties and Cellular Response. *Adv. Funct. Mater.* **2007**, *17* (1), 79–86. https://doi.org/10.1002/adfm.200500594.

(29) Wong, J. Y.; Langer, R.; Ingber, D. E. Electrically Conducting Polymers Can Noninvasively Control the Shape and Growth of Mammalian Cells. *Proc. Natl. Acad. Sci.* **1994**, *91* (8), 3201–3204. https://doi.org/10.1073/pnas.91.8.3201.

(30) Beygisangchin, M.; Abdul Rashid, S.; Shafie, S.; Sadrolhosseini, A. R. Polyaniline Synthesized by Different Dopants for Fluorene Detection via Photoluminescence Spectroscopy. *Materials* **2021**, *14* (23), 7382. https://doi.org/10.3390/ma14237382.

(31) Bednarczyk, K.; Matysiak, W.; Tański, T.; Janeczek, H.; Schab-Balcerzak, E.; Libera, M. Effect of Polyaniline Content and Protonating Dopants on Electroconductive Composites. *Sci. Rep. 2021 111* **2021**, *11* (1), 1–11. https://doi.org/10.1038/s41598-021-86950-4.

(32) Ravichandran, R.; Sundarrajan, S.; Venugopal, J. R.; Mukherjee, S.; Ramakrishna, S. Applications of Conducting Polymers and Their Issues in Biomedical Engineering. *J. R. Soc. Interface* **2010**, *7 Suppl 5* (Suppl 5), S559-579. https://doi.org/10.1098/rsif.2010.0120.focus.

(33) Liu, Z.-H.; Huang, Y.-C.; Kuo, C.-Y.; Kuo, C.-Y.; Chin, C.-Y.; Yip, P. K.; Chen, J.-P. Docosahexaenoic Acid-Loaded Polylactic Acid Core-Shell Nanofiber Membranes for Regenerative Medicine after Spinal Cord Injury: In Vitro and In Vivo Study. *Int. J. Mol. Sci.* **2020**, *21* (19), 7031. https://doi.org/10.3390/ijms21197031.

(34) Rickel, A. P.; Deng, X.; Engebretson, D.; Hong, Z. Electrospun Nanofiber Scaffold for Vascular Tissue Engineering. *Mater. Sci. Eng. C Mater. Biol. Appl.* **2021**, *129*, 112373. https://doi.org/10.1016/j.msec.2021.112373.

(35) Park, J.-C.; Ito, T.; Kim, K.-O.; Kim, K.-W.; Kim, B.-S.; Khil, M.-S.; Kim, H.-Y.; Kim, I.-S. Electrospun Poly(Vinyl Alcohol) Nanofibers: Effects of Degree of Hydrolysis and Enhanced Water Stability. *Polym. J.* **2010**, *42* (3), 273–276. https://doi.org/10.1038/pj.2009.340.

(36) Maccaferri, E.; Mazzocchetti, L.; Benelli, T.; Zucchelli, A.; Giorgini, L. Morphology, Thermal, Mechanical Properties and Ageing of Nylon 6,6/Graphene Nanofibers as Nano2 Materials. *Compos. Part B Eng.* **2019**, *166*, 120–129. https://doi.org/10.1016/j.compositesb.2018.11.096.

(37) Miccoli, I.; Edler, F.; Pfnür, H.; Tegenkamp, C. The 100th Anniversary of the Four-Point Probe Technique: The Role of Probe Geometries in Isotropic and Anisotropic Systems. *J. Phys. Condens. Matter* **2015**, *27* (22), 223201. https://doi.org/10.1088/0953-8984/27/22/223201.

(38) Zhao, Y.; Zhang, Z.; Yu, L.; Tang, Q. Electrospinning of Polyaniline Microfibers for Anticorrosion Coatings: An Avenue of Enhancing Anticorrosion Behaviors. *Synth. Met.* **2016**, *212*, 84–90. https://doi.org/10.1016/j.synthmet.2015.12.007.

(39) Norris, I. D.; Shaker, M. M.; Ko, F. K.; MacDiarmid, A. G. Electrostatic Fabrication of Ultrafine Conducting Fibers: Polyaniline/Polyethylene Oxide Blends. *Synth. Met.* **2000**, *114* (2), 109–114. https://doi.org/10.1016/S0379-6779(00)00217-4.

(40) Frontera, P.; Busacca, C.; Trocino, S.; Antonucci, P.; Faro, M. L.; Falletta, E.; Pina, C. D.; Rossi, M. Electrospinning of Polyaniline: Effect of Different Raw Sources. *J. Nanosci. Nanotechnol.* **2013**, *13* (7), 4744–4751. https://doi.org/10.1166/jnn.2013.7196.

(41) Shahi, M.; Moghimi, A.; Naderizadeh, B.; Maddah, B. Electrospun PVA–PANI and PVA–PANI–AgNO3 Composite Nanofibers. *Sci. Iran.* **2011**, *18* (6), 1327–1331. https://doi.org/10.1016/j.scient.2011.08.013.

(42) Fotia, A.; Malara, A.; Paone, E.; Bonaccorsi, L.; Frontera, P.; Serrano, G.; Caneschi, A. Self Standing Mats of Blended Polyaniline Produced by Electrospinning. *Nanomaterials* **2021**, *11* (5), 1269. https://doi.org/10.3390/nano11051269.

(43) Higashi, S.; Hirai, T.; Matsubara, M.; Yoshida, H.; Beniya, A. Dynamic Viscosity Recovery of Electrospinning Solution for Stabilizing Elongated Ultrafine Polymer Nanofiber by TEMPO-CNF. **123AD**. https://doi.org/10.1038/s41598-020-69136-2.

(44) Fong, H.; Chun, I.; Reneker, D. H. Beaded Nanofibers Formed during Electrospinning. *Polymer* **1999**, *40* (16), 4585–4592. https://doi.org/10.1016/S0032-3861(99)00068-3.

(45) Liu, Y.; He, J.-H.; Yu, J.; Zeng, H. Controlling Numbers and Sizes of Beads in Electrospun Nanofibers. *Polym. Int.* **2008**, *57* (4), 632–636. https://doi.org/10.1002/pi.2387.

(46) Abutaleb, A.; Lolla, D.; Aljuhani, A.; Shin, H. U.; Rajala, J. W.; Chase, G. G. Effects of Surfactants on the Morphology and Properties of Electrospun Polyetherimide Fibers. *Fibers* **2017**, *5* (3), 33. https://doi.org/10.3390/fib5030033.

(47) Rannou, P.; Nechtschein, M.; Travers, J. P.; Berner, D.; Woher, A.; Djurado, D. Ageing of PANI: Chemical, Structural and Transport Consequences. *Synth. Met.* **1999**, *101* (1), 734–737. https://doi.org/10.1016/S0379-6779(98)00207-0.

(48) Jousseaume, V.; Morsli, M.; Bonnet, A. Aging of Electrical Conductivity in Conducting Polymer Films Based on Polyaniline. *J. Appl. Phys.* **2000**, *88* (2), 960–966. https://doi.org/10.1063/1.373762.

(49) Humpolicek, P.; Kasparkova, V.; Saha, P.; Stejskal, J. Biocompatibility of Polyaniline. *Synth. Met.* **2012**, *162* (7), 722–727. https://doi.org/10.1016/j.synthmet.2012.02.024.

(50) Ghasemi-Mobarakeh, L.; Prabhakaran, M. P.; Morshed, M.; Nasr-Esfahani, M. H.; Baharvand, H.; Kiani, S.; Al-Deyab, S. S.; Ramakrishna, S. Application of Conductive Polymers, Scaffolds and Electrical Stimulation for Nerve Tissue Engineering. *J. Tissue Eng. Regen. Med.* **2011**, *5* (4), e17–e35. https://doi.org/10.1002/term.383.

(51) Ilieva, Y.; Dimitrova, L.; Zaharieva, M. M.; Kaleva, M.; Alov, P.; Tsakovska, I.; Pencheva, T.; Pencheva-El Tibi, I.; Najdenski, H.; Pajeva, I. Cytotoxicity and Microbicidal Activity of

Commonly Used Organic Solvents: A Comparative Study and Application to a Standardized Extract from Vaccinium Macrocarpon. *Toxics* **2021**, *9* (5), 92. https://doi.org/10.3390/toxics9050092.

Chapter 8

Summary and potential future works

8.1. Summary

In this dissertation, smart materials in the form of shape memory polymers and electrospun conducting polymer fibers were studied for their actuation and sensing capabilities respectively. Commercially available polystyrene was used for the material model in finite element framework and were studied for their shape memory applications including pre-straining, uniform shrinking and self-folding. The structure property relationship analysis was carried out for polymers undergoing physical aging and UV aging. Finally, electrically conducting polymers such as PANI and PEDOT:PSS were electrospun to fabricate non-woven fiber mats which has the ability to sense electrical signal from muscle actuation in human body.

In chapter 3, a previously developed finite element framework was used to analyze the thermomechanical biaxial pre-straining of a polymer through hot rolling and its shape recovery performance. The amount of strain generated by the roller, in two orthogonal directions, were evaluated. In addition, the role of friction between the roller and workpiece on the amount of stress applied on the workpiece surface is analyzed. Finally, the effects of processing parameters were evaluated to maximize the shape fixity and shape recovery of the pre-strained polymer. It was found that process parameters such as feed rate and rate of uniform heating changes the shape recovery performance, while roller speed has very little effect on the pre-straining efficiency.

In chapter 4, the shape recovery performance of a pre-strained polymer was analyzed with an applied electric field as an external stimulus. For this, the existing coupled thermomechanical finite element framework was modified to include electrical energy which generates resistive Joule heating to initiate the shape recovery response. This research investigated the effects of various

parameters such as electrical conductivity, width of the conducting hinge, and the applied voltage on the shape recovery performance of the pre-strained polymer. The shape recovery performance was measured through uniform shrinking and localized folding of the pre-strained polymer with an applied electric field. It was found that folding was initiated only after the polymer reaches its T_g. In addition, the speed at which it folds depends on the conductivity of the hinge, width of the hinge, and the applied voltage across the hinge.

In chapter 5, polymers were studied for their shape recovery performance, while undergoing physical aging process. Physical aging takes the polymer chains through structural relaxation where these chains change their polymer chain conformation and relaxes to lower energy configuration by losing its enthalpy. This lost in enthalpy was quantified for parameters such as aging time, strain rate and applied strain and their effects on shape recovery performance was evaluated. It was found that an increase in lost enthalpy correlates to an increase in the characteristic shape recovery time, thus slowing down the shape recovery performance. However, physically aging for more than 16 hours resulted in small changes to the enthalpy lost. This is explained by the fact that majority of the polymer chains reach lower energy configuration by losing its enthalpy during this time and decreases the shape recovery performance of the polymer.

In chapter 6, the effects of space environments, such as exposure to UV-C radiation and atomic oxygen on polymers were studied for their shape recovery performance. The polymers were exposed under these environments for prolonged time, during which the polymer chains get chemically degraded through chain scission and introduces foreign functional group to the polymer chain backbone. The degradation of polymer chains were analyzed through infrared spectroscopy and the presence of foreign functional group was found on UV-aged polymers. This degraded the viscoelastic properties of the polymer and resulted in decreased shape recovery performance. In

addition, a set of thermoplastic and thermoset polymers were sent to the international space station (ISS) for a 6-month long experiment to determine the effects of prolonged exposure of the space environments to the polymers.

In chapter 7, the sensing application of smart materials was studied through conducting polymer fibers. The fibers were fabricated through an electrospinning process and were characterized for their morphology, thermal, mechanical and electrical performance. A number of conducting polymers were evaluated for the sensing application and they showed varying degrees of electrical conductivity. It was found that the fibers electrical conductivity increased with an increase in the concentration of conducting polymer solvent. The work done in this chapter can ultimately be used for human machine interaction, where the conducting polymer fiber can act as an interface and provide mobility to prosthetic limbs according to the electrical signals generated from the muscles.

8.2. Potential future works

The potential of smart materials are endless and has been applied in a number of industrial applications including biomedicine, automotive, aerospace, textile, etc. This dissertation tries to investigate fundamental process and performance associated with the shape memory applications of polymers. In doing so, this work has opened up a broad area of investigation to drive the research in smart materials. These are some of the potential future works that the author believes will be the next step for each part of the dissertation.

a. Chapter 3: In this chapter, biaxial pre-straining process of polymers through rolling were studied through computational finite element framework. The study investigated the effects

of processing parameters associated with this process and analyzed the shape recovery performance with heating rate of the pre-strained polymer.

One of the directions this project could proceed is by creating a functional in-house pre-straining setup where a number of polymers could be pre-strained and later studied for shape recovery analysis. The preliminary design for the in-house pre-straining setup is provided in this chapter and needs to be assembled. Another direction would be to study the effects of cooling rate of the polymers exiting the roller as higher cooling rates provide better pre-straining by fixing the polymer chain motion quickly. In order to do this, the experimental setup could use water bath to quickly quench the polymer exiting the rollers. Therefore, another research topic could be an experimental verification of this model by getting the pre-straining setup ready and studying the effects of process parameters on shape fixity and shape recovery performance.

b. Chapter 4: In this chapter, the finite element framework was modified to include the electrical properties of the material and analyzed for the localized shrinkage of the polymer during shape recovery process. This localized shrinkage results in self-folding of the pre-strained polymer.

The potential future works for this chapter will be an experimental verification of the model. The polymer will require a conducting pathway printed on top of the surface. It could be done by direct ink writing (DIW) process where a conducting solution could be printed directly on top of the surface of the polymer.

c. Chapter 5: In this chapter, the structure-property relationship of the polymer undergoing physical aging was performed. During physical aging, the polymer chains undergo structural relaxation process by approaching lower energy state. These effects were later

induced in polymer through pre-straining process and the effects of lost enthalpy was evaluated for the shape recovery performance of the polymer.

The future direction for this project would be to analyze the effects of physical aging on thermoset polymers as their structure contain stronger intermolecular bonds. This will affect the aging behavior and would be interesting to analyze the effects on its mechanical and thermodynamic properties.

d. Chapter 6: In this chapter, the polymers were aged for up to 24 hours in low earth orbit (LEO) environments such as UV-C radiation and atomic oxygen. During prolonged exposure to such environments, the polymer chains undergo rapid photooxidation process. This breaks down the backbone of the polymer and weaken the structural configuration and mechanical properties of the polymer.

The next phase of this project is ongoing as some of the samples were sent to the international space station (ISS) for a 6-month long experiment where these samples are exposed to the LEO environment. Once the sample is received, the above experiments can be performed to analyze the extent of degradation on these polymers. Another step for this project could be to work on UV stabilization coatings. This could involve exploring novel UV-absorbing compounds or nanomaterials that can efficiently dissipate UV energy and prevent degradation.

e. Chapter 7: In this chapter, we fabricate electrically conducting polymer fiber mat through electrospinning process. Through this, we intend to develop an intelligent interface between a human and a prosthetic limb which can sense the user input through electrodermal activity of muscle actuation and enables mobility of wide range of motion in patients with paralysis and spinal cord injuries.

The future direction with this project is to enhance the electrical conductivity of electrospun polymer fiber. This could involve the incorporation of conductive additives, such as carbon nanotubes or graphene, to achieve higher electrical performance. Another direction for this project could be to conduct clinical studies to validate the performance of electrospun fiber mats for specific medical applications, such as stress management.